Molecular Dynamics Simulation of Boundary Lubrication

by

Shon W. Yim
S.B. Mechanical Engineering
University of Illinois, 1995

Submitted to the Department of Mechanical Engineering
in partial fulfillment of the requirements
for the degree of

MASTER OF SCIENCE IN MECHANICAL ENGINEERING

at the

MASSACHUSETTS INSTITUTE OF TECHNOLOGY

May, 1997

Author .....
Department of Mechanical Engineering
May 9, 1997

Certified by .....
Nannaji Saka
Principal Research Scientist and Lecturer
Department of Mechanical Engineering

Certified by .....
Nishikant Sonwalkar
Research Scientist and Director of Hypermedia Teaching Facility
Department of Mechanical Engineering

Accepted by .....
Ain A. Sonin
Chairman, Department Graduate Committee

Molecular Dynamics Simulation of Boundary Lubrication

by

Shon W. Yim

Submitted to the Department of Mechanical Engineering
on May 9, 1997, in partial fulfillment of the
requirements for the degree of
Master of Science in Mechanical Engineering

Abstract

A molecular dynamics simulation study of friction in boundary lubrication was conducted in order to investigate the atomic-scale behavior of the lubricant molecules during the sliding motion. The simulated system consisted of two silicon (001) semi-infinite substrates lubricated by a thin, three layer film of dodecane. Silicon was modeled using the Stillinger-Weber potential, and the dodecane with the Consistent Force Field potential function; a novel scheme was used to generate the silicon-dodecane interaction potentials. The simulations show that the dodecane molecules strongly prefer to adsorb into ledges on the silicon surface. The orientation of the adsorbed molecules depends heavily on the concentration of the lubricant at the Si surface, showing a tendency to stand up at high lubricant concentrations. In sliding, the dodecane layers adsorbed on the silicon surfaces behave as a solid, whereas the middle layer exhibits more liquid-like characteristics. The friction coefficient of this well-lubricated case was calculated to be 0.07, well within the range for boundary lubricated systems. In addition, simulations of dry sliding of two dissimilar Lennard-Jones materials were performed. It was found that the mismatch of the lattices at the interface caused warping in the interface layer of the softer material. The forces required to continuously distort the warped layer could be a significant contribution to the friction force.

Thesis Supervisor: Nannaji Saka
Title: Principal Research Scientist and Lecturer

Thesis Supervisor: Nishikant Sonwalkar
Title: Research Scientist and Director of Hypermedia Teaching Facility

Acknowledgments

I would like to thank my God, Jesus Christ.

I also thank my parents and my sister for giving me encouragement and support. I thank them especially for displaying courage and faith during difficult times. I owe them not only this degree, but everything that I have thus far accomplished.

From the beginning to the very end of this project, Dr. Saka dedicated himself to guide me. He always made time to talk with me and to proof-read twice everything I ever wrote. He is, to me, the expert in tribology, and I thank him for teaching me everything I know on the subject. Dr. Sonwalkar also deserves my gratitude for patiently teaching me all about molecular dynamics simulations. He also took interest in my personal life, and I thank him for helping me take bold steps toward my future. He also provided all of the computational equipment in his lab. The nice color graphics in this thesis were created with his visualization program.

I was lucky to have had great company throughout this project. Michael Silvestro, a good fellow researcher and friend; Natasha Chang, who daringly crosses mile-long bridges over a frozen river through the snow everyday to come to work; Stewart Jenkins, my #1 bus buddy; ; and Nandini Iyer, the nicest person at this institution, who has honored me with her friendship.

The molecular dynamics code used in this work was a revised version of the program written by Professor James Haile at Cornell University. Also, the Stillinger-Weber potential code was originally obtained from Dr. Vasily Bulatov of the Department of Mechanical Engineering at MIT.

Finally, I gratefully acknowledge that this project was funded by the Surface Engineering and Tribology Program of the National Science Foundation under the direction of Dr. Jorn Larsen-Basse.

Contents

1 Introduction 10

1.1 Classical Model of Boundary Lubrication 11

1.2 Friction Coefficient of Boundary Lubricated Surfaces 12

1.3 Research Goals and Methodology 15

1.4 Present Developments in Molecular Tribology 16

1.5 Problem Statement and Thesis Organization 18

2 Molecular Dynamics Simulation 20

2.1 Potential Functions 21

2.1.1 The Lennard-Jones Potential Function 22

2.1.2 The Stillinger-Weber Potential Function 23

2.1.3 Hydrocarbon Potential Function 25

2.2 Boundary Conditions 29

2.3 Parrinello-Rahman Method 31

2.4 Property Calculations 33

2.5 Monte Carlo Simulation 38

3 Simulation of Ideal Solids in Sliding 40

3.1 Single Atom Simulation 44

3.2 Interface Formation 46

3.3 Compression and Sliding 50

4 Potential Functions of the Silicon-Dodecane System 65

4.1 Simulation of Silicon 65
4.2 Simulation of Dodecane 72
4.3 Silicon-Hydrocarbon Interaction Potential 77

5 Simulation of Boundary Lubrication **83**
5.1 Adsorption and Desorption of Dodecane 85
5.2 Silicon-Dodecane System in Compression and Sliding 95

6 Conclusions and Future Research **110**

List of Figures

1-1 Schematic of lubricated asperity contact. 11

1-2 Schematic of friction test apparatus. 13

2-1 General schematic of an MD simulation cell. 21

2-2 Schematic of 2-D periodic boundary conditions. 30

2-3 Schematic of semi-infinite and thin film boundary conditions. 32

2-4 Schematic of a Parrinello-Rahman simulation cell. 34

3-1 Schematic of Ar-Xe system. 41

3-2 L-J potential functions for Ar-Xe system. 43

3-3 Schematic of on-top and hollow-site geometries. 44

3-4 Potential energy of on-top and hollow-site geometries. 45

3-5 Ar-Xe system before interaction. 47

3-6 Ar-Xe system after interaction. 48

3-7 Radial distribution function of Ar-Xe system. 49

3-8 Ar-Xe interface: top view. 51

3-9 Instantaneous tangential and normal stresses in Ar-Xe sliding. 53

3-10 Average tangential and normal stresses in Ar-Xe sliding. 54

3-11 Mean squared displacement of argon and xenon layers during sliding. 56

3-12 Ar-Xe system after 1.06 Å of sliding. 57

3-13 Ar-Xe system after 2.12 Å of sliding. 58

3-14 Ar-Xe system after 3.18 Å of sliding. 59

3-15 Ar-Xe system after 4.24 Å of sliding. 60

3-16 Ar-Xe system after 5.30 Å of sliding. 61

3-17 Potential energy surfaces of Ar-Xe interface during sliding. 62
3-18 Radial distribution function of Ar-Xe interface during sliding. 63

4-1 SW potential energy. 66
4-2 Radial distribution function of solid and liquid silicon. 68
4-3 Viscosity of bulk dodecane. 73
4-4 Vibrational spectrum of carbon atoms in bulk dodecane. 75
4-5 Vibrational spectrum of hydrogen atoms in bulk dodecane. 76
4-6 L-J 9-6 representation of the SW potential function. 80
4-7 Si-C and Si-H interaction potentials. 82

5-1 Schematic of simulation cell for the silicon-dodecane system. 84
5-2 Initial position of one dodecane molecule: top view. 86
5-3 Initial position of one dodecane molecule: side view. 87
5-4 Final position of one dodecane molecule: top view. 89
5-5 Final position of one dodecane molecule: side view. 90
5-6 Final position of nine dodecane molecules: top view. 91
5-7 Final position of nine dodecane molecules: side view. 92
5-8 Mean squared displacement of carbon atoms on silicon surface. 94
5-9 Compressed silicon-dodecane system. 98
5-10 Instantaneous tangential and normal stresses in silicon-dodecane sliding. 100
5-11 Tangential and normal stresses in silicon-dodecane sliding. 101
5-12 Silicon-dodecane system before sliding. 103
5-13 Silicon-dodecane system after 1.54 Å of sliding. 104
5-14 Silicon-dodecane system after 3.07 Å of sliding. 105
5-15 Silicon-dodecane system after 4.61 Å of sliding. 106
5-16 Silicon-dodecane system after 6.14 Å of sliding. 107
5-17 Silicon-dodecane system after 7.68 Å of sliding. 108

List of Tables

1.1 Friction coefficient of various boundary lubricated surfaces. 14
1.2 Friction coefficient of boundary lubricated silicon (001) surfaces. . . . 15

2.1 SW potential parameters. 25
2.2 UAM potential parameters. 26
2.3 CFF potential parameters. 28

3.1 Ar-Xe system parameters. 41
3.2 L-J parameters of Ar-Xe system. 42
3.3 Static structure factor of Ar-Xe layers. 46
3.4 Summary of Ar-Xe sliding experiment. 55

4.1 Parameters for the simulation of bulk Si. 67
4.2 Calculated average density of silicon. 69
4.3 Calculated stresses in silicon due to uniaxial strain. 70
4.4 Calculated stresses in silicon due to simple shear. 70
4.5 Calculated elastic constants of silicon. 71
4.6 Parameters for the simulation of dodecane using UAM potential. . . . 72
4.7 Band assignment of the vibrational frequencies in dodecane. 77
4.8 L-J parameters for Si-C and Si-H interaction potential. 81

5.1 Parameters for the simulation of one dodecane molecule. 85
5.2 Vibrational spectral peaks for adsorbed dodecane. 95
5.3 Parameters for the simulation of compression and sliding. 96
5.4 Tangential and normal stresses in silicon-dodecane sliding. 100

5.5 Vibrational spectral peaks of dodecane in compression and sliding. . . 109

Chapter 1

Introduction

Friction and wear of solid surfaces in sliding pose limitations to the function and life of mechanical components resulting in losses of efficiency and capital. To improve component life, lubricants are commonly used to lower the friction force at the interface, thereby reducing wear. Recently, the growth of micro-devices such as the microelectromechanical systems (MEMS) have placed increased demands on interface contacts to be able to operate at smaller and smaller clearances. In addition, magnetic recording devices in high-speed computers are currently being required to run at smaller separation heights and at higher sliding velocities [1, 2, 3]. It is crucial for these systems to avoid catastrophic failure arising from high friction forces between the head and the recording media.

In these high-precision systems, the separation gap between the surfaces is so small that the lubricant film operates in the boundary lubrication regime. Although a few theories on the fundamental mechanisms of friction in boundary lubrication have been suggested, the true physical understanding of the molecular processes that contribute to the generation of friction is still lacking. Consequently, the selection of lubricants for given surfaces and applications has been largely based on experimental trial-and-error. Thus, the benefits of an improved understanding of the friction in boundary lubrication are numerous. For example, a more efficient way of custom designing lubricants for certain applications could greatly improve the effectiveness as well as service life of lubricated surfaces.

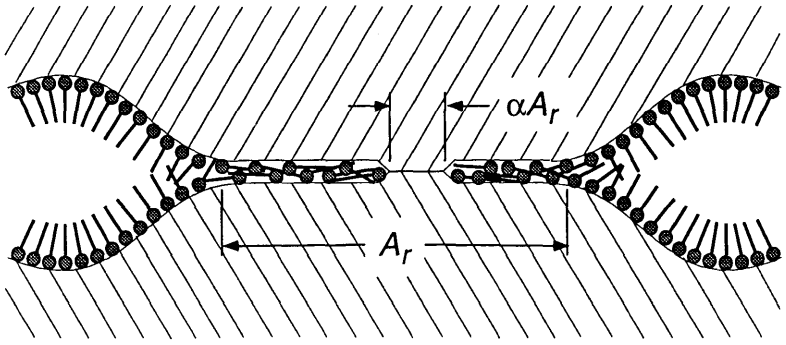

Figure 1-1: Schematic of lubricated asperity contact.

1.1 Classical Model of Boundary Lubrication

Boundary lubrication occurs in the regime where the lubricant thickness separating the sliding surfaces is small, about 1 nm. At this level, the friction force is governed by the physical and chemical interactions between the lubricant film and the sliding surfaces [4]. The lubrication is essentially provided by a monolayer of lubricant molecules that are adsorbed on the solid surfaces [5]. The adsorption of the monolayer on the surface depends on variables such as the molecular structure of the lubricant [6], the physical properties of the lubricant film [7, 8], the environmental humidity [9], and so on.

The classical model for boundary lubricated surfaces in contact assumes that the real area of contact, A_r shown in Figure 1-1, occurs where asperities of the two opposing surfaces meet. Moreover, a fraction α of the real area of contact is in solid-to-solid contact. The remaining portion of A_r is said to be lubricated. Based on this model, Bowden [5] postulated the following expression for the friction force, F:

$$F = A_r \left[\alpha s_m + (1 - \alpha) s_l\right], \tag{1.1}$$

where s_l and s_m are the shear strengths of the lubricant film and the substrate,

respectively. Assuming that the asperities are in a state of plastic deformation, the normal stress can be equated to the hardness of the substrate, p_m, so that the friction coefficient μ can be written [6],

$$\mu = \alpha \frac{s_m}{p_m} + (1 - \alpha) \frac{s_l}{p_m}. \tag{1.2}$$

The above equation is difficult to apply because the parameters α and s_l are not easily acquired. Furthermore, there are fundamental limitations in that the shearing of the lubricant film is assumed to be the sole contribution to the friction force when $\alpha = 0$. However, if the asperities are plastically deformed as the equation also implies, further asperity deformation during the sliding would likely occur and should contribute to the friction force. These limitations of the classical model suggest that a better method of predicting the friction coefficient for boundary lubricated systems needs to be developed.

1.2 Friction Coefficient of Boundary Lubricated Surfaces

Friction tests reveal that the friction coefficient of typical engineering surfaces in boundary lubricated situations is in the range 0.06 – 0.28. These values were obtained from running tests on a friction testing apparatus shown in Figure 1-2. The slider pin was AISI 52100 steel. Cartridge heaters inserted into the stage allowed for high temperature friction tests. Table 1.1 summarizes the measured friction coefficient of various lubricant-substrate combinations for various normal loads, sliding speeds, and temperatures. In the Cu/mineral oil case, high temperatures cause the friction coefficient to go up to levels comparable to dry sliding. This is a well known behavior of boundary lubricated systems. Beyond certain critical temperatures, it is believed that the lubricants desorb from the surface and no longer act as a lubricating medium.

In addition to the tests reported in Table 1.1, friction tests of two silicon (001) surfaces were performed. A small 1 mm × 1 mm piece of silicon wafer was glued to

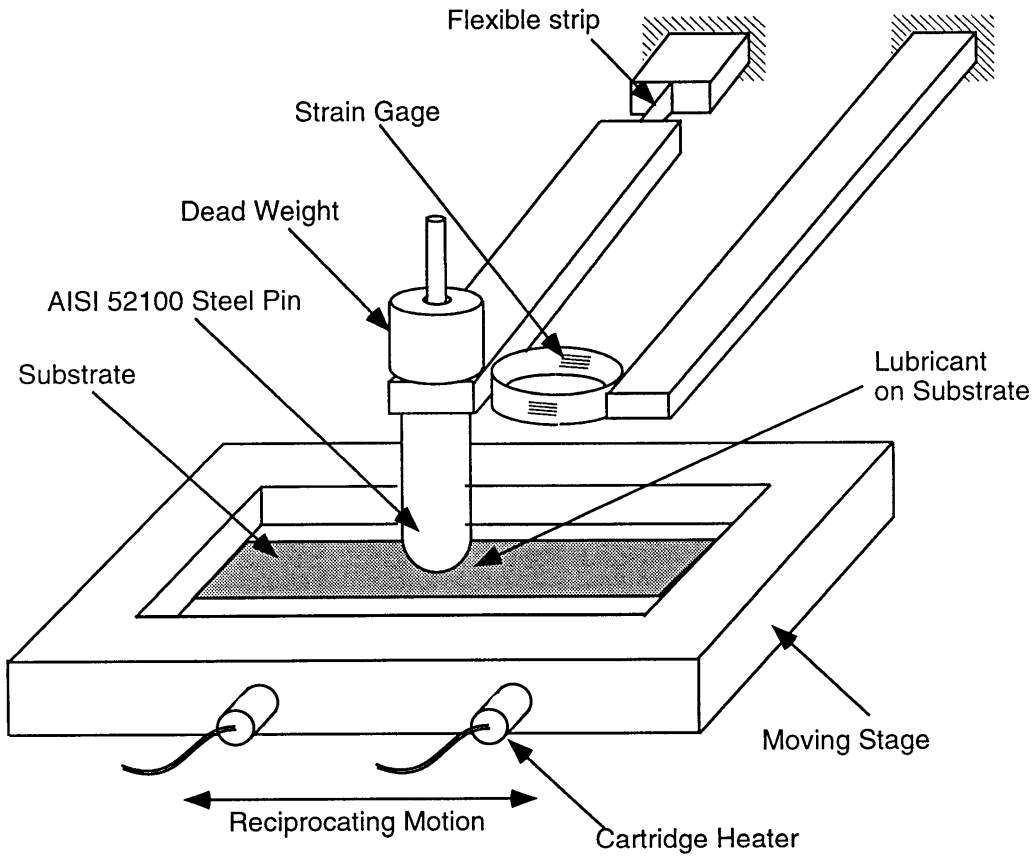

Figure 1-2: Schematic of friction test apparatus.

Table 1.1: Friction coefficient of various boundary lubricated surfaces. All tests were conducted using AISI 52100 steel pin.

Substrate/Lubricant	Load (N)	Speed (mm/s)	Temp. (°C)	μ
Silicon/Oleic acid	1.96	10.0	25	0.06
Silicon/Hexadecane	1.96	6.0	25	0.16
Silicon/Mineral oil	0.98	20.0	25	0.07
			75	0.11
			150	0.18
Silicon/Dodecane	3.92	5.0	25	0.28
		29.0		0.25
	0.98	20.0		0.22
			150	0.22
Copper/Mineral Oil	4.91	20.0	25	0.15
			50	0.18
			75	0.34
			100	0.50

Table 1.2: Friction coefficient of boundary lubricated silicon (001) surfaces. All tests were conducted at room temperature.

Lubricant	Load (N)	Speed (mm/s)	μ
None	0.49	4.7	0.16
	0.98		0.22–0.50
Dodecane	0.49	4.7	0.26
		17.9	0.26
		28.7	0.26
	0.98	4.7	0.29
		17.9	0.26
		28.7	0.26
	1.47	4.7	0.28
		17.9	0.25
		28.7	0.25
	1.96	4.7	0.29
		17.9	0.28
		28.7	0.27

the flattened tip of the steel pin. The friction coefficient was measured for dry sliding as well as for lubricated sliding with dodecane. The results are given in Table 1.2. The friction coefficient values in the dry sliding case vary depending on the amount of wear that takes place. When the wear is absent or too small to be detected by visual inspection, the friction coefficient is as low as 0.16. At higher loads, visible wear grooves develop and the friction coefficient rises to 0.5. One of the tasks of the lubricant is to substantially reduce the amount of wear, thereby keeping the friction coefficient at a low value.

1.3 Research Goals and Methodology

The present thesis is a contribution to a project aimed at investigating the molecular mechanisms of friction in boundary lubrication. The project comprises of two complementary techniques. The first is an experimental study by Raman spectroscopy to collect evidence of configurational changes that may occur in the lubricant film as a result of adsorption to the surface, as well as to applied load and shearing. The second is a molecular dynamics (MD) simulation study which gives an atomic resolution picture of the physical processes that occur in a boundary lubrication process. The vibrational spectra obtained from the Raman spectroscopy will be a valuable calibration aid for the empirical potential functions used in the molecular dynamics study, as shown by Sonwalkar, et al. [10]. Conversely, the atomic behavior observed by MD studies will serve to guide future Raman spectroscopy analyses. In this thesis, the molecular dynamics simulation studies are presented.

1.4 Present Developments in Molecular Tribology

Recently, there has been a push to understand the physics of friction at the molecular level [11]. Developments in experimental techniques, such as the atomic force microscopy (AFM), has enabled researchers to conduct friction experiments at the nanometer scale. In addition, molecular dynamics (MD) simulations have gained acceptance as an investigative tool for simulating frictional phenomena using systems of the order of nanometers.

In terms of theory, Tomlinson [12] was the first to propose a molecular model of friction. His model, based on three atoms described by some potential functions, attributed frictional dissipation to an unstable configuration which arises during the sliding motion. Later, the Frenkel-Kontorova [13] model incorporated a row of atoms interacting with each other through harmonic potentials in order to describe the atomic mechanics of friction. A similar model called the Independent Oscillator

model was proposed by McClelland [14], who described a "plucking" mechanism by which energy is dissipated. In the past decade, such simplistic models have been extended into more complex systems with MD simulations.

In 1990, Landman, et al. [15] conducted simulations of the contact formation of a nickel tip and a gold surface. They observed what they called a "jump-to-contact" phenomena when the tip had neared the surface, resulting in plastic deformation. They also simulated the sliding of nonuniform gold surfaces separated by a film of hexadecane, in what they called "nano-elastohydrodynamics" [16]. They observed the lubricant response to the shearing action of the asperities and calculated the friction forces. Although Landman's group was able to reveal valuable information regarding contact mechanics and elastohydrodynamics, their work did not directly address the problem of boundary lubrication.

Harrison, et al. [17] performed simulations of hydrogenated diamond surfaces in sliding and found that the relationship between the friction and normal forces varied with the crystallographic sliding direction. They observed the atomic trajectories of the hydrogen atoms and related the shape of the force curves to the relative motions of the hydrogen ends of the two surfaces. They next extended their system to include flexible hydrocarbon species chemically bonded to the surface and found that the friction coefficient behaves differently with load for different species attached to the surface [18]. Finally, Perry and Harrison [19] simulated the same system with mobile (CH_4) molecules trapped between the surfaces and found a significant reduction in the friction coefficient. A simulation study focused on the friction in AFM was performed by Kim and Suh [20], who calculated the friction coefficient for a single argon atom sliding over an argon lattice. The use of only one scanning atom and only a two-dimensional argon lattice limited the application of their results.

In the area of boundary lubrication, Glosli and McClelland [21] simulated two rigid substrates in sliding with a monolayer of lubricant fixed to each surface In their model, the lubricant molecules were n-alkanes of six monomers whose axes were oriented normal to the surfaces. They reported that the energy dissipation consists of a continuous viscous mechanism and a discontinuous plucking mechanism.

A similar system was used by Tupper and Brenner [22] to simulate self-assembled monolayers of alkanethiols on gold. They found the frictional force to be proportional to the applied load and suggested that the mode of dissipation was related to the oscillations of the chain tilt angles. In yet another similar study, Grest [23] simulated polymer brushes end grafted to sliding surfaces and calculated the resulting shear force as a function of the sliding velocity. Koike and Yoneya [24] conducted simulations of Langmuir-Blodgett monolayers on rigid SiO_2 and calculated the friction force of perfluorocarboxylic acid film to be three times that of hydrocarboxylic acid film.

In all these simulations of boundary lubrication, the ends of the molecules were assumed to be adsorbed on the surfaces in an ordered, standing manner. While this may be so for straight chain molecules with one polar end, it may not be true for all lubricant/substrate combinations. By fixing the molecule ends rigidly on the surfaces, these studies have ignored the effects of the lubricant-surface interactions on the behavior of the film. Furthermore, the substrate materials have been represented with atoms fixed in space to serve only as a base on which lubricant molecules were attached. Consequently, all of the focus was placed on the behavior of the molecules, while the role of the surface itself was ignored. It is believed that the properties of the surface are also important factors in the mechanisms of boundary lubrication [25]. Therefore, allowing the surface atoms to interact under realistic potential functions would make significant contributions to the simulation studies.

1.5 Problem Statement and Thesis Organization

The physics of lubricating films during frictional sliding still remains to be understood at the atomic scale. At present, there is little evidence regarding the preferred orientation of the molecules in a layer of lubricant adsorbed on a solid surface. The orientation could be a function of many variables such as the surface crystallography, molecular structure of the lubricant, pressure, temperature, and other environmental factors such as humidity. Additionally, the rheological behavior of the thin lubricant film while it is trapped between solid surfaces is not completely known at this

time. These and other factors of the lubricant-substrate interaction at the interface probably have a great deal of impact on the friction force during sliding.

In order to bring to light some of the atomic-resolution processes that occur in boundary lubricated sliding, a molecular dynamics simulation study has been carried out. This thesis gives a detailed account of the work. The thesis is organized into six chapters.

Chapter 1, the current chapter, contains background information on the classical theory of boundary lubrication, experimental values of friction coefficient, and MD literature review. **Chapter 2** reviews some key concepts in general molecular dynamics simulation techniques. All expressions for the potential functions and property calculations used in this work are presented in this chapter. **Chapter 3** discusses a preliminary molecular dynamics simulation study of two Lennard-Jones solids in sliding. **Chapter 4** presents results of validation simulations of bulk silicon and dodecane using the potential functions described in Chapter 2. Also, the procedure by which the silicon-dodecane interaction potential was obtained is discussed. **Chapter 5** discusses the simulation of the silicon- dodecane-silicon system in compression and sliding. **Chapter 6** gives concluding remarks and provides directions for future research.

Chapter 2

Molecular Dynamics Simulation

In a molecular dynamics simulation, the system consists of N discrete particles which represent either individual atoms or groups of atoms such as molecules. The particles are placed in a simulation cell of volume V which determine, together with the mass m of each particle, the density of the system. An illustration of a typical simulation cell is given in Figure 2-1. The particles are given initial positions and velocities, both of which can be assigned either deliberately or randomly. The sum of the individual particle kinetic energies is the kinetic energy of the system which is related to the temperature via the kinetic theory of gases, thus defining the two state properties density and temperature.

The potential energy Φ of the system is a function of the system configuration comprising $3N$ position coordinates,

$$\Phi = \Phi(\mathbf{r}_1, \mathbf{r}_2, \ldots, \mathbf{r}_N), \tag{2.1}$$

where $\mathbf{r}_i$ is the three-component cartesian vector defining the position of particle i. In this thesis, all vectors appear in lower case bold unless otherwise stated. The net force $\mathbf{F}_i$ on particle i is

$$\mathbf{F}_i = \frac{\partial \Phi}{\partial \mathbf{r}_i}, \tag{2.2}$$

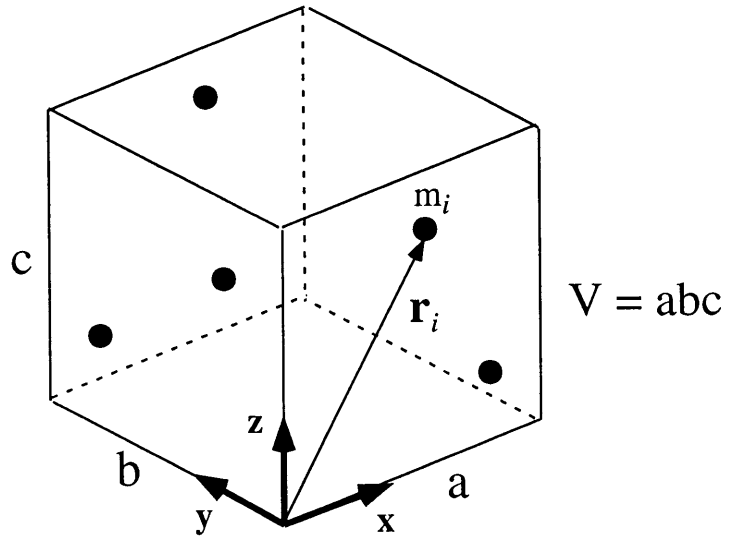

Figure 2-1: General schematic of an MD simulation cell.

and the particle obeys Newton's law of motion for a point mass,

$$\ddot{\mathbf{r}}_i = \frac{\mathbf{F}_i}{m_i}. \tag{2.3}$$

Given the potential function, the initial position coordinates and velocities, and the prescribed boundary conditions at the cell walls, the system evolves in time, tracing out a path in the position-velocity phase space. The particle positions and velocities can then be analyzed by statistical techniques to obtain such macroscopic properties as temperature, pressure, viscosity, and so on.

Complete discussions on the details of molecular dynamics simulations can be found elsewhere [26, 27]. Here, only the key points of MD simulation that are of particular relevance to the study of friction and boundary lubrication are presented.

2.1 Potential Functions

The most important feature of any MD simulation is the potential function that describes the interatomic interactions. Consequently, the most decisive step in a

simulation study is the proper selection of the potential function to model a given material. For a system of N discrete particles, the potential function Φ is usually written as a sum of n-body contributions,

$$\Phi = \sum_{i}^{N} \phi_1(\mathbf{r}_i) + \sum_{i<j}^{N} \phi_2(\mathbf{r}_i, \mathbf{r}_j) + \sum_{i<j<k}^{N} \phi_3(\mathbf{r}_i, \mathbf{r}_j, \mathbf{r}_k) + ... + \phi_N(\mathbf{r}_i, \ldots, \mathbf{r}_N), \qquad (2.4)$$

where ϕ_1, ϕ_2, ϕ_3, and ϕ_N are the one-, two-, three-, and N-body potentials, respectively. The notation $i < j$ used in the summation is shorthand for $i = 1, N;\ j = i + 1, N$. The one-body term ϕ_1, which accounts for the presence of such fields as electromagnetic or gravitational, are neglected in this work. The two-body term ϕ_2 represents all pairwise interactions among the N atoms, and the three-body term ϕ_3 represents all possible threesome interactions among the N atoms, and so on. It is reasonable to assume that in general the potential function improves as higher order terms are added, but the benefit comes at the expense of computational time and memory. In fact, the computational impracticality of the higher order terms has severely limited the suitability of potential functions which contain anything above three-body interactions. In this study, only the two- and three-body potentials were used.

2.1.1 The Lennard-Jones Potential Function

The most widely used two-body potential function in atomistic simulation is the Lennard-Jones (L-J) 12-6 potential function, which defines the potential energy between atoms i and j separated by distance r_{ij} as

$$\phi_{L-J}(r_{ij}) = 4\varepsilon \left[\left(\frac{\sigma}{r_{ij}} \right)^{12} - \left(\frac{\sigma}{r_{ij}} \right)^{6} \right]. \qquad (2.5)$$

The parameter ε is the potential well-depth which is related to the cohesive energy of the material, and σ is roughly the atomic diameter. These two parameters alone uniquely define the material. The powers 12 and 6 give rise to the name Lennard-Jones 12-6. Other forms such as Lennard-Jones 12-5 have been used in the past,

although not as frequently as the 12-6. It may be noted that the L-J is an *effective* pair potential rather than a *true* pair potential. An effective pair potential is a pair potential that has been calibrated with some bulk properties of the material. In the case of L-J, for example, the properties used in the fitting are the second virial coefficient and viscosity, and thus these properties are accurately reproduced even though only pairwise interactions are considered. However, the L-J still suffers from many of the limitations of pair potentials, such as the Cauchy discrepancy in elastic moduli calculations and the inevitable close-packed FCC crystalline structure which all pair potentials form.

The L-J 12-6 was first used in MD simulations by Rahman, who in 1964 matched experimental values of the pair correlation function, diffusion coefficient, and other properties of liquid argon to computational results [28]. It has been found since then that the L-J can be used to model essentially all noble gases in their solid, liquid, and gas phases. Thus in this work, the L-J 12-6 was used for argon and xenon in the study of dry sliding friction between two ideal solids.

2.1.2 The Stillinger-Weber Potential Function

The crystal lattice of silicon is well known to be diamond cubic, and since the L-J potential prefers the FCC structure, it is clear that a potential function of a different nature must be used to model solid silicon. In order to sustain an open structure like the diamond cubic, it is necessary to include more than just two-body terms. Stillinger and Weber [29] introduced the following potential function, including two- and three-body interactions, explicitly for Si which now bears their names,

$$\Phi_{SW} = \sum_{i<j} \varepsilon f_2(r_{ij}) + \sum_{i<j<k} \varepsilon f_3(\mathbf{r}_i, \mathbf{r}_j, \mathbf{r}_k), \tag{2.6}$$

The two-body function f_2 is expressed,

$$f_2(r_{ij}) = \begin{cases} \left[B\left(\frac{r_{ij}}{\sigma}\right)^{-p} - \left(\frac{r_{ij}}{\sigma}\right)^{-q}\right] \exp\left[\left(\frac{r_{ij}}{\sigma} - a\right)^{-1}\right], & 0 < \frac{r_{ij}}{\sigma} \leq a \\ 0, & \frac{r_{ij}}{\sigma} > a, \end{cases} \tag{2.7}$$

and the three-body function f_3 is expressed,

$$f_3(\mathbf{r}_i, \mathbf{r}_j, \mathbf{r}_k) = h(r_{ij}, r_{ik}, \theta_{jik}) + h(r_{ji}, r_{jk}, \theta_{ijk}) + h(r_{ki}, r_{kj}, \theta_{ikj}), \tag{2.8}$$

where

$$h(r_{ij}, r_{ik}, \theta_{jik}) = \begin{cases} \lambda \exp\left[\gamma\left(\frac{r_{ij}}{\sigma} - a\right)^{-1} + \gamma\left(\frac{r_{ik}}{\sigma} - a\right)^{-1}\right]\left(\cos\theta_{jik} + \frac{1}{3}\right)^2, & 0 < \frac{r_{ij}}{\sigma} \leq a \\ 0, & \frac{r_{ij}}{\sigma} > a, \end{cases} \tag{2.9}$$

and θ_{jik} is the angle formed by the three atoms i,j,and k with i as the vertex. The conditions stated to the right of Equations 2.7 and 2.9 for $\frac{r_{ij}}{\sigma}$ also apply to $\frac{r_{ik}}{\sigma}$. Table 2.1 lists the values of all of the constants in the above equations. The parameters ε and σ are not the Lennard-Jones parameters of silicon, although they carry similar meaning. The constants A, B, p, q, a, γ, and λ are the fitting parameters that were chosen by Stillinger and Weber according to two basic criteria. The first was that the potential must be most stable at the diamond cubic structure at low pressures, and the second was the reasonable reproduction of the melting temperature. Indeed, the SW potential successfully forms the diamond cubic lattice and it has been shown to predict the melting point of silicon accurately. An additional and unexpected attribute of the SW potential is its ability to model the elastic behavior of crystalline silicon. The elastic constants can be reproduced to reasonable agreement, as shown in Section 4.1.

Table 2.1: SW potential parameters. All energy units are normalized by the Boltzmann's constant.

ε	=	25 150 K
σ	=	2.0951 Å
A	=	7.049556277
B	=	0.6022245584
p	=	4
q	=	0
a	=	1.80
λ	=	21.0
γ	=	1.20

2.1.3 Hydrocarbon Potential Function

A simple model for complex alkanes utilizing the united atom method (UAM) was proposed by Siepmann et al. [30], in which the CH_3 and CH_2 groups are represented by pseudo-atoms so that the hydrogen atoms are not explicitly considered. The intermolecular part of the potential consists of two terms: ϕ_θ for the C-C-C angle bending and ϕ_φ for the torsion around a C-C bond. The bending term has a harmonic form,

$$\phi_\theta = \frac{1}{2} k_\theta \sum_i (\theta_i - \theta_0)^2, \tag{2.10}$$

where k_θ is the spring constant, θ_0 is the equilibrium value of the C-C-C angle θ, and the summation is over all θ_i present in the molecule. The torsional potential, originally developed by Jorgensen, et al. [31], has three contributions,

$$\phi_\varphi = \sum_i [a_1(1 + \cos\varphi_i) + a_2(1 - \cos 2\varphi_i) + a_3(1 + \cos 3\varphi_i)], \tag{2.11}$$

Table 2.2: United atom method parameters. All energy units are normalized by the Boltzmann's constant.

k_b	=	452 900 K/Å^2	b_0	=	1.540 Å
k_θ	=	62 500 K/rad^2	θ_0	=	1.99 rad
a_1	=	355.03 K			
a_2	=	-68.19			
a_3	=	791.32			
ε_{CH_3}	=	114.0 K	σ_{CH_3}	=	3.93 Å
ε_{CH_2}	=	47.0	σ_{CH_2}	=	3.93
† $\varepsilon_{CH_3-CH_2}$	=	73.2	$\sigma_{CH_3-CH_2}$	=	3.93

† $\varepsilon_{CH_3-CH_2} = \sqrt{\varepsilon_{CH_3}\varepsilon_{CH_2}}$, $\sigma_{CH_3-CH_2} = \frac{1}{2}(\sigma_{CH_3} + \sigma_{CH_2})$

where a_1, a_2, and a_3 are constants. In addition to these, Mundy, et al. [32] introduced the harmonic C-C bond stretching potential ϕ_b,

$$\phi_b = \frac{1}{2} k_b \sum_i (b_i - b_0)^2, \tag{2.12}$$

where k_b and b_0 are again the spring constant and the equilibrium bond length, respectively. Finally, there is a Lennard-Jones 12-6 potential for interactions between intermolecular pairs of atoms and intramolecular pairs of atoms separated by more than three bonds. Table 2.2 lists the constants and L-J parameters for the UAM model. An obvious limitation of the UAM is that it cannot be used to model the behavior of the hydrogen atoms. The hydrogen atoms may have an important influence on the way the molecules adsorb onto a surface. In addition, the motion of the hydrogen atoms need to be modeled in order to get the high frequency vibrational spectra of a system of molecules. Since the united atom method alone cannot supply such information, it is necessary to also employ a more sophisticated model for hydrocarbons.

The consistent force field (CFF) model developed by Lifson and Warshel [33, 34] does include the hydrogen atoms and was fitted to a large variety of experimental data including the vibrational frequencies of cycloalkanes. The intramolecular part of the CFF has the following form:

$$\begin{aligned}\phi_{intra} &= \frac{1}{2}k_b\sum_i(b_i-b_0)^2 + \frac{1}{2}k_\theta\sum_i(\theta_i-\theta_0)^2 + \frac{1}{2}k_a\sum_i(a_i-a_0)^2 \\ &+ \frac{1}{2}k_\gamma\sum_i(\gamma_i-\gamma_0)^2 + \frac{1}{2}k_\delta\sum_i(\delta_i-\delta_0)^2 \\ &+ \frac{1}{2}k_\varphi\sum_i(1+\cos 3\varphi_i). \end{aligned} \tag{2.13}$$

The subscript i has a different meaning for each term in Equation 2.13, implying in each case that the summation should include all terms present. For instance, the first term is the sum of all C-C bond lengths b_i in the molecule. The corresponding force constant is denoted by k_b, and b_0 is the equilibrium value of b. Similar notation is used for the C-C-C bending angle θ, the C-H bond length a, the C-C-H angle γ, and the torsional angle φ about a C-C bond. In addition, there is a Urey-Bradley (UB) type potential, ϕ_{UB}, for a pair of atoms i and j bonded to a common atom,

$$\phi_{UB} = k'_\theta\sum_i(\theta_i-\theta_0) + \frac{1}{2}\sum_{i,j}F_{ij}(r_{ij}-r^0_{ij})^2, \tag{2.14}$$

where the general variable F_{ij} represents the UB force constants F_{CC}, F_{CH}, and F_{HH}.

All atoms pairs bonded neither to each other nor to a common atom, including intermolecular pairs, interact through a Lennard-Jones 9-6 potential ϕ_{nb},

$$U_{nb}(r_{ij}) = \frac{\varepsilon}{2}\left[\left(\frac{\sigma}{r_{ij}}\right)^9 - \frac{3}{2}\left(\frac{\sigma}{r_{ij}}\right)^6\right]. \tag{2.15}$$

Finally, there is a long range Coulomb term which was ignored in this work. The CFF model was employed in an MD simulation study of butane by Ullo, et al. [35] to show good predictions of vibrational and transport properties at various conditions. The constants that appear in the potential functions of the CFF are listed in Table 2.3.

The CFF takes much more computational time than the united atom method, for

Table 2.3: CFF model parameters. All energy units are normalized by the Boltzmann's constant.

k_b	=	111,156 K/Å^2	b_0	=	1.540 Å
k_a	=	288,622	a_0	=	1.099 (for CH_2)
k_a	=	313,010	a_0	=	1.102 (for CH_3)
k_θ	=	15,923 K/rad^2	θ_0	=	1.95 rad
k_γ	=	25,496	γ_0	=	1.91
k_δ	=	39,807	δ_0	=	1.91
k_ϕ	=	585 K			
k'_θ	=	3,124 K			
F_{CC}	=	55,427 K/Å^2	r^0_{CC}	=	2.50 Å
F_{HH}	=	1,713	r^0_{CH}	=	1.80
F_{CH}	=	43,233	r^0_{CH}	=	2.20
ε_{CC}	=	93.0 K	σ_{CC}	=	3.548 Å
ε_{HH}	=	1.3	σ_{HH}	=	3.616
† ε_{CH}	=	11.0	σ_{CH}	=	3.528

† $\varepsilon_{CH} = \sqrt{\varepsilon_C \varepsilon_H}$, $\sigma_{CH} = \frac{1}{2}(\sigma_C + \sigma_H)$

the hydrogen atoms and all associated angles are modeled. A method of combining the UAM and CFF models in the interest of computational efficiency at a minimal sacrifice of the validity is presented in Section 4.2.

2.2 Boundary Conditions

The issue that remains to be addressed is how the particles respond when they approach the walls of the simulation cell. In principle, if the cell is made large enough to be of macroscopic dimensions, no special treatment at the boundaries would be necessary. However, this is impossible to achieve given the capacity and speed of the present computer hardware. The largest ensemble to have been simulated to date is on the order of 10^9 particles, which still is an insignificant fraction of the $\sim 10^{23}$ particles required to fill a macroscopic volume. Indeed, even a billion particle ensemble would still only be a microscale system. This poses a problem since results from simulations are useful only if they reflect macroscopic behavior. This problem is addressed by using proper boundary conditions which allow for the simulation of bulk material using only a small number (~ 100) of particles.

Bulk modeling using periodic boundary conditions

The concept of periodic boundary conditions allows the use of only a small simulation cell to model infinite space. Figure 2-2 is a two-dimensional representation of periodic boundary conditions; the extension to a three-dimensional case is straightforward. In the figure, box A is the simulation cell in which all N particles are placed. However, the simulation environment comprises not just box A, but identical images of box A surrounding it out to infinity, as shown in the figure. Thus the particles in box A must interact with not only the other particles in A but also with those in all the other boxes. This implies an infinite number of interactions; while this is true in principle, it is avoided in practice by establishing a cutoff distance, beyond which the particles no longer interact with each other. This is a valid simplification for almost all substances because the long-range attractive forces are small enough to be

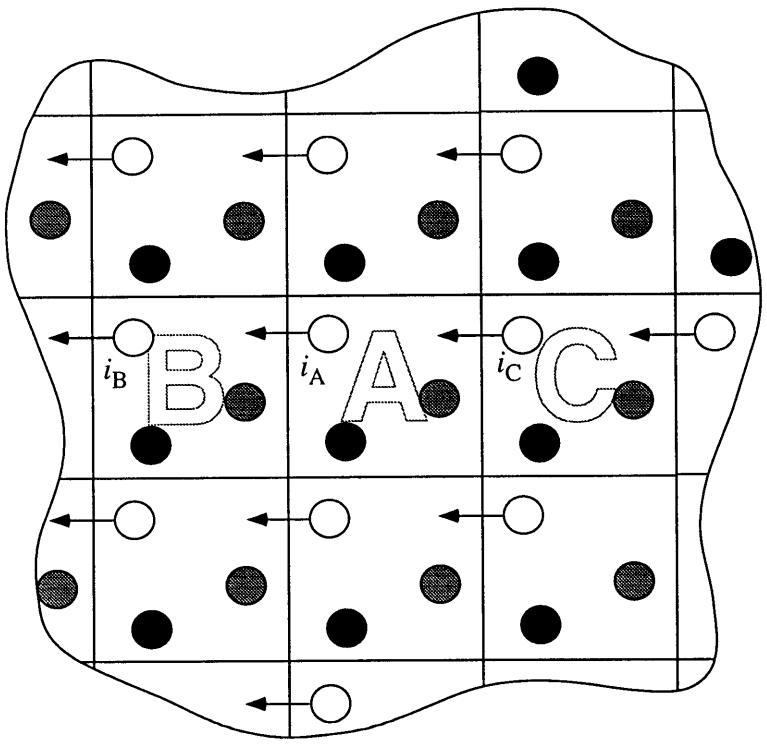

Figure 2-2: Schematic of 2-D periodic boundary conditions.

neglected in comparison with the stronger short-range forces.

In the course of the simulation, many of the particles will leave the simulation cell A into adjacent cells. An example of this is shown in Figure 2-2 where particle i_A has just moved from A into B across the boundary. At the same time, periodic boundary conditions require that the particle labeled i_C, which is the periodic image of i_A, crosses from C into A while i_B crosses out of B. Therefore the number of particles in each cell is always conserved. In using periodic boundary conditions with the cutoff distance, it is the general practice to follow what is called the minimum image criterion. This means that for a given interaction between particles i and j, particle i will interact with either j or one of its images, whichever is closer to i.

Modeling a bulk material using periodic boundary conditions is done under the assumption that the material is homogeneous to a degree, since identical images of the same cell replicate in space. The simulation creates an artificial periodicity with a wavelength equal to the length of the side of the cell. Thus an apparent limitation of using periodic boundary conditions is that the simulation yields only those properties

or characteristics of the material which have a wavelength equal to or less than by an integer factor of the simulation cell. However, this limitation is not too restricting in most cases, particularly for structural properties of crystals, provided that the shape and size of the simulation cell are identical to those of the unit cell. For instance, it is necessary to use a rectilinear simulation cell when modeling cubic crystals(FCC, BCC), while HCP crystals require the use of a hexagonal cell.

Semi-infinite and thin-film boundary conditions

In the study of friction, it is necessary to simulate for a semi-infinite body rather than a bulk material. This is accomplished by relaxing the periodic boundary conditions in the direction that coincides with the normal to the desired surface. In Figure 2-3(a), for example, the periodic boundary condition is relaxed in the z direction, while it is still in effect in the x and y directions. The $+\hat{z}$ surface is open to the environment, effectively making it a free surface. On the other hand, the $-\hat{z}$ surface is an ordered array of particles which are at all times fixed (or moving in concert when modeling sliding) in space according to the crystalline pattern of the given material. This combination of the free and fixed boundaries, as shown in Figure 2-3(a), was used in this work to model the substrates that slide against each other.

To treat the lubricant layer, thin-film boundary conditions shown in Figure 2-3(b) was used. The thin-film has periodic boundary conditions in the x and y directions while both surfaces in the z directions are free to interact. To set up the full substrate-lubricant-substrate boundary lubrication system, a stacked combination of the semi-infinite and thin-film boundary conditions were used such that the free surfaces of the thin-film interacted with the free surfaces of the semi-infinite substrates.

2.3 Parrinello-Rahman Method

Andersen [36] introduced the idea of making the simulation cell volume an additional dynamic variable in order to generate a constant pressure statistical ensemble rather than the conventional constant volume ensemble. His approach, limited to

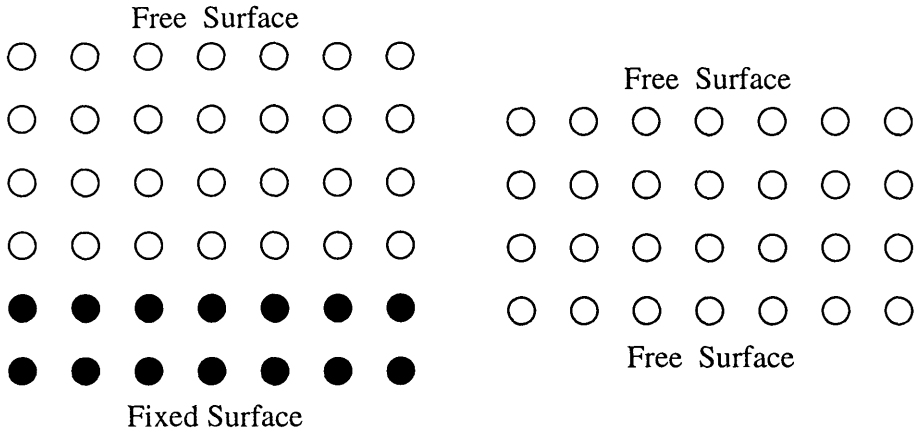

Figure 2-3: Schematic of semi-infinite and thin film boundary conditions. (a) semi-infinite boundary conditions and (b) thin film boundary conditions. Open circles represent particles that are free to move and filled circles represent fixed particles.

pure dilatation, was extended to allow non-uniform strain and shear deformations by Parrinello and Rahman [37, 38]. In their scheme, the spatial coordinates of N particles are completely specified by N number of $\mathbf{s}$ vectors and a 3×3 $\mathbf{H}$ matrix. The $\mathbf{s}$ vectors are the position vectors of the particles which have been mapped to a cube of unit length, and consequently all components of the $\mathbf{s}$ vectors fall between zero and one. The size and shape of the simulation cell is defined by the the vectors $\mathbf{a}$, $\mathbf{b}$, and $\mathbf{c}$, as shown in Figure 2-4, which are also the column vectors that make up the $\mathbf{H}$ matrix so that for particle i, the relationship between $\mathbf{s}_i$, $\mathbf{H}$, and the real-space position vector $\mathbf{r}_i$ is

$$\mathbf{r}_i = \mathbf{H}\mathbf{s}_i. \tag{2.16}$$

Taking into account the elements of $\mathbf{H}$ as nine additional variables, the equation of motion in s-space for particle i is

$$\ddot{\mathbf{s}}_i = -\frac{1}{m_i}\mathbf{G}^{-1}\frac{\partial \Phi}{\partial \mathbf{s}_i} - \mathbf{G}^{-1}\dot{\mathbf{G}}\dot{\mathbf{s}}_i, \tag{2.17}$$

where m_i is the particle mass, Φ is the system potential function, and $\mathbf{G}$ is a symmetric matrix defined as

$$\mathbf{G} = \mathbf{H}^{\mathrm{T}}\mathbf{H}, \tag{2.18}$$

where the superscript T denotes the transpose. In the H-space, the equation of motion is derived to be

$$W\ddot{\mathbf{H}} = (\mathbf{\Pi} - p)\mathbf{\Lambda} - \mathbf{H}\mathbf{\Sigma}. \tag{2.19}$$

W is called the wall mass that controls the rate of fluctuation of the cell dimensions, and p is the externally applied hydrostatic pressure. The matrix $\mathbf{\Lambda}$ is given by $\mathbf{\Lambda} = V\mathbf{H}^{\mathrm{T}\,-1}$, where V is again the volume of the cell which can be obtained by taking the determinant of $\mathbf{H}$. The internal stress tensor, $\mathbf{\Pi}$, is given by

$$\mathbf{\Pi} = \frac{1}{V}\left[\sum_{i}^{N} m_i \mathbf{v}_i \mathbf{v}_i^{\mathrm{T}} - \frac{\partial \Phi}{\partial \mathbf{H}}\right], \tag{2.20}$$

where $\mathbf{v}_i$ is the real-space velocity vector of particle i, obtained by $\mathbf{v}_i = \mathbf{H}\dot{\mathbf{s}}_i$. The first term inside the brackets is the kinetic contribution to the stress tensor, where a vector multiplication of the column vector, $\mathbf{v}$, itself produces the 3×3 tensor. The second term is the virial component which reflects the interatomic forces among the system atoms. The remaining term in Equation 2.19 is defined,

$$\mathbf{\Sigma} = \mathbf{H}_0^{-1}(\mathbf{S} - p)\left[\mathbf{H}_0^{\mathrm{T}}\right]^{-1} V_0, \tag{2.21}$$

where $\mathbf{H}_0$ and V_0 are the $\mathbf{H}$ matrix and the cell volume at time zero, $\mathbf{S}$ is the applied stress tensor, and p is again the applied hydrostatic pressure, which is also equal to $\frac{1}{3}\mathrm{Trace}(\mathbf{S})$.

2.4 Property Calculations

The information obtained from the simulation run consists only of the phase space trajectories (i.e. particle positions and velocities with respect to time) and is mostly uninformative until converted to continuum properties through statistical treatment.

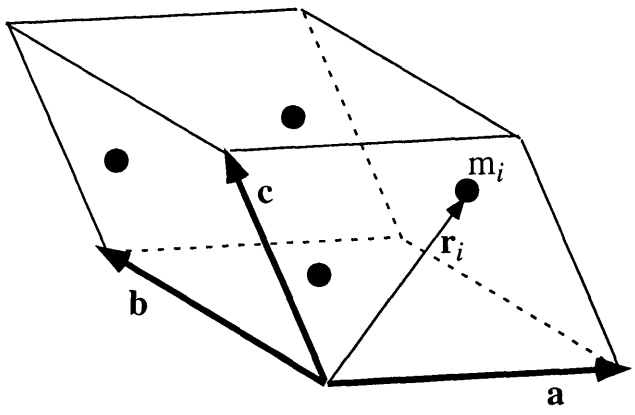

$$\mathbf{a} = (a_X, a_Y, a_Z)$$
$$\mathbf{b} = (b_X, b_Y, b_Z)$$
$$\mathbf{c} = (c_X, c_Y, c_Z)$$

$$\mathbf{H} = \begin{bmatrix} a_X & b_X & c_X \\ a_Y & b_Y & c_Y \\ a_Z & b_Z & c_Z \end{bmatrix}$$

$$V = \det \mathbf{H}$$

Figure 2-4: Schematic of a Parrinello-Rahman simulation cell.

There is a wide range of static, dynamic, and thermodynamic properties which can be calculated, and their derivations are discussed elsewhere [27, 39]. Due to the statistical nature of the equilibrium property calculations, it is necessary to collect data from several systems of the same ensemble to obtain an ensemble average. From the simulation perspective, this would involve making several runs, each with a unique initial condition, and averaging the results over all runs. However, for an ensemble in equilibrium, the ergodic hypothesis states that each system will eventually visit all the state points of the ensemble if given enough time. Therefore, the time average of one system becomes equal to the ensemble average as the run time approaches infinity. Thus in practice, equilibrium properties are extracted from the time average of a single run, provided that the run is of sufficiently long duration. The required duration can be determined by how well the desired property converges during the run to some equilibrium value. The properties calculated in this work rely on the ergodic hypothesis. In the following expressions for the properties calculated in this work, ensemble (or time) averaging is denoted by angle brackets, unless otherwise noted.

Radial Distribution Function

The radial distribution function $g(r)$, also called the pair correlation function, is the distribution of the separation distance r_{ij} between all pairs of of atoms i and j in the system. For a system of N particles

$$g(r) = \frac{1}{4\pi r^2 \Delta r} \left\langle \sum_{i<j}^{N} \delta(r - |\mathbf{r}_i - \mathbf{r}_j|) \right\rangle, \tag{2.22}$$

where Δr is a sufficiently small increment in r and δ is the Dirac delta function.

The radial distribution function is useful in determining the phase of the system. In the solid phase at some finite temperature, a system will exhibit distinguishable peaks up to the third or even fourth nearest neighbors. The shape of $g(r)$ is unique for each structure (FCC, BCC, etc.), so it can also be used to identify the crystal structure of the simulated material. Once the system melts and loses structural order, the $g(r)$ smears out so that only the first peak remains, its magnitude being significantly lower than what it had been for the crystal.

Static Structure Factor

Another way of determining the structural order in a system is to calculate the static structure factor $S(\mathbf{k})$,

$$S(\mathbf{k}) = \frac{1}{N^2} \left| \sum_{j}^{N} \exp(i\mathbf{k} \cdot \mathbf{r}_j) \right|^2, \tag{2.23}$$

where i is the imaginary number $\sqrt{-1}$. The wave vector $\mathbf{k}$ must be so chosen that $S(\mathbf{k}) = 1$ for a perfectly crystalline system; if the system experiences disorder, the structure factor decreases in value toward zero. Usually the magnitude of $\mathbf{k}$ can be chosen to be $4\pi/a$ where a is the lattice parameter of the crystal, and the direction of $\mathbf{k}$ can be whichever is most applicable to the analysis. With the proper selection of $\mathbf{k}$, the static structure factor can be monitored throughout the run to determine if and when the system loses its structural periodicity.

Mean Squared Displacement

The mean squared displacement $< \Delta r^2 >$ tracks as a function of time t the displacement of the particles from their initial positions,

$$< \Delta r^2(t) >= \frac{1}{N} \sum_i |\mathbf{r}_i(t) - \mathbf{r}_i(0)|^2 . \tag{2.24}$$

The Δr^2 used here to denote the mean squared displacement is not related to the Δr that appears in the expression for the radial distribution function. Also, the angle brackets in this expression denotes particle averaging rather than ensemble (or time) averaging. The mean squared displacement is another way to determine the phase of the system. A system in solid phase will have a curve which oscillates about or plateaus to some value while the liquid phase curve will continuously increase.

Temperature

The temperature is taken from the equipartition theorem,

$$T = \frac{1}{3Nk_B} \left\langle \sum_i m_i \mathbf{v}_i \cdot \mathbf{v}_i \right\rangle . \tag{2.25}$$

Pressure

The pressure is the sum of the kinetic term and the virial term,

$$p = \frac{1}{3V} \left\langle \sum_i (m_i \mathbf{v}_i \cdot \mathbf{v}_i + \mathbf{r}_i \cdot \mathbf{F}_i) \right\rangle , \tag{2.26}$$

and is also equal to $\frac{1}{3}\text{Trace}(\mathbf{\Pi})$, where $\mathbf{\Pi}$ is obtained from Equation 2.20.

Velocity Autocorrelation Function

The velocity autocorrelation function $\chi(t)$ for a particle is

$$\chi(t) = \langle \mathbf{v}(0) \cdot \mathbf{v}(t) \rangle . \tag{2.27}$$

This autocorrelation function can be transformed with techniques such as Fourier

Transform and Maximum Entropy Method to yield the vibrational frequency of the particle [40]. When computing the velocity autocorrelation function to be used for spectral analysis, it is desirable to calculate it using several starting points and then compute the average of the set so that noise in the data can be minimized. In addition, the system should be in a well equilibrated state before any correlation functions are initiated.

Shear Viscosity

The shear viscosity η is given by the generalized Green-Kubo formula

$$\eta = \frac{V}{10k_BT}\int_0^\infty \langle \text{Trace}[\tilde{\mathbf{P}}(t)\tilde{\mathbf{P}}(0)]\rangle, \tag{2.28}$$

where $\tilde{\mathbf{P}}(t)$ is the deviatoric part of the stress tensor $\mathbf{\Pi}$ from Equation 2.20. The integral should be performed for a long enough time to allow the computed viscosity to converge to an equilibrium value.

Friction coefficient

For a body with a surface whose normal vector is $\mathbf{n}$, the traction stress $\mathbf{t}$ acting on the surface is related to the stress tensor $\mathbf{\Pi}$ in Equation 2.20 by,

$$\mathbf{t} = \mathbf{\Pi n}, \tag{2.29}$$

For homogeneous systems where the stress is uniform throughout the body, the force acting on the surface is just the traction multiplied by the surface area. It follows that the magnitudes of the friction force F and the normal load N on a surface lying parallel to the $x-y$ plane are given by

$$F = \Pi_{13}A, \tag{2.30}$$

and

$$N = -\Pi_{33}A, \tag{2.31}$$

where the tensor indices 1 and 3 correspond to the cartesian coordinates x and z, respectively. The ratio F/N is called the friction coefficient and is denoted by μ.

The friction force calculated in these simulations is qualitatively different from an experimentally measured friction force. In an experiment, the asperity contacts are not atomically flat like in the simulated system. Consequently, plastic deformation and possibly wear could contribute to the measured friction in the real system. In addition, real asperities contain such imperfections as grain boundaries which serve as nucleation sites for slip and deformation, further increasing the work required to slide surfaces over one another. Therefore, it is reasonable to expect lower friction in ideal, simulated systems.

2.5 Monte Carlo Simulation

The initial particle positions for the MD simulations are usually assigned according to some known crystalline pattern in cases where a single crystal is modeled. For the modeling of interfaces or liquids, however, the initial configuration is not so easily determined, as a purely random configuration may take too long to reach equilibrium or get trapped in a phase-space bottleneck. For this reason, Metropolis [41] monte carlo (MC) simulations are used at times in this work to generate the initial configuration for an MD run.

MC is a simulation technique which stochastically generates the minimum potential energy configuration of a system of particles. The procedure is to randomly assign a displacement to one of the particles of the system. The potential energy of the system before and after the move are compared. If the move has resulted in a lower system potential energy, the move is accepted. On the other hand, if the move has increased the system potential energy, the move is accepted only with a probability determined by the Boltzmann distribution.

MC is different from MD in that it does not include the kinetic energies of the particles in the energy calculation, in essence considering the temperature of the system to be zero. The advantage of using MC over MD is much less computing

time, and the disadvantage is the loss of the dynamic side of the system such as vibrations and temperature. A combined use of MC and MD allows us to benefit from the advantages of both methods. Further details of MC simulations can be found elsewhere [27, 41].

Chapter 3

Simulation of Ideal Solids in Sliding

Molecular dynamics simulations of two solid materials were carried out in order to obtain information concerning the interface formation and sliding between two dissimilar solids. Figure 3-1 shows the present system and Table 3.1 lists all the relevant properties and parameters of the simulation.

The materials were argon and xenon, both represented by the 12-6 Lennard-Jones potentials. The L-J parameters for these materials, obtained from the work of Hogervost [42], are given in Table 3.2. The combined potential for the interaction between argon and xenon is also a 12-6 Lennard-Jones. The parameters for the combined potential were obtained using Kong's combining rules [43], which is an extension of the more common geometric mean method. In his approach for combining potentials for A and B, the repulsive part of the potential, ϕ_{AB}^{rep}, is based on a model of atomic distortion such that,

$$\phi_{AB}^{rep}(r) = \frac{1}{2}\left[\phi_{A}^{rep}(2\gamma_1) + \phi_{B}^{rep}(2\gamma_2)\right], \tag{3.1}$$

where r is the separation distance between atom A and B. The parameters γ_1 and γ_2 satisfy,

$$\gamma_1 + \gamma_2 = r, \tag{3.2}$$

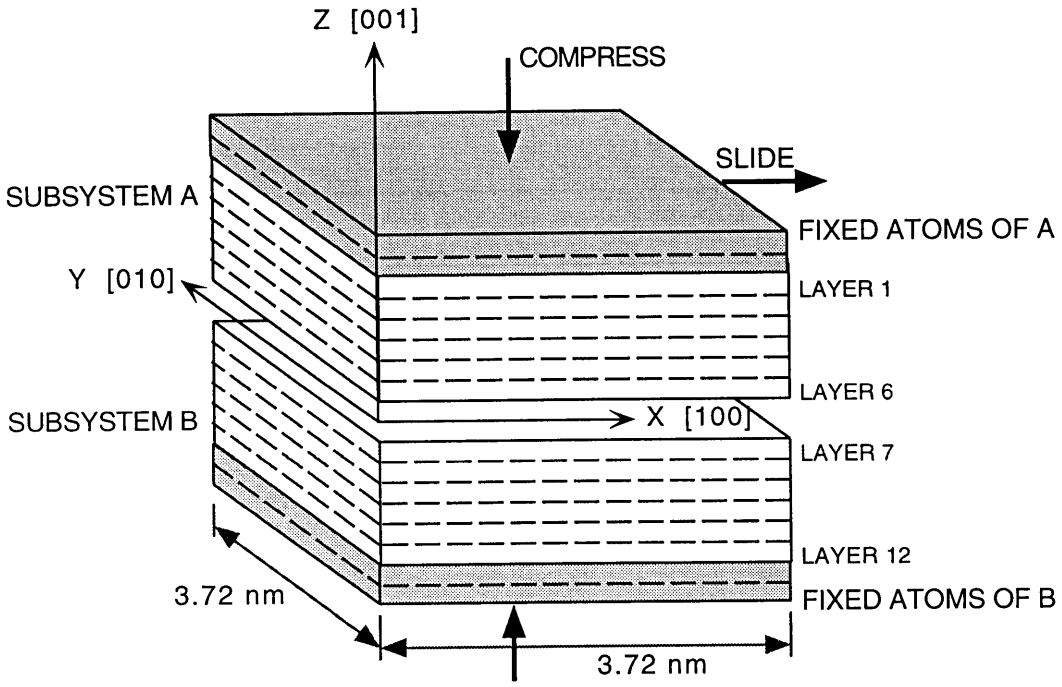

Figure 3-1: Schematic of Ar-Xe system.

Table 3.1: Ar-Xe system parameters.

	Ar	Xe
Number of atoms	588	432
Number of layers	6	6
Number of fixed layers	2	2
Density (kg/m^3)	1,763	3,651
Crystal structure	FCC	FCC
Lattice parameter (Å)	5.32	6.20
Temperature (K)	24	
Time increment (s)	1.08×10^{-15}	

Table 3.2: L-J parameters of Ar-Xe system.

	σ(Å)	ε/k_B(K)
Ar	3.405	120.0
Xe	4.100	221.0
Ar-Xe	3.785	150.7

and

$$\left[\frac{d\phi_A^{rep}(r)}{dr}\right]_{r=2\gamma_1} = \left[\frac{d\phi_B^{rep}(r)}{dr}\right]_{r=2\gamma_2}. \tag{3.3}$$

The attractive part of the combined potential, ϕ_{AB}^{att}, is the geometric mean, i.e.,

$$\phi_{AB}^{att}(r) = [\phi_A^{att}(r)\phi_B^{att}(r)]^{1/2}. \tag{3.4}$$

Kong's method offers an advantage over applying the geometric mean to the entire potential in that the short range repulsive forces are better represented. The combined L-J parameters calculated using this method are listed in Table 3.2. Figure 3-2 shows the plots of all three potentials.

Semi-infinite boundary conditions (see section 2.2 were used to model both materials such that periodic boundaries extended in the x and y directions, and the free surfaces of the two materials met at the $z = 0$ plane. The cell dimensions, aside from the compression stage, were kept constant, and the Parrinello-Rahman method was not used for this study. The initial positions of the atoms were arranged in FCC crystalline pattern with the [100], [010], and [001] crystal directions coincident with the x, y, and z cartesian directions, respectively. The equations of motion were integrated in time using a fifth-order Gear predictor-corrector method. To reduce computation time, a cutoff ratio of 2.5 was enforced on all potential functions, and the potentials and forces were shifted accordingly to remove the resulting discontinuities. In addition a Verlet neighbor list, updated at every ten time steps, was used for further reduction of computation time.

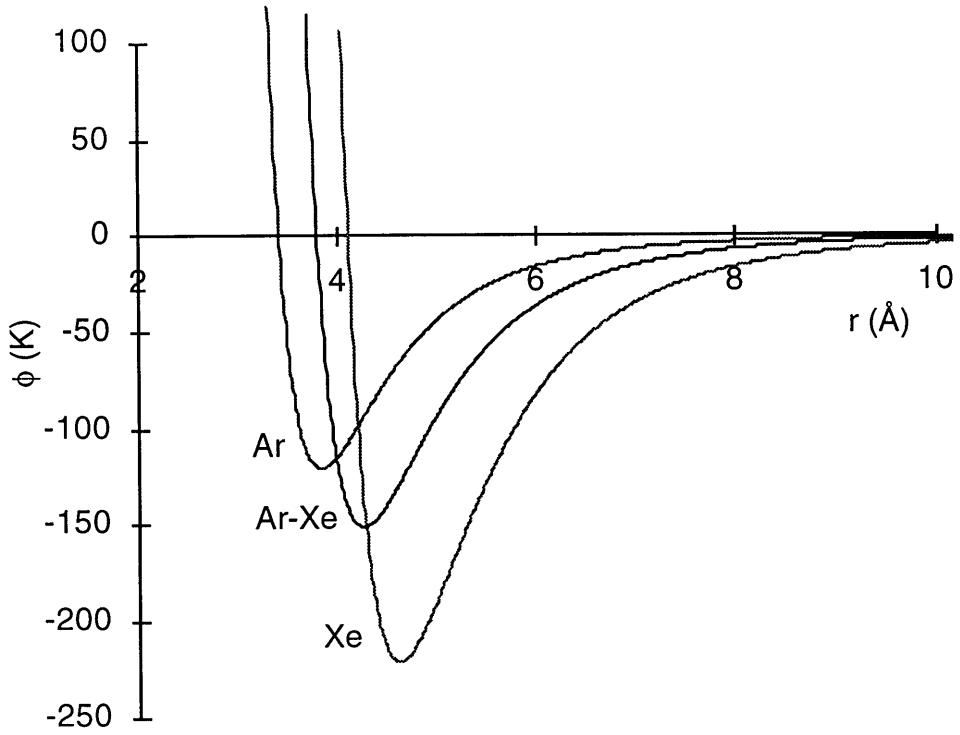

Figure 3-2: L-J potential functions for Ar-Xe system.

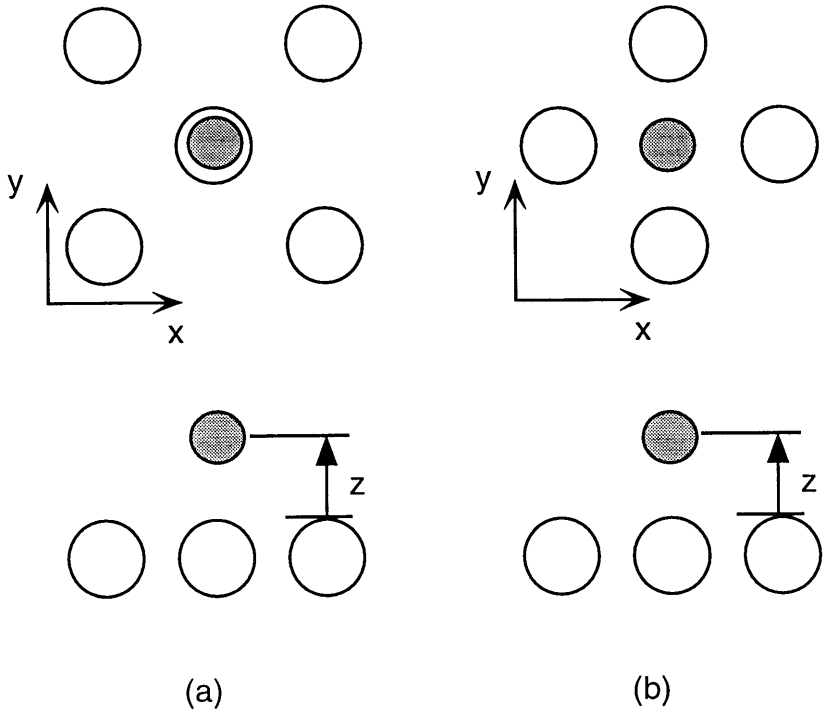

Figure 3-3: Schematic of on-top and hollow-site geometries.

3.1 Single Atom Simulation

Before forming the full interface between the argon and xenon surfaces, it is informative to determine which equilibrium configuration is preferred by a single argon atom on the xenon surface. In order to investigate this matter, a study of the potential energies of an argon atom at various positions suspended above the xenon surface was performed. According to Holloway, two limiting configurations exist for a foreign atom or molecule on a crystal lattice [44]. One is the "on-top geometry" where the foreign atom sits directly on the top of one of the surface atoms, shown in Figure 3-3(a). The other is the "hollow-site geometry" where the foreign atom sits in one of the valleys of the crystal surface, shown in Figure 3-3(b). The on-top geometry was first tested by placing a single argon atom directly above one of the surface xenon atoms. With its x and y coordinates held fixed, the potential energy of the argon atom at different values of z was computed. Since there are no other argon atoms, the

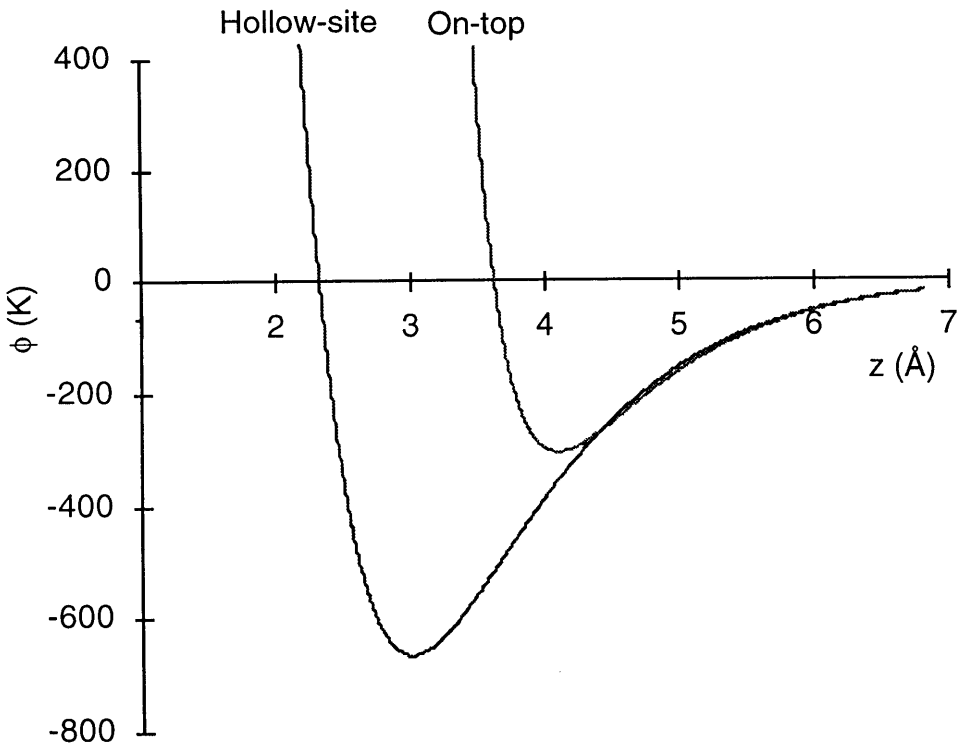

Figure 3-4: Potential energy of on-top and hollow-site geometries. z is the vertical distance between a single argon atom and the xenon surface.

calculated potential energy is all due to the interaction with the xenon surface. Next, this same simulation was carried out, this time with the argon atom situated above a hollow site. The results for the two cases, compared in Figure 3-4, show that the argon atom has lower potential energy in the hollow-site geometry than the on-top geometry for most of the range of z. Since systems are always seeking lower energy states, it was concluded that a single argon atom, when left to interact with the xenon surface, prefers the hollow-site geometry. This conclusion was confirmed by a series of MC simulations, which showed that for various starting positions, the argon atom always settles in a valley. This tendency is characteristic of the close-packing nature of Lennard-Jones systems.

Table 3.3: Static structure factor of Ar-Xe layers. The values of the $\mathbf{k}$ vectors are: 0.376 $\text{Å}^{-1}\hat{\mathbf{y}}$ for Ar; 0.322 $\text{Å}^{-1}\hat{\mathbf{y}}$ for Xe.

Layer	1	2	3	4	5	6	7	8	9	10	11	12
$S(\mathbf{k})$	0.95	0.93	0.92	0.93	0.92	0.73	0.94	0.97	0.97	0.97	0.97	0.97

3.2 Interface Formation

In forming the full interface between the argon and xenon surfaces, there was an artificial constraint on the cell dimension due to the use of periodic boundaries. For two semi-infinite cells with periodic boundary conditions, a stable interface can be established only if the cells have matching periodicity in the directions where the periodic boundary conditions are applied. For instance, if the cells are periodic along x, their simulation cells must be of the same length along x so that atom i and all its periodic images see the same environment. For the present system with periodic boundary conditions in x and y, the x lengths as well as the y lengths of the simulation cells had to be identical.

Having satisfied the periodicity requirement, the interface was formed with 500,000 MC steps followed by 40,000 MD steps. The initial configuration was that of perfect FCC crystal configurations, shown in Figure 3-5. Initially, the separation of the two surfaces was 3.785 Å. Figure 3-6 shows the configuration of the system after the interface was formed. There is clearly noticeable disorder, particularly in the argon lattice, due to the formation of the interface. The level of disorder in each layer was quantified by computing the static structure factor, $S(\mathbf{k})$ for each of the layers. The results, given in Table 3.3, show that the argon layer of greatest structural disorder is the interface layers 6 and the xenon layer of greatest disorder is layer 7. The disorder occurs due to the mismatch of lattices at the Ar-Xe interface. In forming the incommensurate interface, many of the atoms at the contact region have been forced out of their lattice positions. As a whole, the argon undergoes more disorder than the xenon, which is evident in both Figure 3-6 and Table 3.3. As further evidence

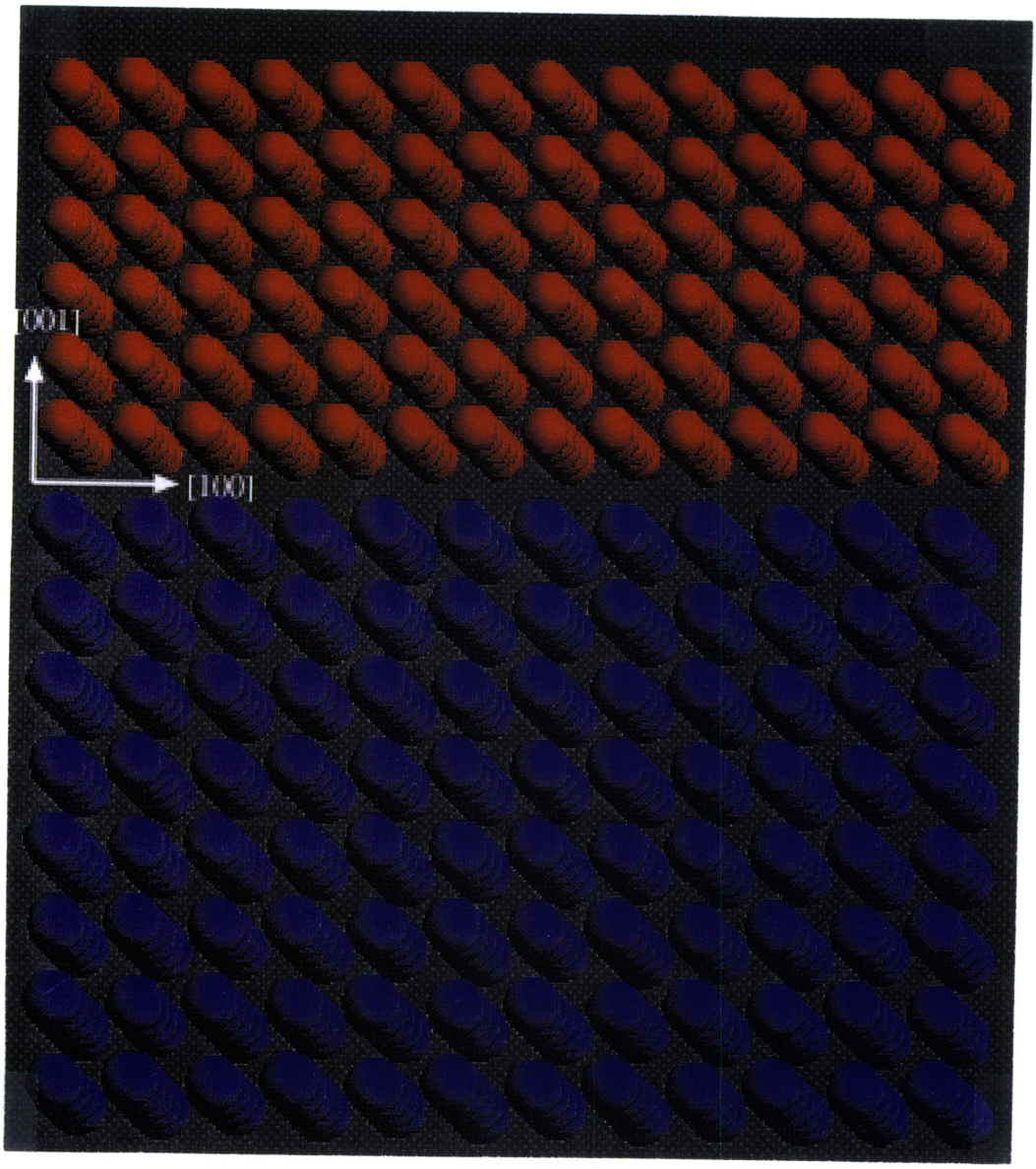

Figure 3-5: Ar-Xe system before interaction. Argon atoms are in red, xenon in blue.

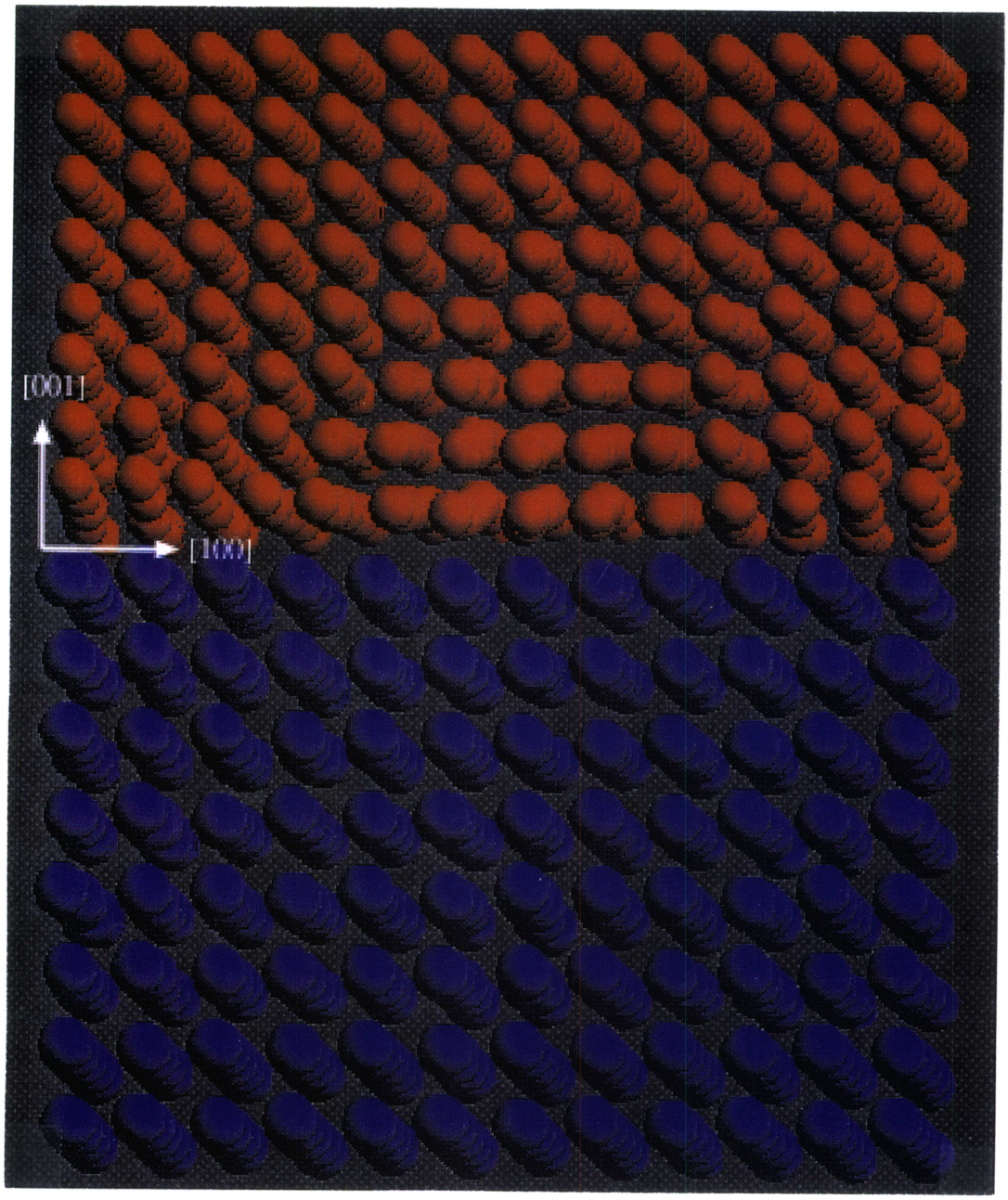

Figure 3-6: Ar-Xe system after interaction.

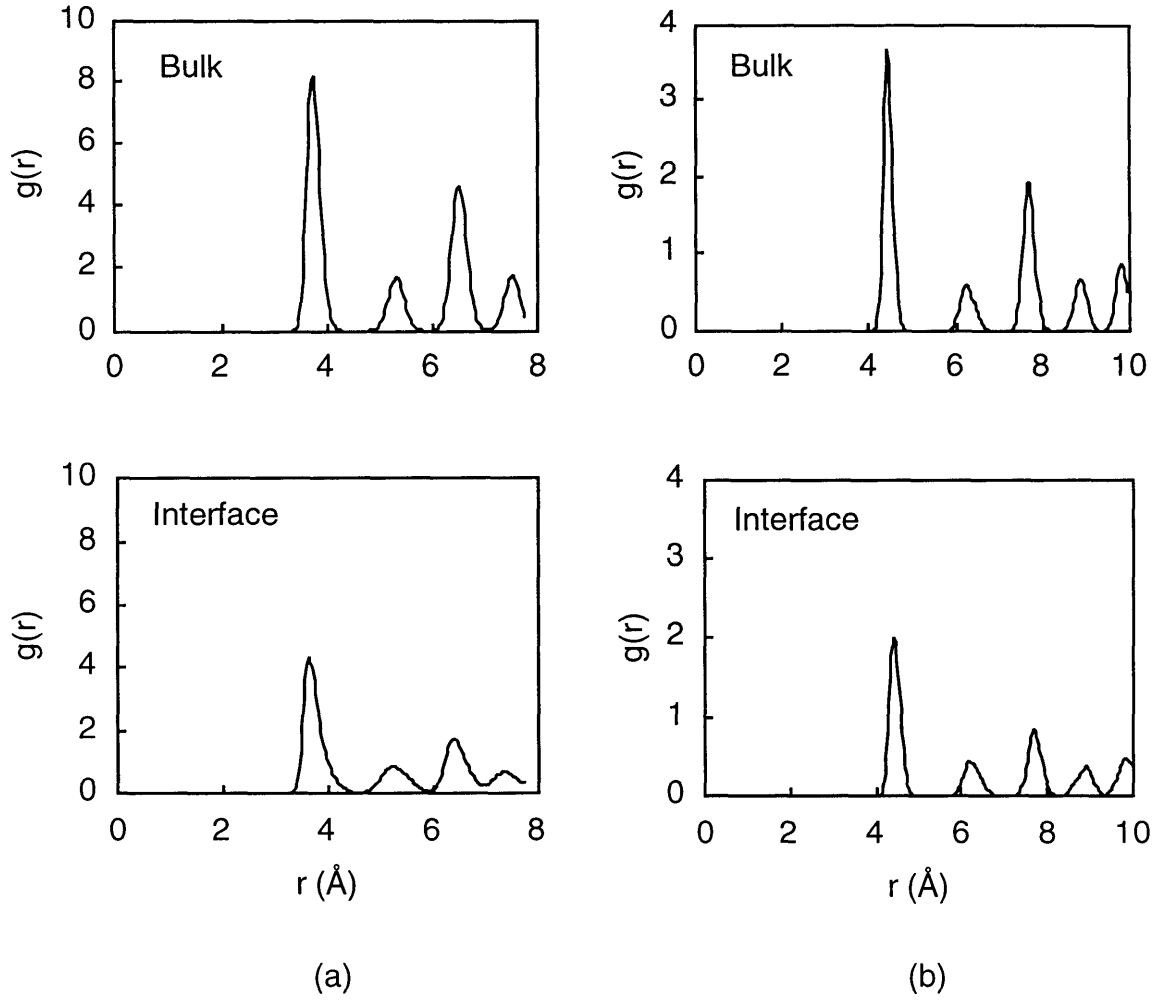

Figure 3-7: Radial distribution function of Ar-Xe system. (a) argon (b) xenon

of the disorder at the interface, Figure 3-7 shows the radial distribution function, $g(r)$, for the interface layers compared with the bulk region. For both materials, the radial distribution function loses the sharp features at the interface, signifying that the structural order which exists in the bulk region is less ordered in the interfacial region.

Without any Ar-Xe interactions, the minimum energy configuration for the system was achieved when the two materials were in the FCC crystal form. With the introduction of Ar-Xe interactions, the system must also account for the interfacial energy ϕ_{Ar-Xe} in the energy minimization. The perfect FCC structures are no longer the lowest potential energy configurations. Instead, the materials get distorted at

the junction as the system minimizes its energy. The primary reason for the disorder is the different lattice parameters of the two materials. The lattice mismatch forces disorder because incommensurate surfaces have high interfacial energy. As a whole, argon undergoes more disorder than xenon, which is evident in both Figure 3-6 and Table 3.3. This is due to the fact that the argon potential function has a well depth of 120 K compared to the xenon potential, which has a well depth of 221 K. Since the binding energy of xenon is about twice as high as that of argon, the latter takes less energy to deform. Consequently, the system creates more deformation of the argon in order to minimize the energy.

Figure 3-6 also shows that the interface layer of argon seems to be warped. The reason for this is evident in Figure 3-8, which shows the top view of the interface layers 6 and 7. The interfacial argon atoms are distributed in many configurations with respect to the underlying xenon surface. Some are in the on-top position, others are in the hollow-site position, and the rest are somewhere in between. The few argon atoms in the hollow site positions tend to bond nearer to the xenon surface to achieve lower interfacial potential energy (see Figure 3-4). On the other hand, the argon atoms in the on-top positions prefer to be further away from the surface. These competing factors result in the warping of the argon interface. The low stiffness of argon allows its interface to deform. On the other hand, xenon is too stiff for any warping at the interface to occur.

3.3 Compression and Sliding

The equilibrated interfacial system was next compressed in the z direction by subjecting the system to a uniaxial normal strain, ϵ_{zz}, of -0.002. The strain was imposed by scaling the z coordinates of all of the atoms in the system by a factor of 0.998. Subsequently, a run of 40,000 time steps was performed to bring the system to a state of equilibrium. Each time step was 1.08×10^{-15} s. A strain of 0.002 was chosen because it is the strain that corresponds to the yielding stress for many materials. The asperities of contacting surfaces are believed to be mostly in a state of yielding.

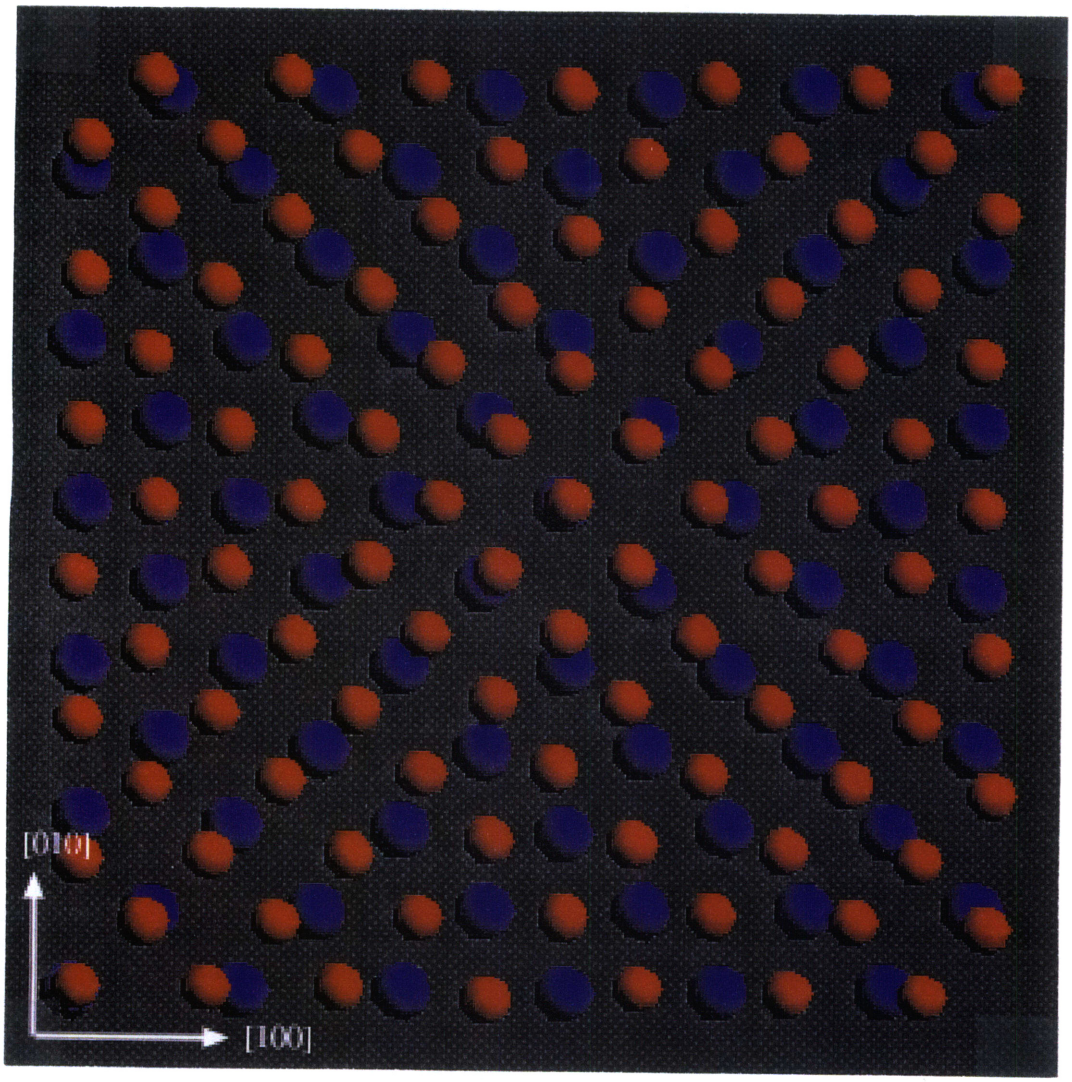

Figure 3-8: Ar-Xe interface: top view.

Since the present system is a model of an asperity, it was logical to compress close to the yielding strain.

The next step was to create sliding by displacing the fixed atoms of argon incrementally in the $+x$ direction. All the other atoms in the system were left to respond to the sliding motion of the argon boundary. A displacement of 0.53 Å was imposed after every 10,000 time steps, which corresponds to a sliding speed of 4.9 m/s. A total of ten such displacements were taken, giving the system a total sliding distance of 5.3 Å, equivalent to the lattice parameter of argon. The high sliding speed was due to computational limitations. The temperature was held constant at 24 K in order to prevent heating and melting of the materials due to the excessive sliding speed.

The instantaneous friction and normal forces per unit area were calculated during the sliding process, and the results are shown in Figure 3-9. The vibration of the particles creates a significant amount of noise in the force calculations. The noise can be reduced by taking the time average of the forces, shown in Figure 3-10.

These force calculations were obtained by summing the tangential and normal components of the Ar-Xe interaction forces at the interface. (The method introduced in section 2.4 was not used here because the stress tensor was not calculated for this part of the study.) Since the sliding takes place at every 10,000 time steps, the friction force calculations reflect the Ar-Xe interatomic forces at the interface as the system relaxes to equilibrium in response to each sliding displacement. The work energy needed to slide is converted into thermal energy and immediately dissipated out of the system via the velocity rescaling, which occurs at each time step. An alternative way of calculating the friction would be to compute the energy that is dissipated during the 10,000 time steps of relaxation, and then divide by the distance travelled. However, this method would be very sensitive to the interfacial temperature, which, for this system, was set to 24 K in order to prevent melting. Since it was not possible to accurately predict the interfacial temperature of sliding surfaces, the force-approach, which is not quite so dependent on the temperature, seemed to be a better choice of calculating friction.

Table 3.4 summarizes the the numerical friction experiment data. The friction

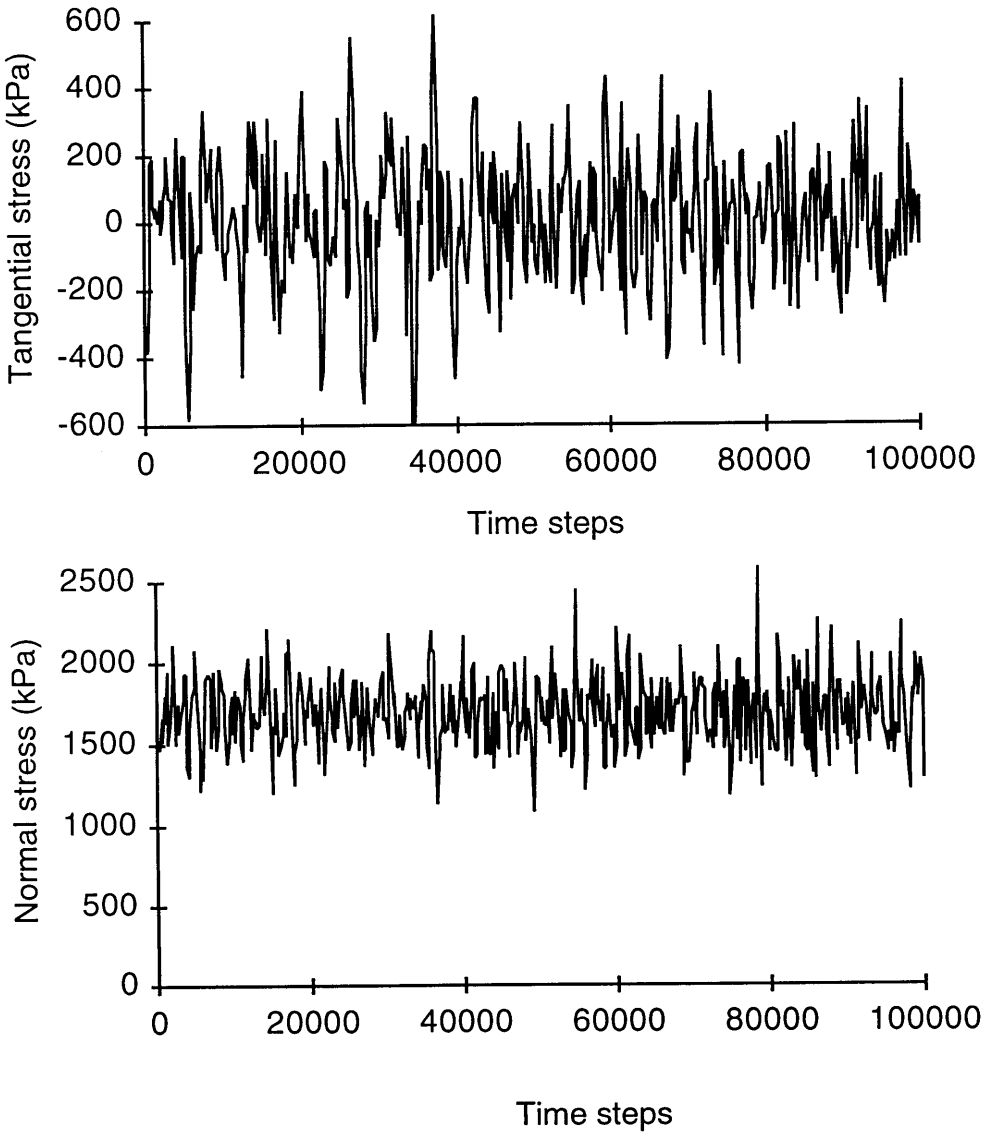

Figure 3-9: Instantaneous tangential and normal stresses in Ar-Xe sliding. Plots are for the entire sliding simulation.

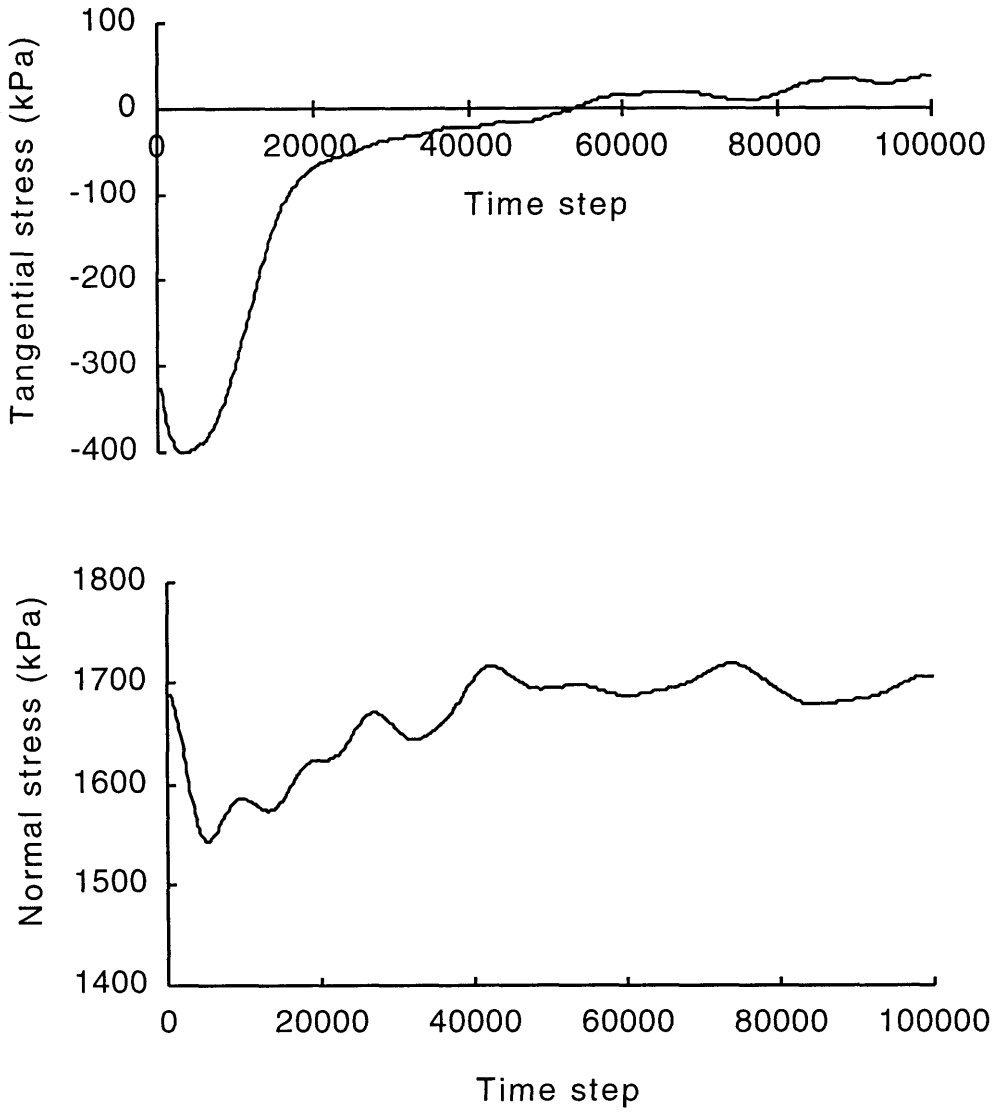

Figure 3-10: Average tangential and normal stresses in Ar-Xe sliding. Forces are time averaged cumulatively. Plots are for the entire sliding simulation.

Table 3.4: Summary of Ar-Xe sliding experiment.

Sliding direction	[100]
Sliding speed	4.9 m/s
Total sliding distance	5.3 Å
Average tangential stress	38.9 kPa
Average normal stress	1,708 kPa
Friction coefficient	0.023

coefficient for this case was 0.023, which is very low compared with the typical value for dry sliding of solid surfaces, which lies in the range 0.4 – 0.6. One source of the discrepancy lies in the potential functions used in the simulations, which are more suitable for noble gases rather than metallic solids used in tribological applications. Furthermore, the friction force calculated in the simulation was due only to elastic interactions. There was no wear nor permanent deformation, as will be shown later. Finally, calculating the friction force after the energy dissipation is an addition reason for the low values of friction.

Figure 3-11 is a plot of the layer-by-layer mean squared displacement of the system during the sliding. The argon (Layers 1-6) moves mostly as a bulk body while the xenon (Layers 7-12) essentially stays fixed. The distinct transition from Layer 6 to Layer 7 shows that shearing and breaking occurs between the argon and xenon interface layers. The mismatch of the lattices at the interface weakens the Ar-Xe bonds, so that they are most vulnerable to breaking in the event of sliding.

Figures 3-12 through 3-16 show the side view of the system during the sliding motion. Argon continues to experience more deformation than xenon throughout the sliding process. The argon interface layer remains warped throughout the sliding. Figure 3-17 shows a side view of the interface atoms during the sliding. It can be seen that during the course of the sliding, the argon interface gets continuously distorted from one warped form to another. It seems that the warped shape of the interface provides a resistance to the sliding motion, thereby contributing to the friction force.

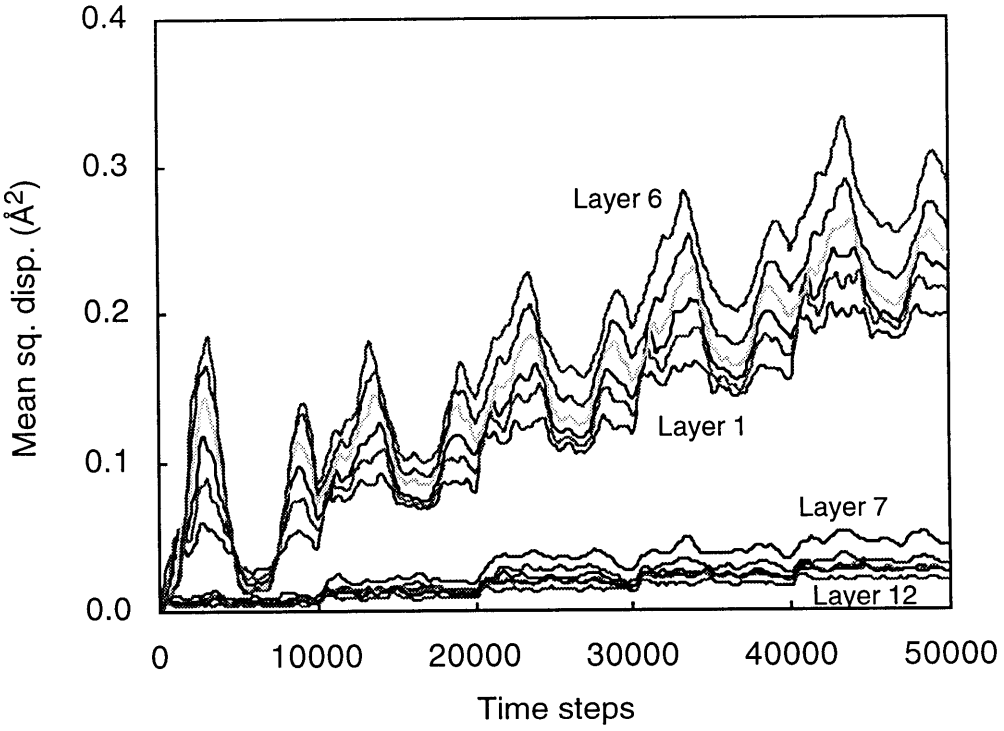

Figure 3-11: Mean squared displacement of argon and xenon layers during sliding.

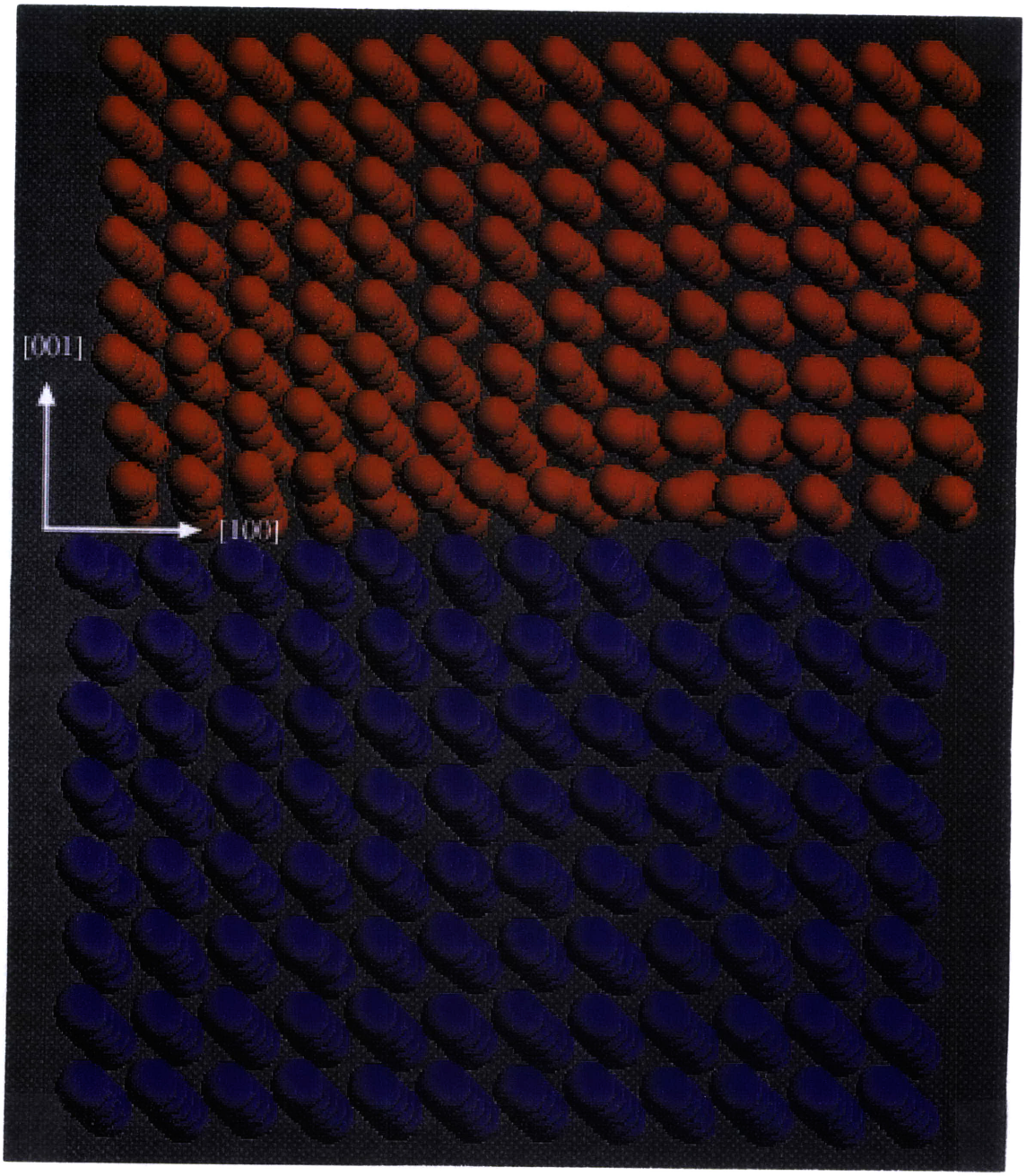

Figure 3-12: Ar-Xe system after 1.06 Å of sliding. Sliding is in the [100] direction.

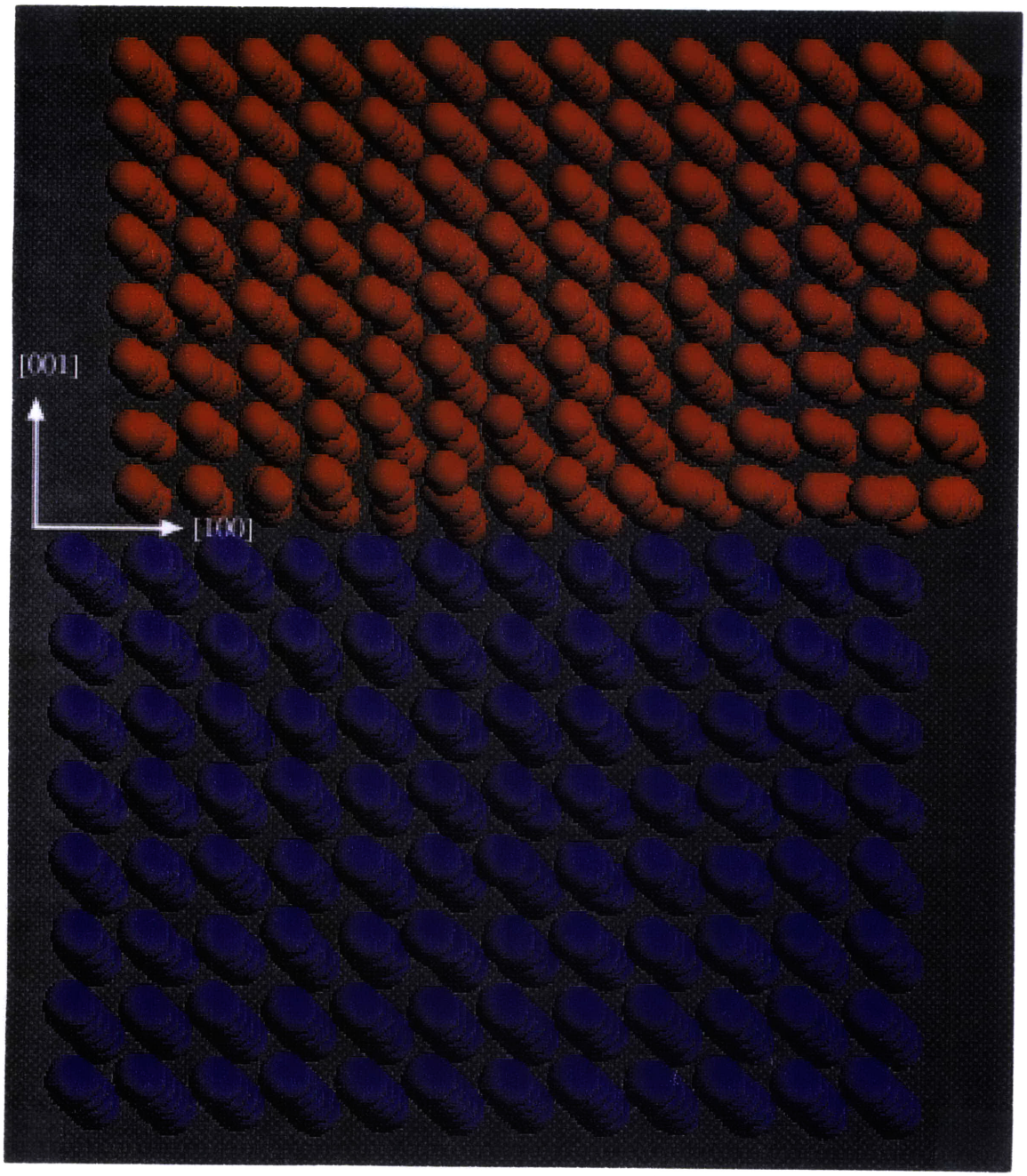

Figure 3-13: Ar-Xe system after 2.12 Å of sliding.

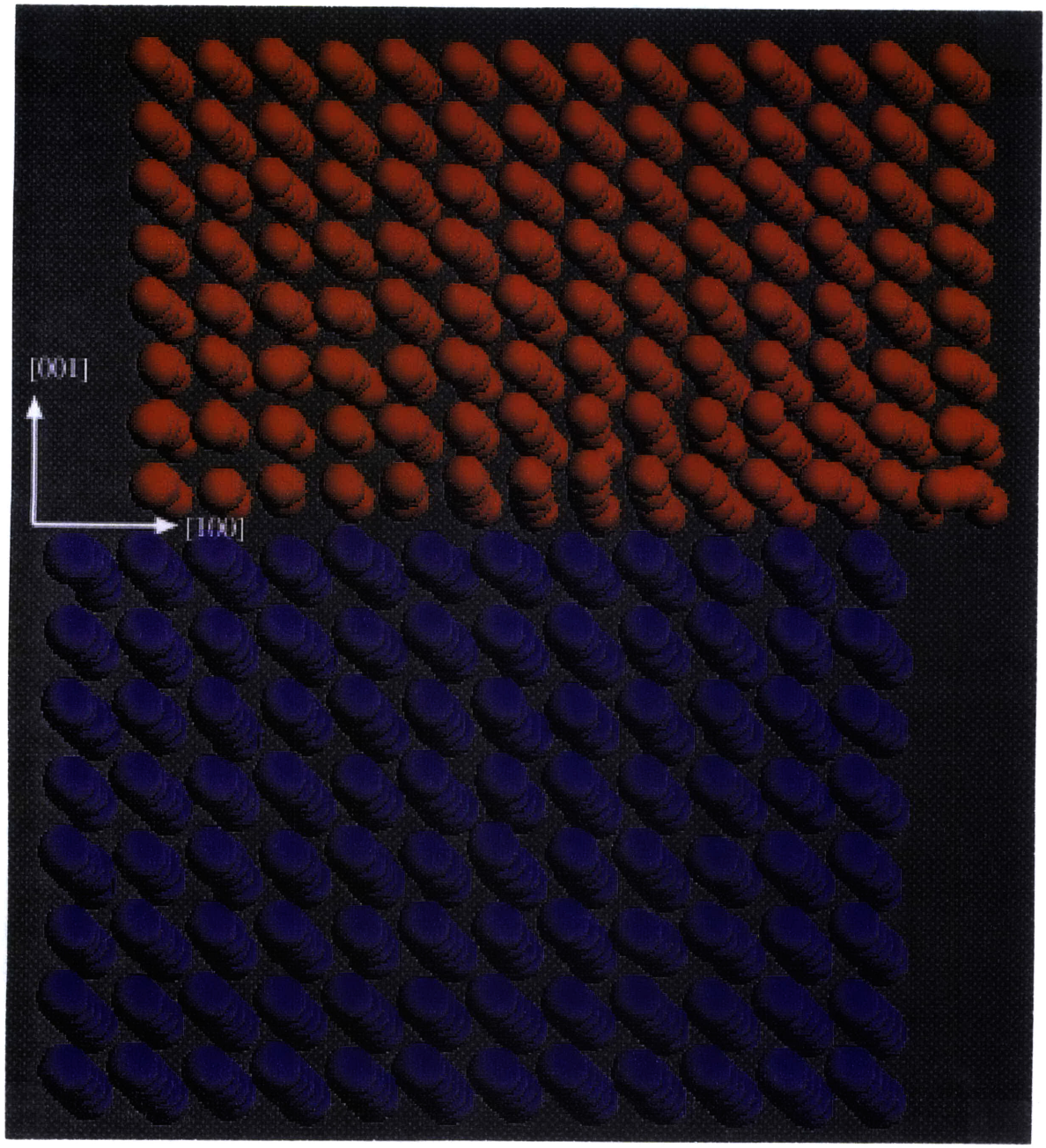

Figure 3-14: Ar-Xe system after 3.18 Å of sliding.

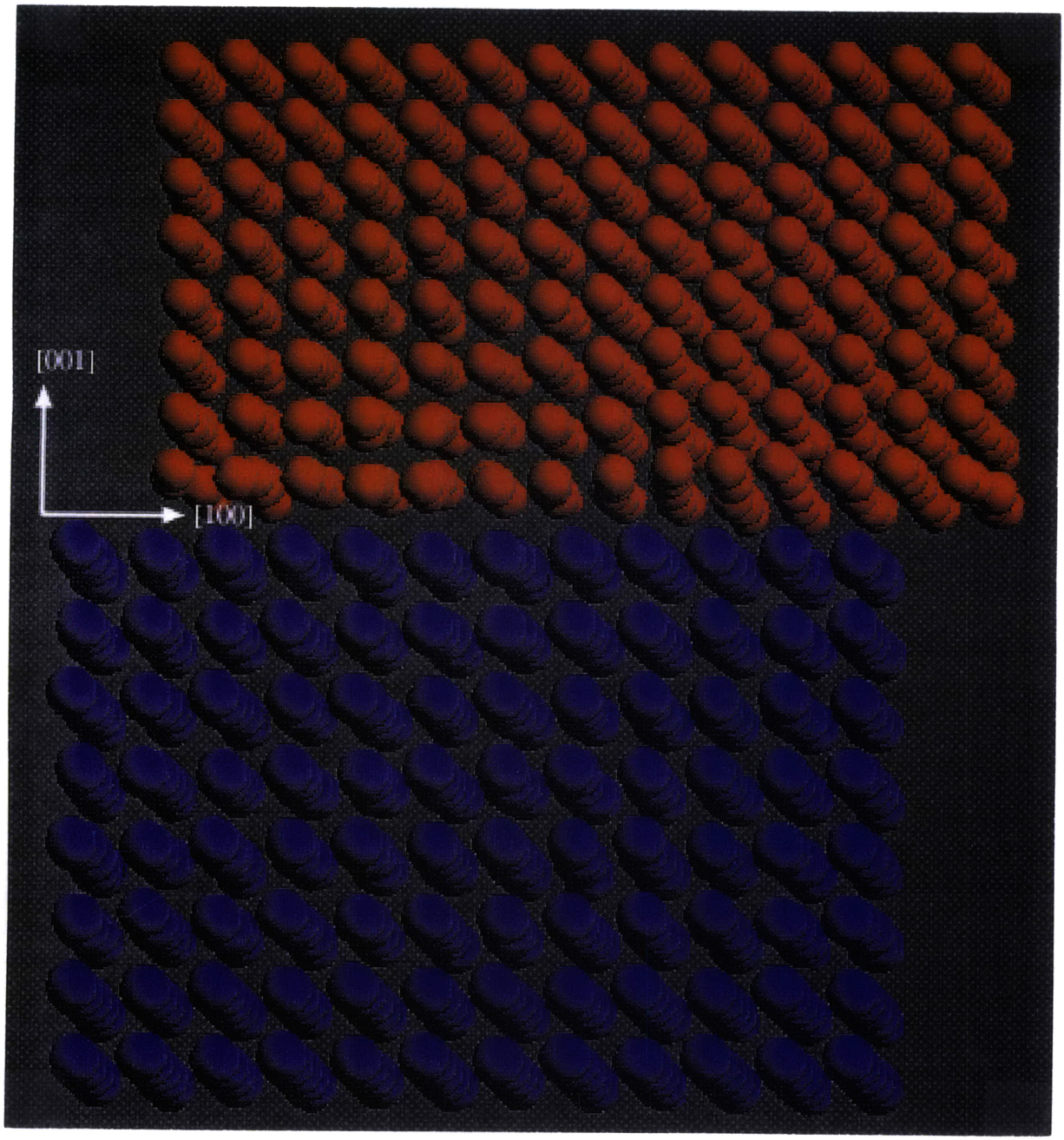

Figure 3-15: Ar-Xe system after 4.24 Å of sliding.

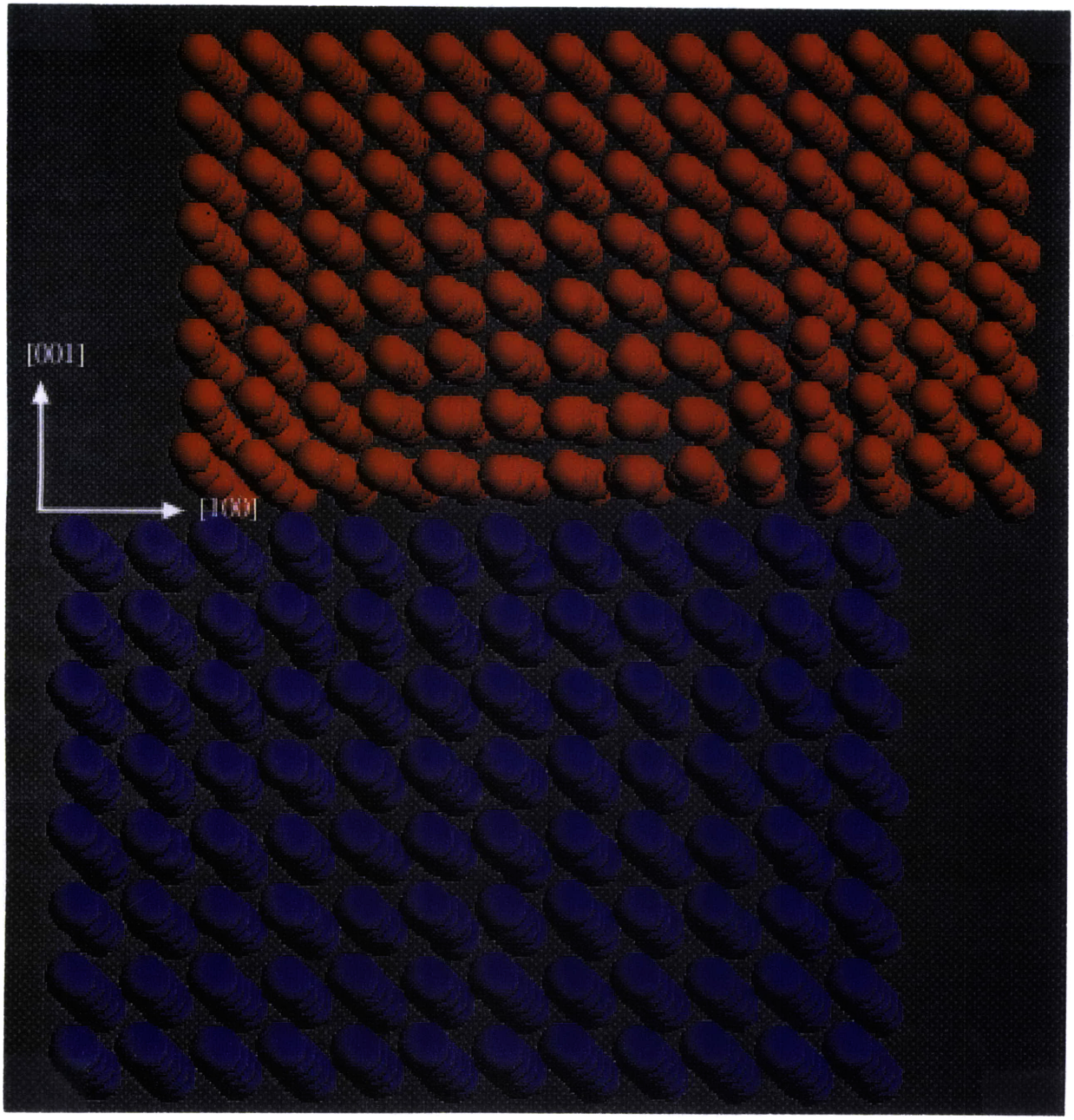

Figure 3-16: Ar-Xe system after 5.30 Å of sliding.

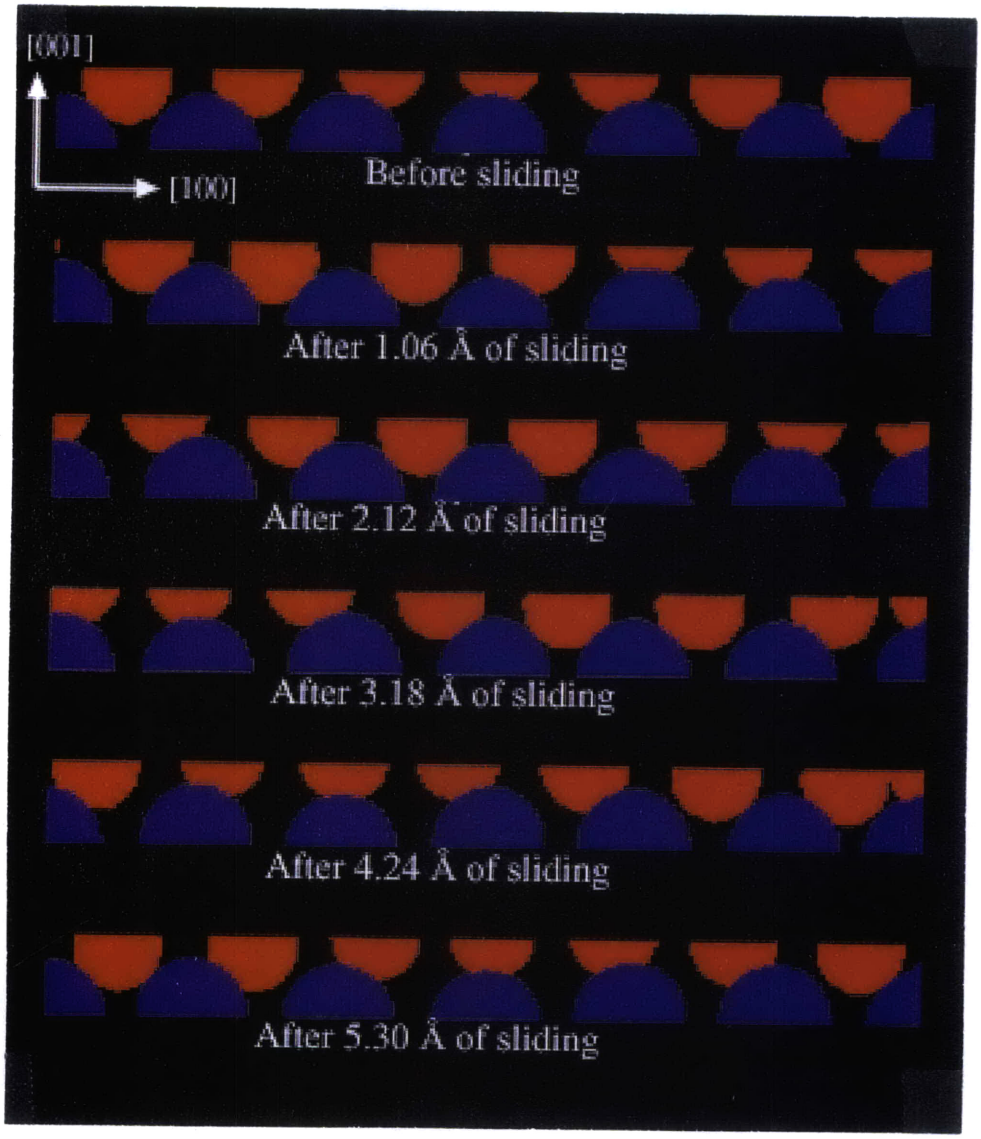

Figure 3-17: Potential energy surfaces of Ar-Xe interface during sliding.

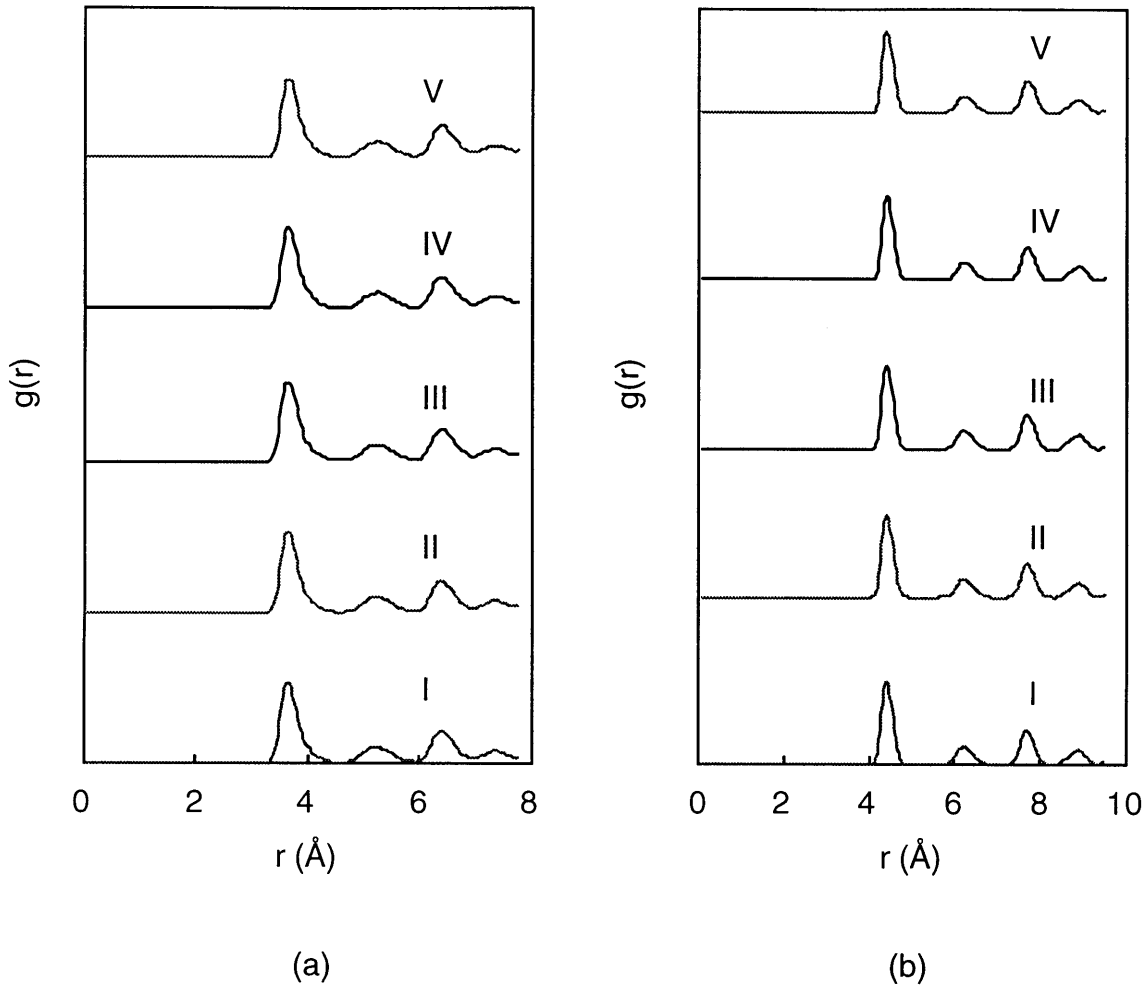

Figure 3-18: Radial distribution function of Ar-Xe interface during sliding. I) After 1.06 $\mathring{A}$ of sliding. II) After 2.12 $\mathring{A}$ of sliding. III) After 3.18 $\mathring{A}$ of sliding. IV) After 4.24 $\mathring{A}$ of sliding. V) After 5.30 $\mathring{A}$ of sliding.

The energy needed to distort the interfacial region of argon comes from the work required to cause sliding. The calculated friction force could be partly due to the forces at the interface that are necessary to deform the argon interface.

Figure 3-18 shows the radial distribution function for the interfacial layers at various points during the sliding. There is hardly any change in the structural order at the interface during the sliding motion. The interface layer static structure factor, not shown here, also is not affected by sliding. At first, this result may seem to contradict the deformation of the argon atoms seen in Figures 3-12 through 3-16. However, the radial distribution function and the structure factor presented here

represent the average over all atoms in the layer as well as over time. Therefore, even though there are local regions of disorder, on the average there is no permanent disorder as a result of sliding.

Chapter 4

Potential Functions of the Silicon-Dodecane System

Prior to simulating the boundary lubrication system, simulations of the individual materials silicon (Si) and dodecane ($C_{12}H_{26}$) were performed. These were done to evaluate the suitability of the potential functions that are used to model the materials. Using the potential functions presented in section 2.1, these materials were simulated to obtain certain preliminary results, and to ascertain the strengths and weaknesses of these models. This chapter also contains the description of the approach employed to model the silicon-dodecane cross-interaction.

4.1 Simulation of Silicon

Several potential functions for silicon have been presented since the pioneering work of Stillinger and Weber [29]. A comparison of six of these models, the Stillinger-Weber (SW) included, was done by Belamane, et al. [45]. They computed the structural and physical properties of clusters, bulk phases, and surfaces, and compared the results with experimental data. They reported that each potential possesses strengths as well as weaknesses, and that there is no one potential that satisfactorily models all the characteristics of Si. Among their conclusions was that the SW is among the best at predicting the elastic constants of silicon, and that it is very effective in large-scale

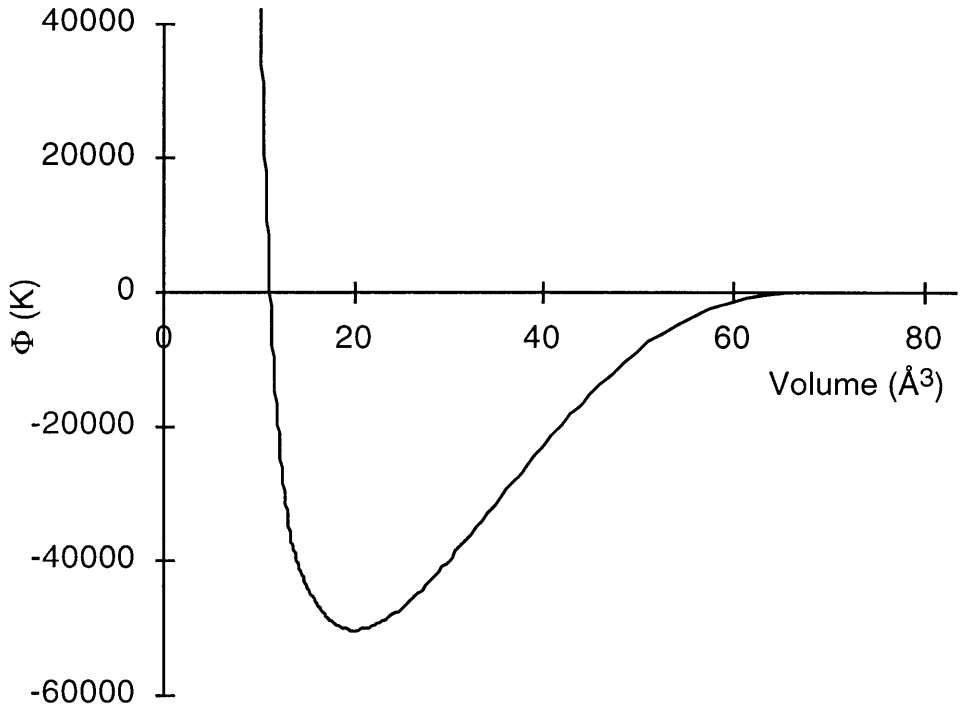

Figure 4-1: SW potential energy. $N = 216$ atoms.

simulations involving the (100) surface. Since the present work required a reliable model of the silicon surface, as well as its elastic behavior, the SW was chosen to model the silicon substrates. Figure 4-1 shows the potential energy of the SW silicon in its crystalline form as a function of the system volume normalized by the number of atoms. A similar plot was shown by Stillinger-Weber in their original work, the only difference being that they used the density rather than the specific volume for the abscissa. They illustrated that among the BCC, FCC, simple cubic, and diamond cubic structures, the minimum energy configuration of their potential is the diamond cubic for a wide range of densities. Thus, the SW is most stable in the diamond cubic, as confirmed by experimental fact.

Table 4.1: Parameters for the simulation of bulk Si.

Number of atoms	216
Cell dimensions	$(16 \times 16 \times 16)$Å
Density	$2,465$ kg/m^3
Time increment	0.384×10^{-15} s

Simulation of the melting of silicon

In order to investigate the melting behavior of bulk silicon, two simulations at different temperatures were done for a system described in Table 4.1. Periodic boundary conditions were applied in all directions and the cell dimensions were kept constant throughout. The temperature was kept fixed at 1,760 K for the first run and 2,767 K for the second. The simulations were each carried out for 5,000 time steps. Figure 4-2 shows the radial distribution function for the two runs, from which the structural order can be easily determined. At 1,760 K, the $g(r)$ has distinguishable peaks at the first, second, and even third nearest neighbor positions, indicating that the system is in its solid phase. At 2,767 K, the first peak has lost its intensity, and the second and third peaks are no longer present. The long range order characteristic of crystals has disappeared, which means that the system has melted. At this temperature, the crystal structure could not be sustained, and the system consequently transformed into the liquid phase. The plots in Figure 4-2 are identical to the plots reported by Stillinger and Weber, who also investigated the melting of bulk silicon and concluded that the SW crystal is stable only up to 2,590 K. This value is higher than the experimental melting temperature of 1,686 K because the simulation reflects mechanical melting while the experimental value reflects thermodynamic melting. Mechanical melting is a homogeneous collapse of the crystal whereas thermodynamic melting is a heterogeneous process which nucleates at defects or surfaces. Phillpot, et al. [46] simulated for silicon surfaces using SW and found the thermodynamic melting point to be 1,691 K, in good agreement with experiment. In the simulation of boundary

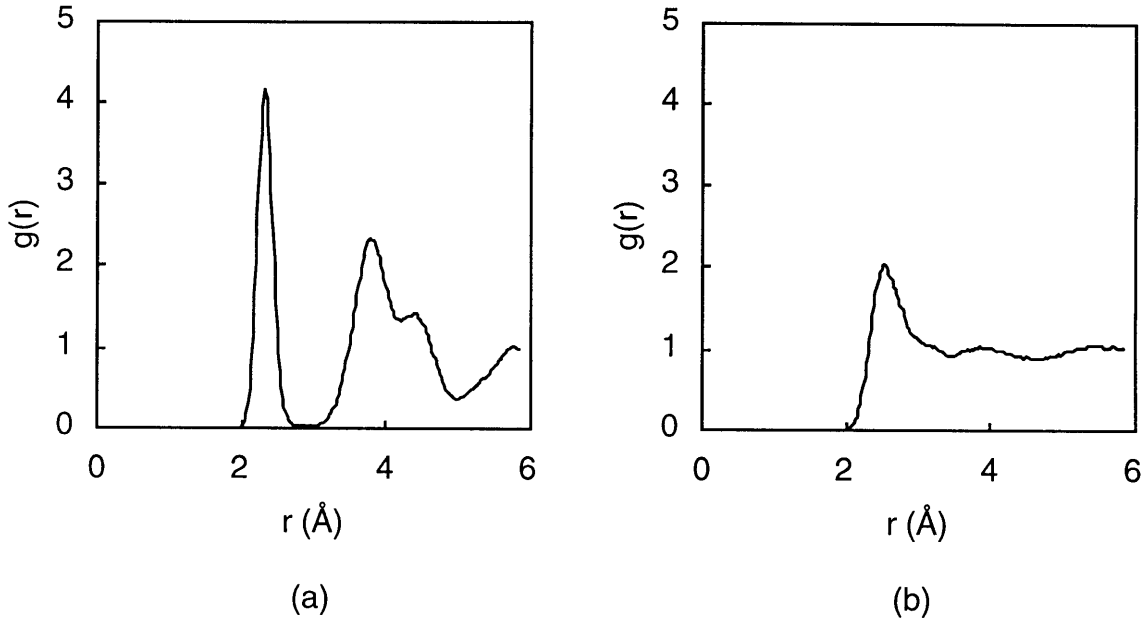

Figure 4-2: Radial distribution function of solid and liquid Si. (a) solid at 1760 K. (b) liquid at 2,767 K

lubrication using silicon surfaces, it will be important to keep the temperature far below 1,691 K.

Calculation of the elastic properties of silicon

Several workers have used the SW to calculate the elastic constants C_{11}, C_{12}, and C_{44} at various conditions using such techniques as the stress fluctuation approach [47] and the homogeneous deformation method [45]. In this work, the elastic constants for the SW potential were calculated using a numerical stress-strain experiment, where a silicon crystal initially in some reference state was prescribed a strain which developed internal stresses in the system. The system parameters were the same as those of the melting simulations (Table 4.1), with the exception of the cell dimensions (and density), which were adjusted to produce zero residual stresses in the reference state. Periodic boundary conditions were still applied in all directions and the temperature was also kept constant. Simulations were done at two temperatures, 888 K and

Table 4.2: Calculated average density of silicon. Simulations conducted at zero pressure.

Temp (K)	ρ (kg/m^3)
888	2,310
1,477	2,300

1477 K, in order to observe the effect of temperature on the calculated elastic moduli.

The first step was to define the reference state which meant that the initial positions and velocities of the atoms as well as the initial dimensions of the simulation cell had to be determined. As usual, the velocities were assigned randomly and adjusted to zero net momentum of the system and scaled to the desired temperature. The atoms were positioned in the diamond cubic lattice, and the simulation cell was made cubic with some reference volume V_{ref}. The choice of V_{ref} was important, for stresses calculated in this manner are highly sensitive to the reference cell dimensions. In this work, V_{ref} was chosen to make the initial stresses zero, so that the effect of residual stresses on the calculations could be eliminated. It may be noted that the experimental values of the density are not appropriate to use since the laboratory state of equilibrium may not be the same as the simulation state. Furthermore, the experimental values of density do not guarantee zero residual stress in the system. Therefore, the reference cell dimensions were obtained from a simulation run of the described system at the given temperature and zero pressure where the cell size and shape were allowed to fluctuate using the Parrinello-Rahman method (see section 2.2) for 5,000 steps. The $\mathbf{H}$ matrix was averaged over the entire run and the resulting $\mathbf{H}_{avg}$ provided the desired reference volume, $V_{ref} = \det[\mathbf{H}_{avg}]$. Table 4.2 lists the densities that were obtained from this exercise.

Once the reference cell was defined, the first numerical experiment was to introduce a uniaxial strain, $\epsilon_{xx} = 0.002$, by uniformly elongating the reference cell only in the x-direction by a factor of 1.002, and then simulating for 2,000 time steps with the cell fixed in its stretched form. A strain of 0.002 produced stresses no higher than

Table 4.3: Calculated stresses in silicon due to uniaxial strain.

	T = 888 K	T = 1477 K
$\epsilon_{xx} = 0.002$	$\sigma_{xx} = 280$ MPa	$\sigma_{xx} = 236$ MPa
	$\sigma_{yy} = 143$	$\sigma_{yy} = 123$
	$\sigma_{zz} = 138$	$\sigma_{zz} = 116$
$\epsilon_{xx} = -0.002$	$\sigma_{xx} = -303$	$\sigma_{xx} = -312$
	$\sigma_{yy} = -170$	$\sigma_{yy} = -174$
	$\sigma_{zz} = -168$	$\sigma_{zz} = -145$

Table 4.4: Calculated stresses in silicon due to simple shear.

	T = 888 K	T = 1477 K
$\epsilon_{xy} = 0.002$	$\sigma_{xy} = 200$ MPa	$\sigma_{xy} = 183$ MPa
$\epsilon_{xy} = -0.002$	$\sigma_{xy} = -200$	$\sigma_{xy} = -143$

312 MPa, which is well under the yield point $\sigma_y \approx 3,000$ MPa for silicon, so it was safe to use this data to compute the elastic constants. The resulting internal stresses, calculated using Equation 2.20, were averaged over the entire run, and this process was repeated for $\epsilon_{xx} = -0.002$ in order to improve the statistics. The axial stress σ_{xx} and the transverse stresses σ_{yy}, σ_{zz} averaged over the run are shown in Table 4.3 for the two temperatures.

Next, a simple shear was imposed on the reference cell, much in the same way as the uniaxial strain experiment, only that the reference cell was deformed as to produce only a shear strain $\epsilon_{xy} = 0.002$. The cell was then held fixed and the stresses were computed and averaged for 2,000 time steps. The resulting shear stresses σ_{xy} are shown in Table 4.4.

All the computed stresses were then used to calculate the elastic moduli, given in

Table 4.5: Calculated elastic constants of silicon. The results under the column heading "Stress-Strain" are from the present work. Experimental values are from reference [48].

Modulus	Stress-Strain	Kluge, et al.	Experimental
	$T = 888K$		
C_{11}	145.8 GPa	141.4 GPa	157.5 GPa
C_{12}	77.4	75.2	60.5
C_{44}	50.0	52.4	75.3
	$T = 1477K$		
C_{11}	137.0 GPa	133.2 GPa	148.0 GPa
C_{12}	70.0	73.9	57.5
C_{44}	40.8	42.0	70.0

Table 4.5. The expressions used in the modulus calculations are,

$$C_{11} = \frac{\sigma_{xx}}{\epsilon_{xx}} \tag{4.1}$$

$$C_{12} = \frac{\sigma_{yy}}{\epsilon_{xx}} \tag{4.2}$$

$$C_{44} = \frac{\sigma_{xy}}{2\epsilon_{xy}}. \tag{4.3}$$

In Equation 4.2, the transverse stress in the z-direction σ_{zz} can just as well be used instead of σ_{yy} due to the cubic symmetry of Si. The values of C_{12}, given in Table 4.5, are the average of using σ_{yy} and σ_{zz} in Equation 4.2. In addition, all the moduli in the table are the result of averaging the outcomes of the positive and negative prescribed strains. The table also lists similar data obtained by Kluge, et al. [47] as well as experimental data. The values of the elastic constants from this work agree well with the results of Kluge, et al., even though they used the fluctuation approach, which is more rigorous than the simple stress-strain experiment. The results also compare fairly well to the experimental data with the exception of C_{44} for which the computational values are significantly lower than the experimental data. This is a

Table 4.6: Parameters for the simulation of dodecane using UAM potential.

Number of molecules	27
Temperature	298 K
Density	744 kg/m^3
Cell dimensions	$(21.7 \times 21.7 \times 21.7)$Å
Time increment	0.384×10^{-15} sec

well known shortcoming of the SW potential and no attempt was made to remedy it here, except to note that the calculations of the friction forces which will occur in later simulations may be affected by the under-prediction of the shear modulus.

4.2 Simulation of Dodecane

The UAM potential has been used in the past to simulate the viscous behavior of decane ($C_{10}H_{20}$) to good agreement with experimental data by Mundy, et al.[32] and Cui, et al. [49, 50]. To ascertain how well the UAM predicts the viscosity of dodecane, a similar simulation as those by Mundy and Cui has been performed for a bulk system of 27 molecules. The parametric details of this simulation are presented in Table 4.6. The simulation cell was fixed in size and shape throughout the run, and velocity rescaling was applied at every time step to keep the temperature constant.

The system was first brought to equilibrium through a run of 50,000 time steps. Subsequently, a run of 20,000 time steps was made, and the viscosity was calculated at every tenth time step using Equation 2.28. The result, shown in Figure 4-3, shows that the calculated viscosity for this system at the completion of the run is 1363 μPa $\cdot$ s, which is close to the experimental value of $1,407$ μPa $\cdot$ s. It is clear from Figure 4-3 that a run of only 20,000 steps is inadequate to establish convergence. The good accuracy of the calculated viscosity is largely fortuitous, although it does seem likely that the viscosity will converge reasonably close to the experimental value if given enough time. Since the only purpose of this simulation was to demonstrate

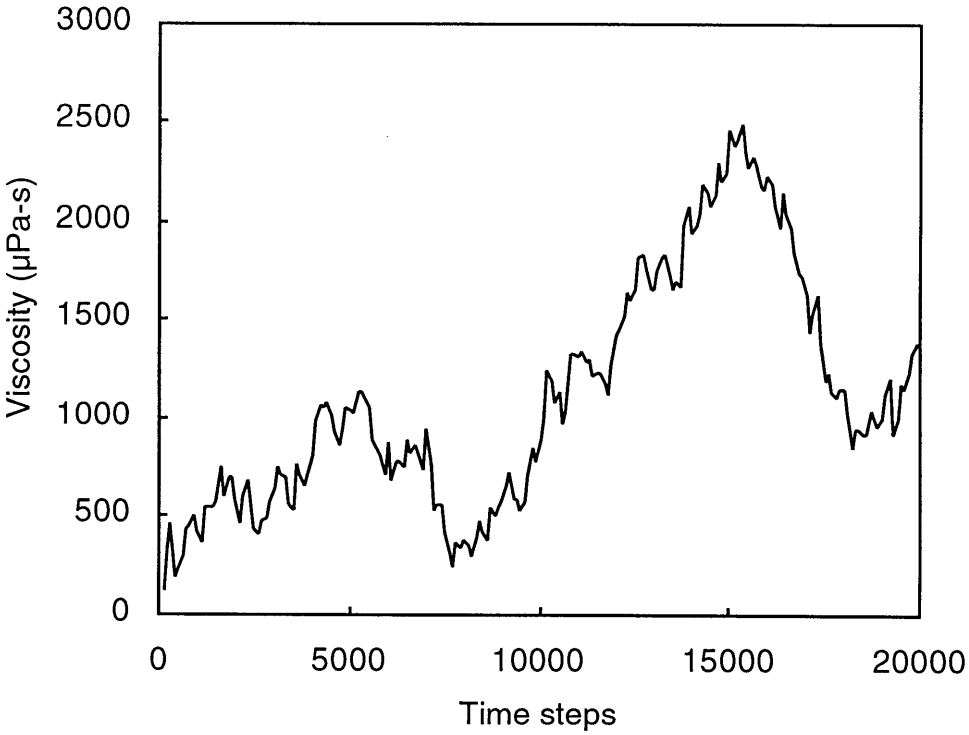

Figure 4-3: Viscosity of bulk dodecane. UAM potential.

the UAM's effectiveness in calculating the viscosity of dodecane, further efforts to improve the viscosity calculations were not pursued. It may be noted that the viscosity calculations are extremely sensitive to the choice of the time origin used in the evaluation of the time correlation. An improper time origin, such as one which is not in an equilibrated state, yields unreliable predictions of the viscosity. For this run the time origin is apparently good, although any thorough study should average over many time origins.

The next step was to use the CFF model (see section 2.1.3) to simulate dodecane. In its original form, the CFF requires a lot of computational time which can be avoided by replacing some of the terms in the model with simpler, less time-consuming substitutes. For this study, the torsional potential (the last term in Equation 2.13) is omitted in favor of the Jorgensen potential (Equation 2.11) from the UAM model. This is a significant saving in computation because the CFF torsional potential involves all dihedral angles formed around a C-C bond, including those involving H atoms, while the Jorgensen potential considers torsional angles involving only C atoms. The justification for this simplification is that the Jorgensen potential is itself a well-founded and verified potential function based on experimental data. Moreover, for this study, the vibrational spectra from the torsional rotations are not as important as the vibrations from C-H stretching, H-C-H angle bending, C-C bond stretching, and C-C-C angle bending motions.

Using the modified CFF potential, a system of 27 dodecane molecules was simulated in order to compute the vibrational frequencies of dodecane. The simulation parameters were the same as those of the previous UAM simulation, given in Table 4.6. The simulation cell was fixed in size and shape, and the temperature was rescaled at every time step. The system was first given 500,000 time steps to equilibrate. Afterwards, a simulation of 200,000 time steps was conducted, during which the velocity autocorrelation function was computed for each of the involved species (C, H) at every tenth time step. Ten different time origins were used in the calculation of the velocity autocorrelation in order to improve the results. The average of the ten autocorrelations was then transformed into the frequency space by the Maximum

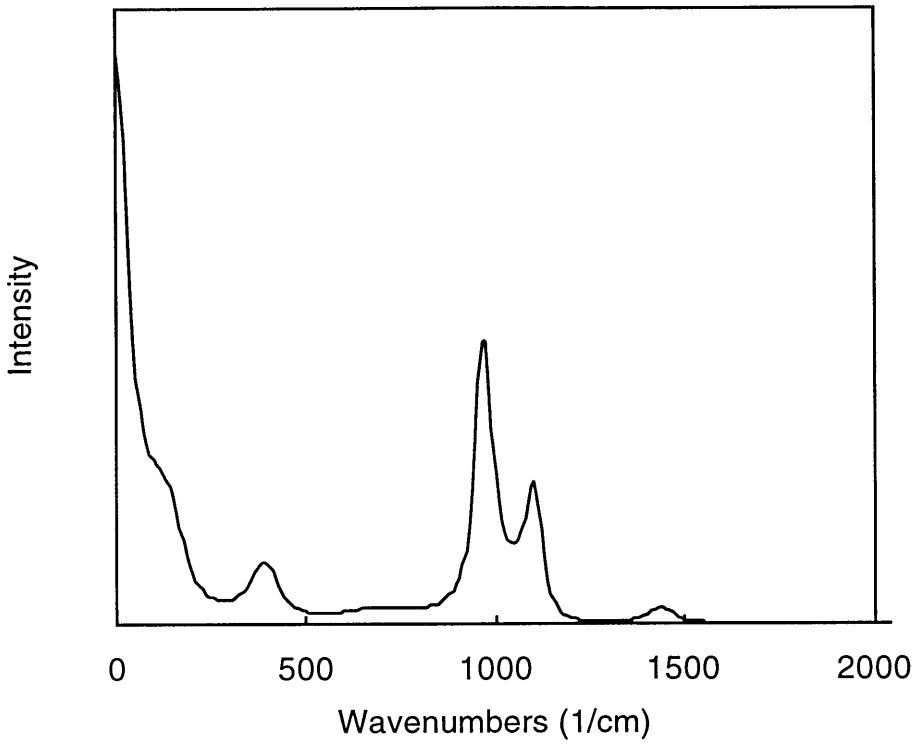

Figure 4-4: Vibrational spectrum of carbon atoms in bulk dodecane. Modified CFF potential. The abscissa is the inverse of the wavelength of light corresponding to the frequency of vibration.

Entropy Method using 40 poles (see section 2.4).

Figures 4-4 and 4-5 show the vibrational spectra for the carbon and hydrogen atoms, respectively. The peaks in the signals each correspond to certain vibrational modes of the molecule, which are well known experimentally. In Table 4.7, the calculated peaks are assigned the proper vibrational modes and compared with experimental data. The CFF predicts the vibrational spectra very well because it was originally fitted to vibrational properties of alkanes. It is apparent that the substitution of the torsional potentials has no noticeable effect on the high frequency vibrations. At lower frequencies, where the torsional rotations occur, there may be some discrepancies. Since this study is concerned with only the high frequency modes listed in Table 4.7, the current modified CFF model using the Jorgensen potential seems satisfactory.

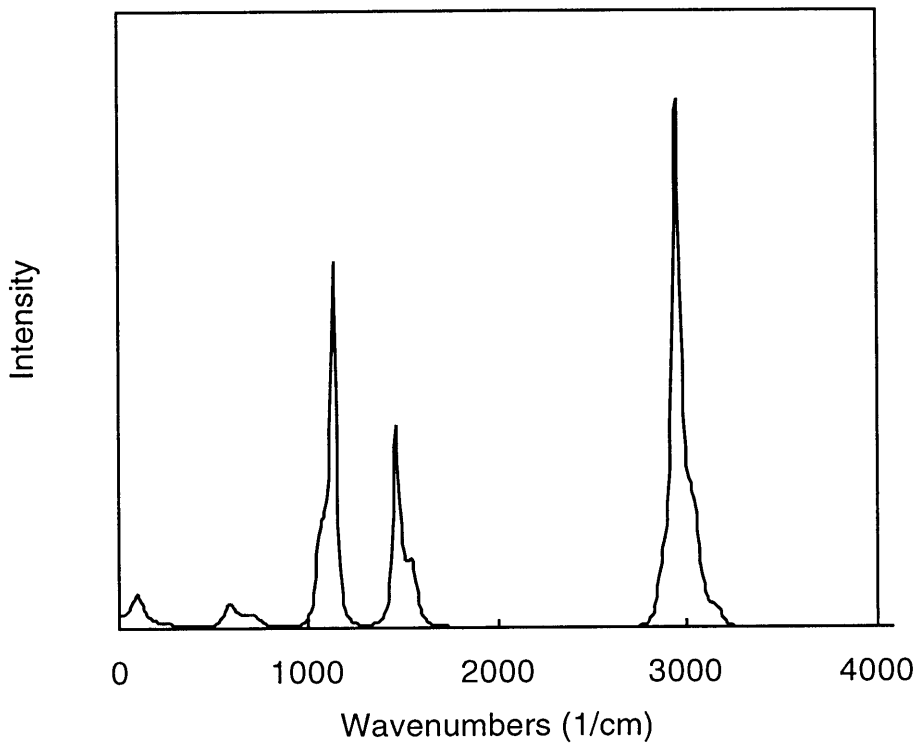

Figure 4-5: Vibrational spectrum of hydrogen atoms in bulk dodecane. Modified CFF potential.

Table 4.7: Band assignment of the vibrational frequencies in dodecane.

Mode	Predicted wavenumber (1/cm)	Experimental wavenumber
C-C stretch	955	$1060 \sim 1130$
C-C-H bend	1138	-
H-C-H bend	1467	1450
C-H stretch	2952	$2800 \sim 3000$

4.3 Silicon-Hydrocarbon Interaction Potential

For two dissimilar materials A and B whose potential functions are each of the Lennard-Jones form, the cross-interaction potential function between A and B may be taken as a Lennard-Jones potential, where the L-J parameters are the mean of the contributing members A and B,

$$\begin{aligned} \sigma_{AB} &= \frac{1}{2}(\sigma_A + \sigma_B) \\ \varepsilon_{AB} &= \sqrt{\varepsilon_A \varepsilon_B}. \end{aligned} \tag{4.4}$$

For this method to work, the potentials of A and B (and consequently the combined potential AB) must both be in the same L-J form (i.e., 12-6, 9-6). This procedure, simplistic as it may seem, has been verified with experimental data and is widely used to simulate bimaterial systems of two L-J materials. For instance, both the UAM and CFF potentials for hydrocarbons utilize this method in their intermolecular potential models.

For the present bimaterial system consisting of silicon and hydrocarbon, however, it is necessary to create one potential for Si-C and another for Si-H interactions. We have already adopted the SW potential to model silicon, and the hydrogen and carbon are 9-6 L-J potentials as given by the CFF model. The difficulty in combining these potentials is that the SW is a three-body, non-L-J potential. Therefore, the arithmetic/geometric mean technique cannot be applied here directly. There exists no standard procedure for combining three- and two-body potentials, so the best alternative is to generate a 9-6 L-J representation for the SW, and then to employ the L-J combining rules. In order to come up with an L-J representation, it was necessary to first reduce the SW to an effective pair potential which is a function only of the separation distance between pairs of atoms in the system. This was done by first plotting the potential energy of the SW system as a function of the cubic cell volume normalized by the number of atoms in the system, which is shown in Figure 4-1, then taking the cube-root of the horizontal axis (specific volume). The resulting plot is the solid curve in Figure 4-6, to be called the effective SW pair potential and

denoted $\phi_{eff,SW}$ from here on. By taking the cube-root of the normalized volume, the horizontal axis becomes the length of a side of an atom-cube, imagining that the system can be divided into N number of such atom-cubes, each of which contains one atom in its center. The effective SW is a first-order approximation of the potential energy of the system as a function of the separation between pairs of atoms. This mapping of the three-body SW potential to a two-body form inevitably results in much information being lost. At the same time, the effective SW still retains many important features of the original SW such as the well depth and the atomic diameter. Essentially, the effective SW is analogous to taking a two-dimensional picture of a three-dimensional object.

The next task was to fit a L-J potential through the effective SW curve. The general form for the 9-6 L-J potential is

$$\phi_{L-J\ 9-6}(r) = \varepsilon \left[A \left(\frac{\sigma}{r} \right)^9 - B \left(\frac{\sigma}{r} \right)^6 \right], \tag{4.5}$$

where A and B are constants. Setting $\varepsilon = 50,300\ K$, left three fitting parameters: A, B, and σ. Several combinations of these parameters have been tested and the best fit was determined by inspection as to which set of parameters most closely captured the essential features of the effective SW pair potential. The aspects of $\phi_{eff,SW}$ considered to be most important were: the value of r at which $\phi_{eff,SW} = 0$, the value of r at which $\phi_{eff,SW}$ is a minimum, the value of $\phi_{eff,sw}$ at its minimum, and the shape of the curve near the zero-slope region. These were, to a large degree, competing criteria, so they could not all be met simultaneously. A satisfactory compromise among these criteria was reached with $A = 1.015$, $B = 1.910$, and $\sigma = 2.8$ Å. The resulting L-J potential for the SW, from here on called $\phi_{LJ,SW}$, is the dotted curve in Figure 4-6. The fit is by no means exact, and the most error-prone region is in the attractive portion of the potential. This discrepancy comes from the abrupt manner in which the SW curve approaches zero in the attractive part. In L-J forms, the attractive part tends to zero asymptotically.

It may be noted that a 12-6 Lennard-Jones form for silicon was suggested in 1961

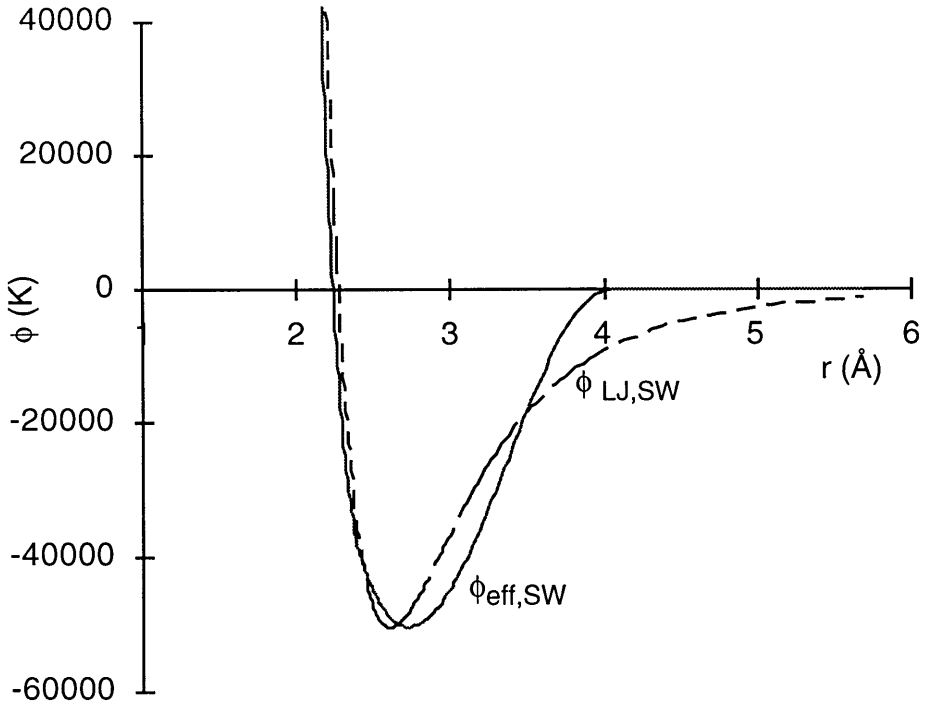

Figure 4-6: L-J 9-6 representation of the SW potential function.

Table 4.8: L-J parameters for Si-C and Si-H interaction potential.

$\varepsilon_{\text{Si-C}}$	=	2,163.0 K	$\sigma_{\text{Si-C}}$	=	3.174 Å
$\varepsilon_{\text{Si-H}}$	=	255.7 K	$\sigma_{\text{Si-H}}$	=	3.208 Å

by Svehla who used experimental data of the molar volume at the melting point as well as the boiling temperature to obtain $\sigma = 2.91$ Å and $\varepsilon/k_B = 3,036$ K, respectively [51]. His potential is not suitable for the present work because the well depth of 3,036 K used in his L-J 12-6 is too low compared with the well depth 25,150 K given by the SW potential, which has already been chosen to model silicon in this work. It is thus unrealistic to treat Si-Si interactions using SW, then treat Si-hydrocarbon interactions using Svehla's model which is nearly an order of magnitude lower in its definition of the binding energy. Thus, it was preferred to construct a Lennard-Jones form which is more comparable to the SW.

Combining $\phi_{LJ,SW}$ with ϕ_{nb} from Equation 2.15 for hydrogen and carbon produces the cross-interaction potential,

$$\phi_{Si-H,C}(r) = \varepsilon \left[0.7124 \left(\frac{\sigma}{r}\right)^9 - 1.1969 \left(\frac{\sigma}{r}\right)^6 \right], \tag{4.6}$$

where the values for σ and ε, found using Equation 4.4, are given in Table 4.8. The functions are graphed in Figure 4-7.

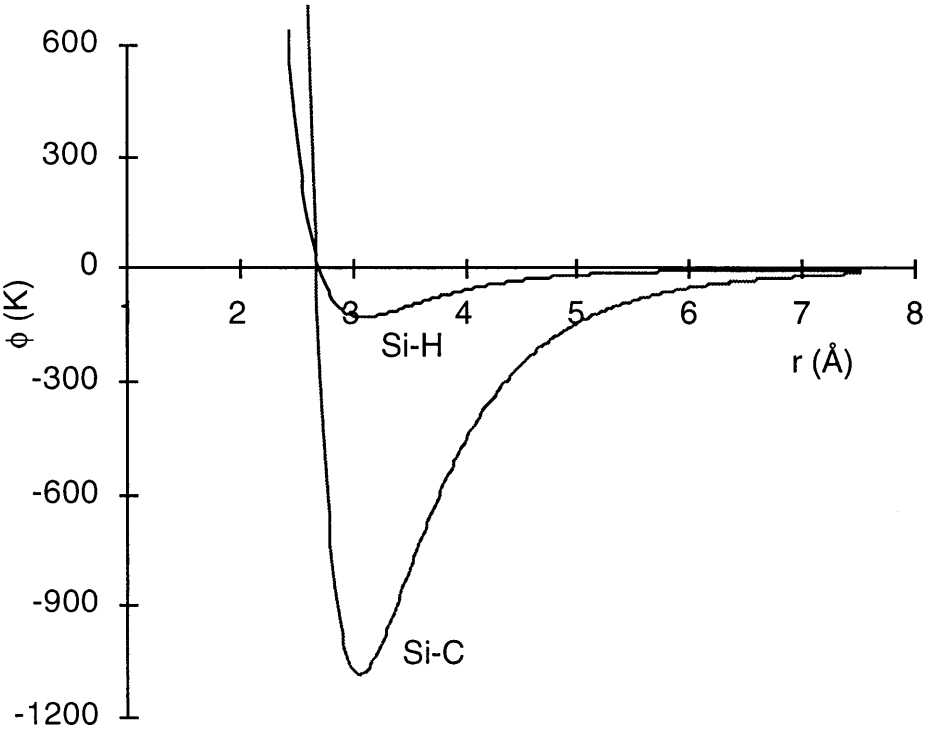

Figure 4-7: Si-C and Si-H interaction potentials.

Chapter 5

Simulation of Boundary Lubrication

The bimaterial system, silicon and dodecane ($C_{12}H_{26}$), in boundary-lubricated sliding is schematically shown in Figure 5-1. The potential functions for all the atomic interactions are described in Chapter 4. The stress tensor calculations of Equation 2.20 require that each cell contain homogeneous material. Thus, the system was divided into three simulation cells, one for each silicon substrate and one for the dodecane lubricant.

The two silicon cells were subjected to semi-infinite boundary conditions while the dodecane was modeled with thin-film boundary conditions (see section 2.2), so that all cells were periodic in the x and y directions. Due to the periodic boundary conditions, the following conditions on the simulation cells were maintained at all times:

$$\begin{aligned} \mathbf{a}_{\text{Si-top}} &= \mathbf{a}_{\text{Si-bottom}} = \mathbf{a}_{\text{dodecane}} \\ \mathbf{b}_{\text{Si-top}} &= \mathbf{b}_{\text{Si-bottom}} = \mathbf{b}_{\text{dodecane}}, \end{aligned} \tag{5.1}$$

where $\mathbf{a}$ and $\mathbf{b}$, defined in section 2.3, are the vectors that define the $x-y$ planes of the simulation cells with respect to some reference frame. The normal strain in the z direction, ϵ_{zz}, was controlled to give the system the desired normal stress, σ_{zz}. The Parrinello-Rahman method was used in limited fashion such that only the Poisson

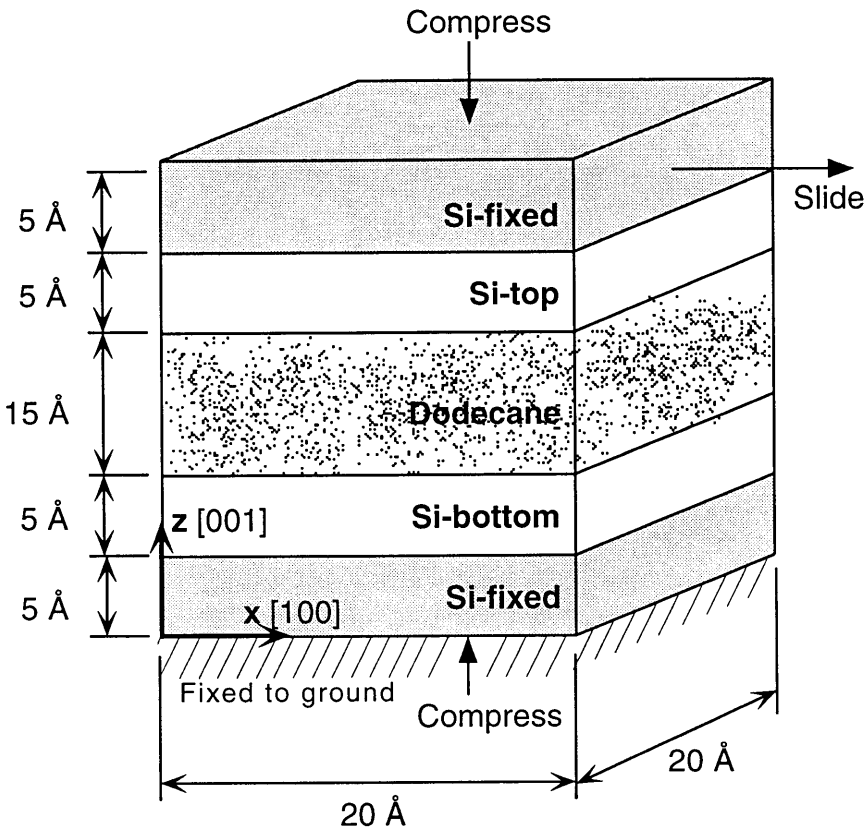

Figure 5-1: Schematic of simulation cell for the silicon-dodecane system.

Table 5.1: Parameters for the simulation of one dodecane molecule.

Number of $C_{12}H_{26}$ molecules	1
Total number of Si atoms: bottom	128
Number of Si layers: bottom	4
Density of Si	$2,434$ kg/m^3
Si surface plane	(001)
Si crystal structure	Diamond cubic
Total number of fixed Si atoms: bottom	128
Number of layers of fixed Si atoms: bottom	4
Temperature	298 K
Time increment	0.384×10^{-15} s
Number of time steps	60,000

strains, ϵ_{xx} and ϵ_{yy}, were allowed in response to σ_{zz}. No shear strains were allowed in order to eliminate unrealistic fluctuations of the cell dimensions.

5.1 Adsorption and Desorption of Dodecane

The first simulation was that of one dodecane molecule on a silicon substrate. The objective was to determine the preferred orientation of a single molecule on the (001) Si surface in the absence of neighboring molecules. Table 5.1 lists the system parameters used in this simulation. The molecule was initially placed above the surface as shown in Figures 5-2 and 5-3. It was tilted at 45_o to the surface normal in order to allow it to naturally settle on the surface to its preferred resting orientation. In addition, the projected image of the molecule on the surface was aligned in the [210] direction so as to avoid a symmetric alignment, such as the [110] or the [100] direction, which could have trapped the molecule in a local potential minimum from the onset of the run. The molecule was then left to interact with the surface for 60,000 time steps, during which it approached and adsorbed onto the surface. The temperature

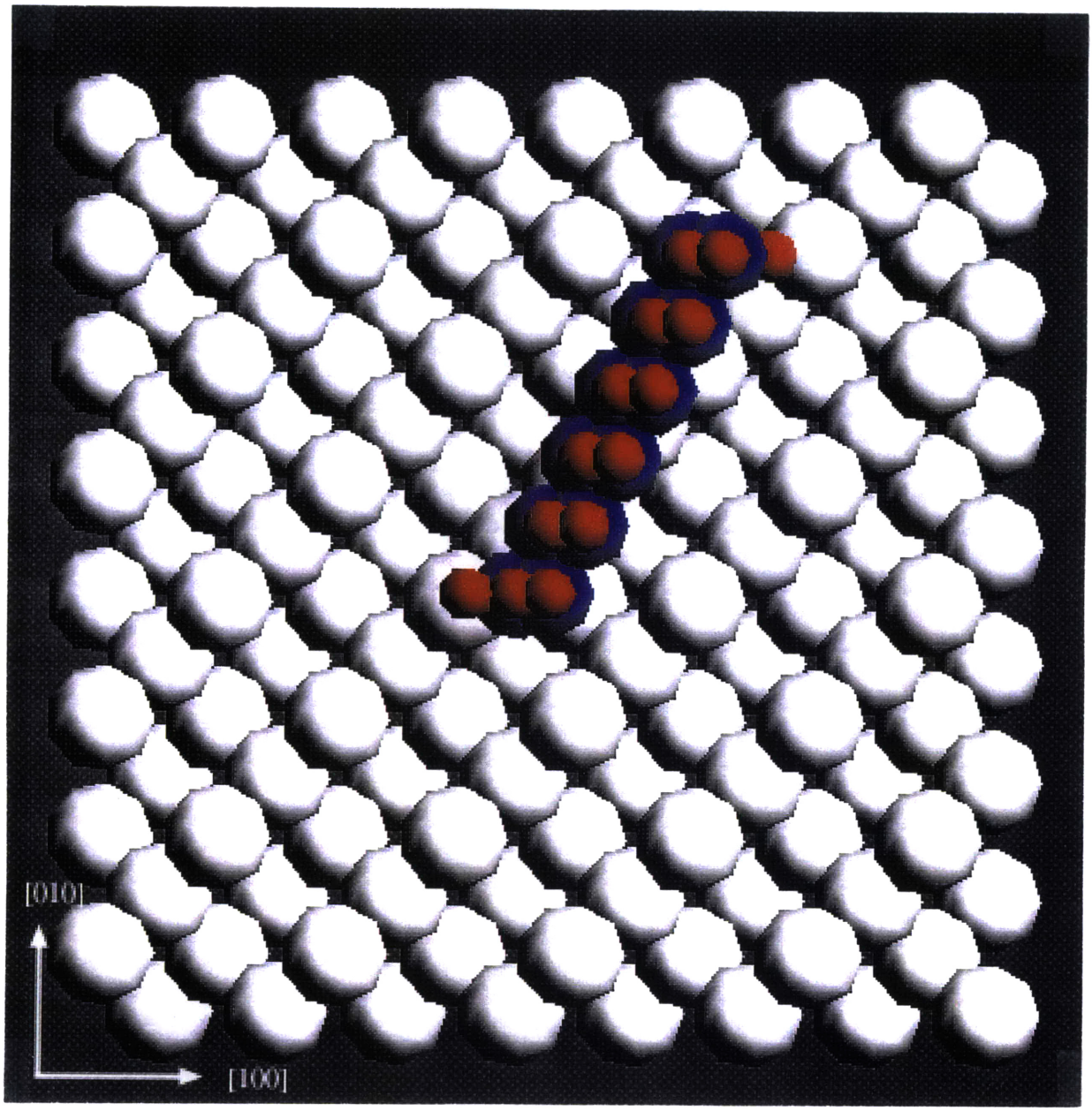

Figure 5-2: Initial position of one dodecane molecule: top view. Carbon atoms are in blue, hydrogen in red, and silicon in white.

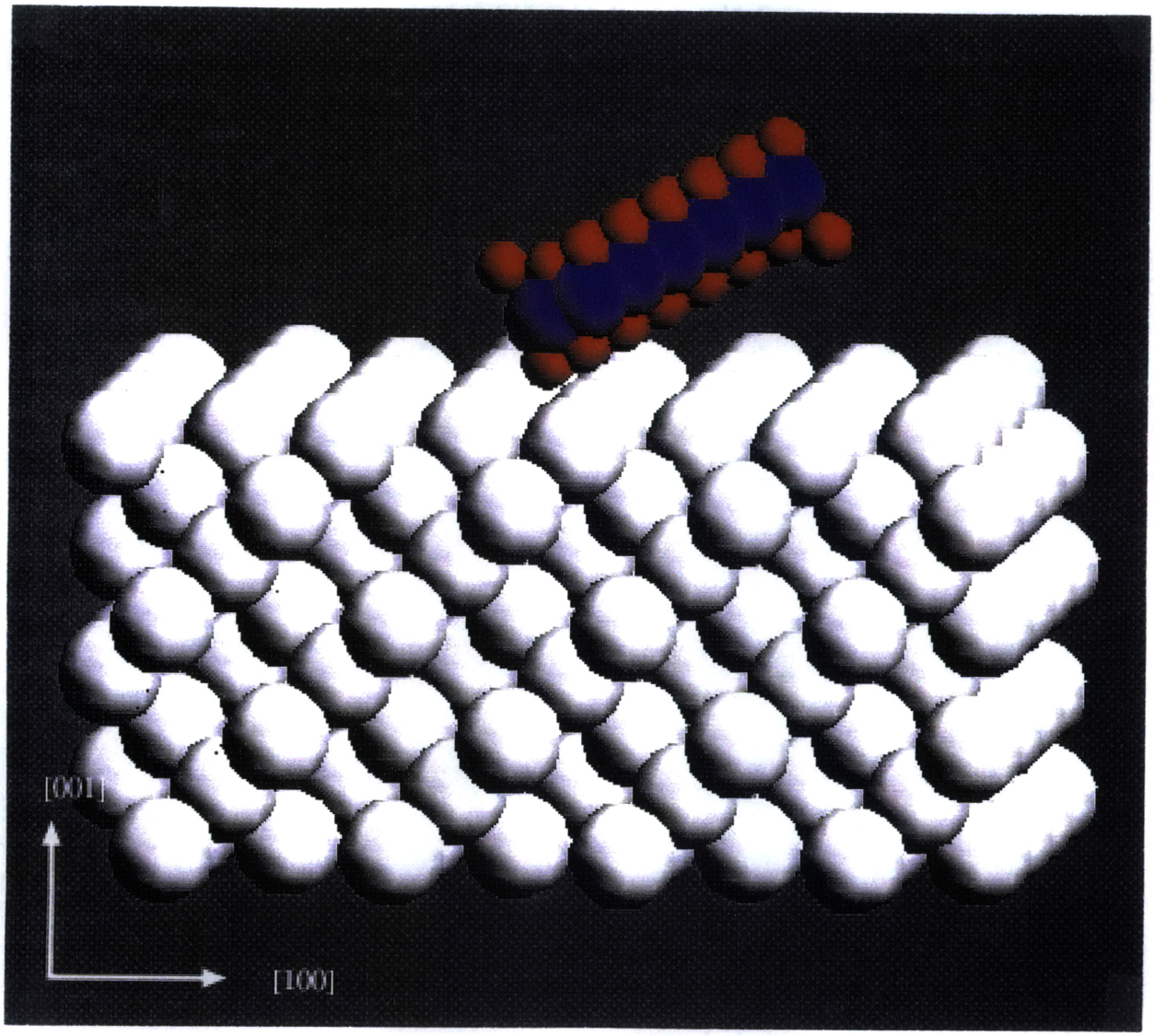

Figure 5-3: Initial position of one dodecane molecule: side view.

was rescaled at every time step to 298 K throughout the process. Figures 5-4 and 5-5 show two views of the molecule's position at the completion of the run. Only the top two atomic layers of the silicon substrate are shown to clearly display the pattern of steps and ledges on the surface. The ledges are trench-like valleys that lie along the [110] direction, separated by rows of silicon atoms which will be referred to as the steps. Due to some disorder at the surface, the ledges fail to extend infinitely, terminating at certain locations where the atoms in the steps are pinched together. It is noted that these ledge patterns are not due to the presence of the molecule, since they occurred even in simulations of the silicon (001) surface alone. These ledge patterns are quite helpful in elucidating the adsorption mechanism of the dodecane molecule on the surface. The top view of the adsorbed molecule in Figure 5-4 is very clear in showing that the molecule settles such that the molecular axis lies along one of the ledges. An interesting phenomenon occurs in the middle of the molecule where the ledge in which the chain is situated is terminated. At this point, rather than continuing to lie along the same direction, the molecule crosses over a step to the next ledge, indicating a very strong preference for ledge adsorption.

Careful inspection also shows that this cross-over takes place directly over a shallow section of the step. The side view in Figure 5-5 shows that the molecule is indeed lying down along the ledges on the surface. Silvestro [52] has used polarized Raman spectroscopy techniques to conclude that the molecules in a film of dodecane adsorbed on a silicon (001) surface at room temperature are primarily aligned in the [110] direction. His result qualitatively agrees with the simulation, since the ledges, in which the simulated molecules are adsorbed, are oriented in the [110] direction. This indicates that the silicon- dodecane cross potential developed in section 4.3 is reasonably valid in modeling the interfacial interactions.

The simulation was next extended to nine dodecane molecules on the silicon surface to model a film of lubricant. The initial configuration was similar to Figures 5-2 and 5-3, the only difference being that there were nine such molecules evenly distributed above the surface. The simulation parameters are identical to those in Table 5.1, except for the number of dodecane molecules as well as the number of time

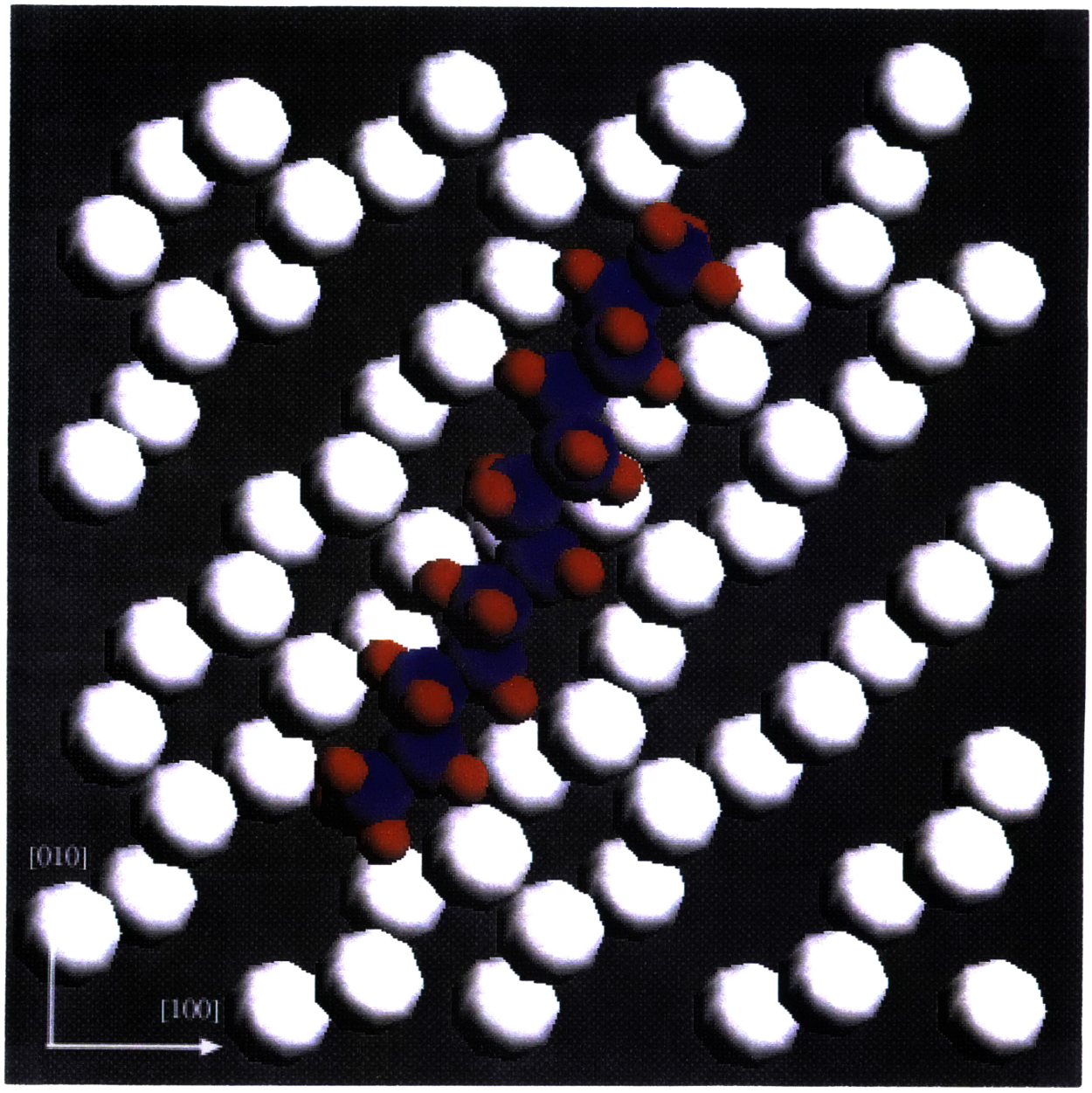

Figure 5-4: Final position of one dodecane molecule: top view.

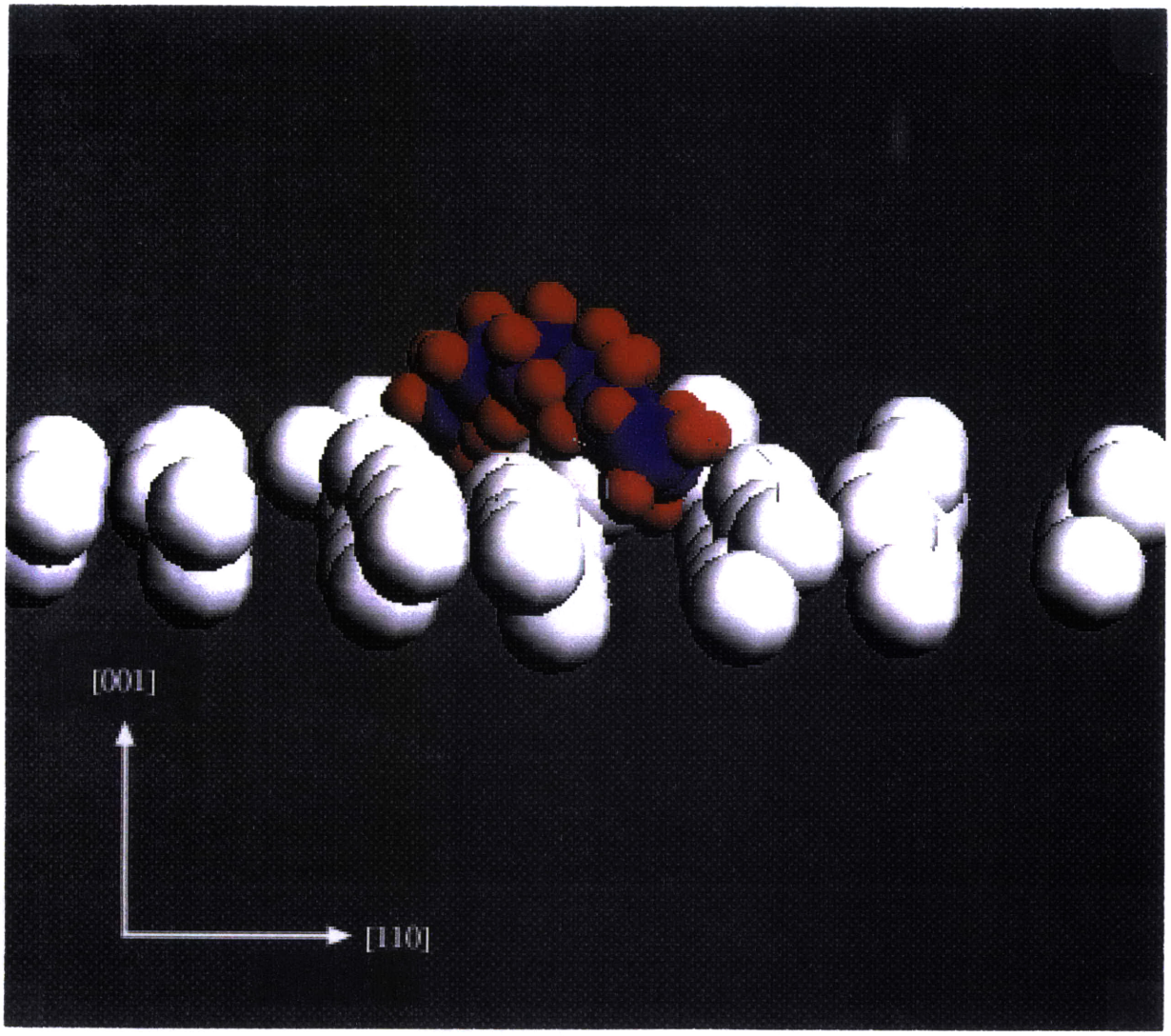

Figure 5-5: Final position of one dodecane molecule: side view.

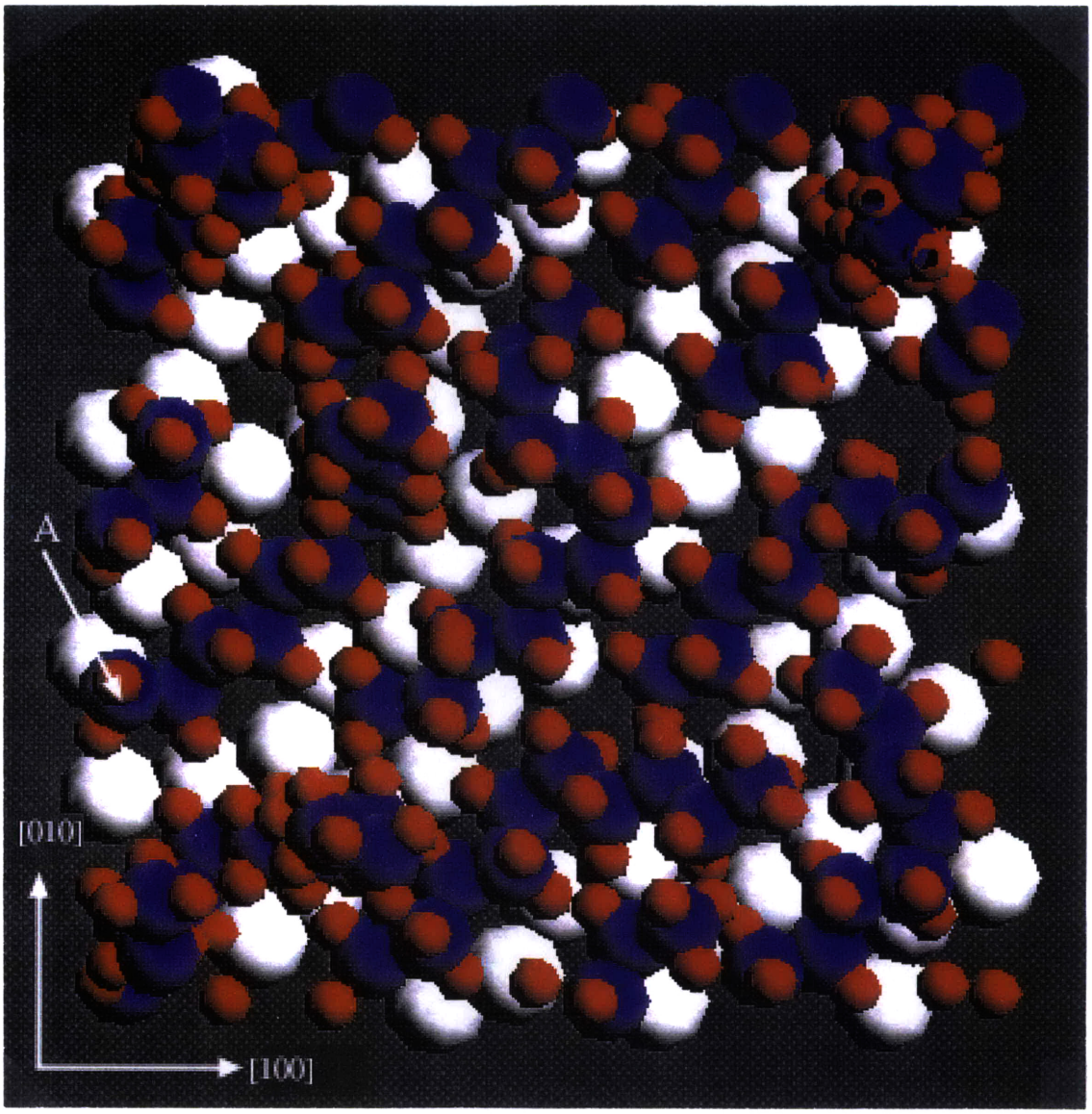

Figure 5-6: Final position of nine dodecane molecules: top view.

steps, which was increased to 100,000 in order to give the molecules ample time to equilibrate. Figures 5-6 and 5-7 show the final positions of the molecules after the system had equilibrated. Due to the presence of many molecules, none of the chains is able to fully occupy the ledges like the single molecule in Figure 5-4. For a typical molecule, only a portion of the chain is in the ledge, and the remaining segment stands up nearly normal to the surface. For example, the molecule labeled "A" in Figure 5-6 has one end adsorbed in a ledge on the surface. The ledge closes off at about the sixth carbon atom, forcing the molecule to divert its direction to adjacent ledges.

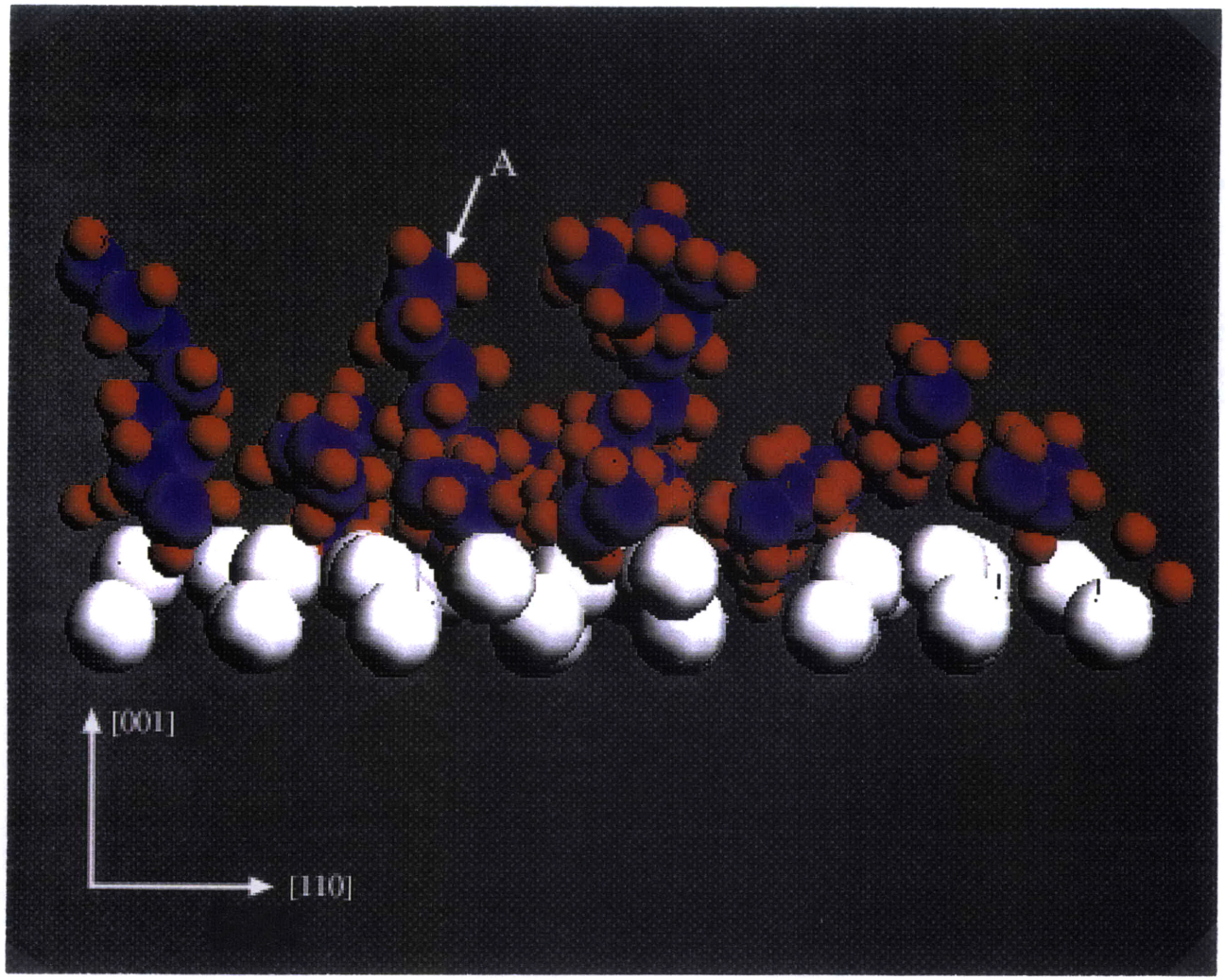

Figure 5-7: Final position of nine dodecane molecules: side view.

However, unlike the previous case of the single dodecane molecule, the adjacent ledges are already occupied by other molecules. In response, the molecule chooses to stand up rather than lie on top of the other molecules. Figure 5-7 show the side view of the system, where it is shown that a portion of molecule A is standing up.

Based on these findings, it is proposed that the adsorption orientation of the molecules depends on the equilibrium lubricant concentration on the surface. At low lubricant coverage, all molecules are able to lie down, filling in the ledges on the surface. At higher lubricant concentrations, the available ledge spaces become saturated. Beyond the full saturation limit, the addition of more molecules results in partial adsorption, whereby only segments of the molecules attain ledge adsorption. Intuitively, it can be hypothesized that at high enough concentrations, the molecules may all be forced to stand up, being anchored to the surface only at the ends. If this is the case, the physical bonding interaction between the surface and the end groups of the lubricant molecules could have significant impact on the effectiveness of the lubricant during the shearing motion.

The next simulation was to raise the temperature of the Si-9$C_{12}H_{26}$ adsorbed system in order to see the desorption phenomena associated with high temperatures. The objective of this experiment was to establish that beyond a certain critical temperature, the molecules are no longer physically affixed to the surface. Iyer [53] found this critical temperature to be 155°C using both heated friction experiments and stiction testing. The present system was heated to 488 K (215°C), which is sufficiently higher than the critical temperature so that the system is sure to be in the desorption mode. The heating process was done as follows: the temperature of the system, initially at 298 K, was raised by 5 K at every 2000 time steps until the desired temperature of 488 K was reached. This process was done incrementally because a sudden increase in temperature could produce unrealistic responses in the system. Following this heating process, a constant temperature run of 20,000 time steps at 488 K was performed to obtain equilibrium properties of the system at 488 K. Figure 5-8 compares the mean squared displacement of the system before and after the heating. At room temperature, the mean squared displacement curve resembles that

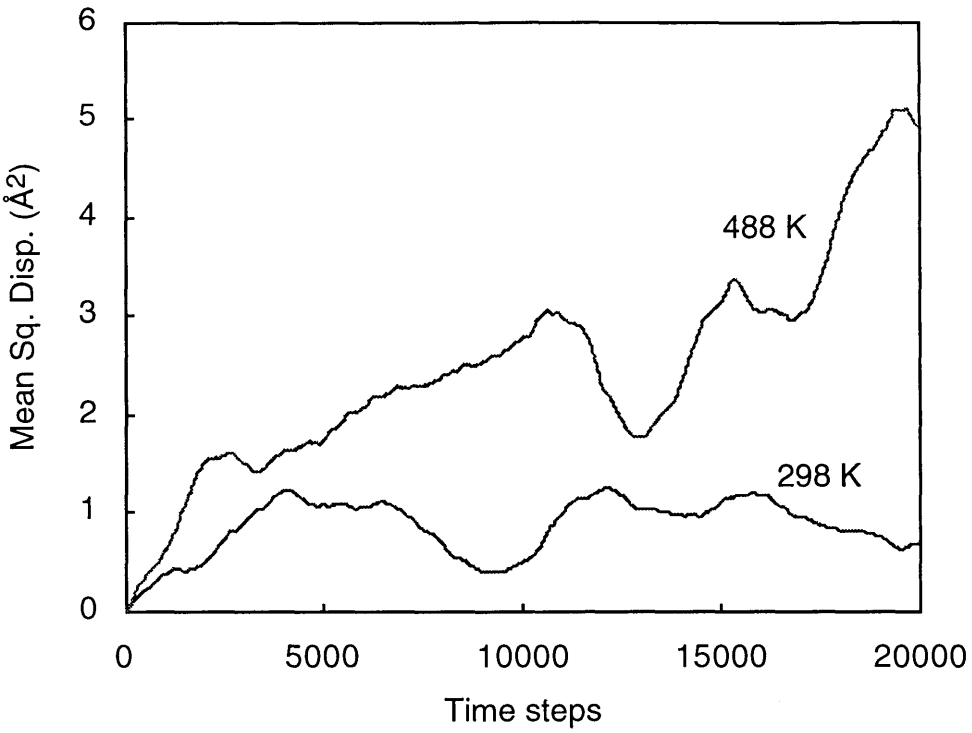

Figure 5-8: Mean squared displacement of carbon atoms on silicon surface.

of a solid material, flattening out to a nearly constant value. This indicates that the molecules are physically attached to and unable to leave their adsorption sites. The molecules display more mobility at the higher temperature, as shown by the rising mean squared displacement. The increase in the kinetic energy of the molecules allows them to break free from their bonds to the surface. The simulation is thus capable of modeling the desorption of molecules from the surface. It is observed in practice that the desorption of lubricant molecules is the cause of the transition of the friction coefficients to higher values at the critical temperature [54]. Although it will not be pursued here, a molecular dynamics simulation study of boundary lubricated systems at high temperatures could yield valuable information concerning the effect of the desorption on the friction between the surfaces.

The vibrational spectra of the nine dodecane molecules were computed for the adsorption of the nine molecules at both 298 K and 488 K. The peaks corresponding to the C-C stretching, C-C-H bending, H-C-H bending, and C-H stretching modes are given in Table 5.2. The results for bulk dodecane from Table 4.7 are also listed here

Table 5.2: Vibrational spectral peaks for adsorbed dodecane.

Bulk (no Si) (1/cm)	Adsorbed on Si at 298 K (1/cm)	Adsorbed on Si at 488 K (1/cm)
955	946	920
1138	1146	1155
1467	1485	1485
2952	2978	2987

for comparison. The changes in vibrational spectra due to the rise in temperature is, at best, marginal. These data can be compared with Raman spectroscopy results which are currently being obtained.

5.2 Silicon-Dodecane System in Compression and Sliding

The boundary lubrication simulation was done with a system of 27 dodecane molecules trapped between the silicon surfaces, as shown in Figure 5-1. The simulation parameters are listed in Table 5.3. The entire system was held at 298 K throughout the compression and sliding stages. Initially, the molecules were arranged into three ordered layers between the silicon surfaces, each molecule positioned as in Figures 5-2 and 5-3. The separation distance between the surfaces was 16.0 Å in the uncompressed state. A Monte Carlo run of 200,000 steps was first performed at constant cell dimensions in order to provide the initial configuration. This output was then used as the initial configuration in MD, and the system was compressed in the z direction. The compression was done by imposing a normal strain, ϵ_{zz} to the dodecane cell in increments of -0.001 at every 1000 times steps for a duration of 80,000 time steps, causing the silicon substrates (including the fixed atoms) to approach each other while squeezing the dodecane film. The system was then allowed to come

Table 5.3: Parameters for the simulation of compression and sliding.

Total number of fixed Si atoms: top	128
Number of layers of fixed Si atoms: top	4
Total number of Si atoms: top	128
Number of Si layers: top	4
Density of Si: top	$2,434$ kg/m^3
Si surface plane: top	$(00\bar{1})$
Si crystal structure: top	Diamond cubic
Number of $C_{12}H_{26}$ molecules	27
Density of $C_{12}H_{26}$	$1,107$ kg/m^3
Total number of Si atoms: bottom	128
Number of Si layers: bottom	4
Density of Si: bottom	$2,434$ kg/m^3
Si surface plane: bottom	(001)
Si crystal structure: bottom	Diamond cubic
Total number of fixed Si atoms: bottom	128
Number of layers of fixed Si atoms: bottom	4
Temperature	298 K
Time increment	0.384×10^{-15} s
Number of time steps:	
Compression	200,000 (MC) + 105,000 (MD)
Sliding	100,000 (MD)

to equilibrium for 25,000 time steps in the compressed state where the fixed atoms of the silicon substrates were held at constant z. By the end of this equilibration, the separation between the silicon surfaces (i.e. dodecane film thickness) had been reduced to 14.8 Å, making the dodecane density $1,107$ kg/m^3. The normal stresses in the z direction, σ_{zz}, of the materials were calculated to be:

$$\begin{aligned} \sigma_{zz,\text{Si-top}} &= 1.84 \text{ GPa}, \\ \sigma_{zz,\text{Si-bottom}} &= 1.83 \text{ GPa}, \textit{and} \\ \sigma_{zz,\text{dodecane}} &= 1.91 \text{ GPa}. \end{aligned}$$

The three values are very close to each other, as expected of a system in equilibrium. Figure 5-9 shows the atomic positions of the full system in compression. The dodecane film is equilibrated in three layers. Two layers, each of nine molecules, are adsorbed on the two silicon surfaces. A middle layer of nine molecules lies between the two adsorbed layers. This equilibrium geometry reflects the initial configuration, which had the molecules placed in three ordered layers of nine molecules each. The tight confinement between the silicon surfaces on the top and bottom and the periodic images in the horizontal directions did not allow the molecules excessive departure from their original positions. The layered configuration of the lubricant qualitatively agrees with experimental findings. Gee, et al. [55] reported that lubricant films less than ten molecular diameters display solid-like behavior characterized by ordering of the molecules into discrete layers.

The next step was to slide the top substrate in the [100] direction. The sliding was modeled by displacing all of the fixed atoms of the top silicon piece by an amount of 7.68×10^{-15} m at every time step, which corresponds to a sliding velocity of 20 m/s. This method of simulating the sliding is different from the one used in the simulations of L-J solids in Chapter 3. By sliding in smaller displacement increments at every time step rather than in larger increments at longer time intervals, a smoother, more realistic motion was simulated. The temperature was rescaled to 298 K at every time step. The rigid silicon boundaries were kept at a constant separation distance

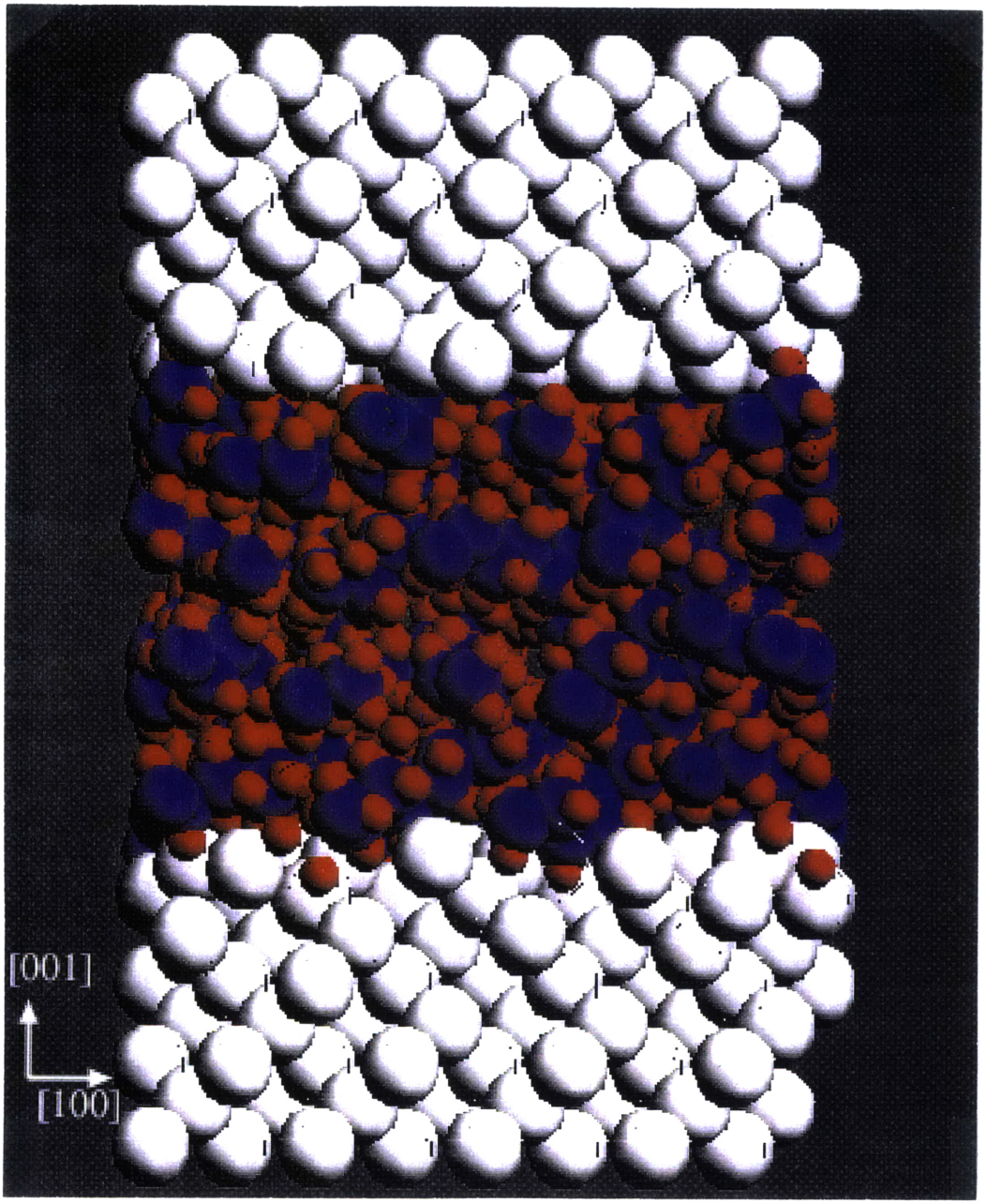

Figure 5-9: Compressed silicon-dodecane system. Compression is in the [001] direction.

of 14.8 Å. Holding the separation constant in this way during the sliding causes the normal stress to fluctuate about some mean value. This differs from experiments, in which the normal load, rather than the separation distance, remains constant. The reason for simulating with the constant separation method was that much computation time would be needed in iterating to a constant normal stress. Since we were interested in the ratio of the friction force to the normal force, the variability of the normal force does not affect the validity of the results.

The sliding was performed for 100,000 time steps covering 7.68 Å of sliding distance. The surface traction and the friction coefficient were computed using the method discussed in section 2.4 for each of the cells. The friction force was assumed to be the tangential component of the surface traction multiplied by the surface area. The traction calculation is based on the stress tensor, which contains both thermal and virial contributions. The sequence of the calculations were as follows. First, the sliding was invoked to the fixed silicon atoms. Simultaneously, all the free atoms moved a step in their trajectories based on the interatomic forces computed from the previous step. Next, the stress tensor as well as the interatomic forces were computed for the new system configuration. Afterward, the velocities were rescaled. Then the sliding was again imposed, and the cycle was repeated. In order to reduce the amount of data, the friction forces were saved only at every 100 time steps.

Figure 5-10 shows the instantaneous tangential and normal stresses acting on the top silicon surface. There is significant thermal fluctuation in the results. Since the temperature is constant, taking the time average eliminates the thermal noise. Figure 5-11 shows the time averaged tangential and normal stresses. The time averaged tangential stress equilibrates to 146 MPa. Similar results were obtained for the bottom silicon and the dodecane cells. Table 5.4 summarizes for all three cells the final average values of the traction stresses. The calculated friction coefficient is about 0.07, which is typical of a boundary lubricated system, as discussed in section 1.2. However, 0.07 is low compared with the experimental friction coefficient of 0.28 from Table 1.2 for boundary lubricated sliding of Si/dodecane.

The discrepancy between the computed and the experimental friction coefficient

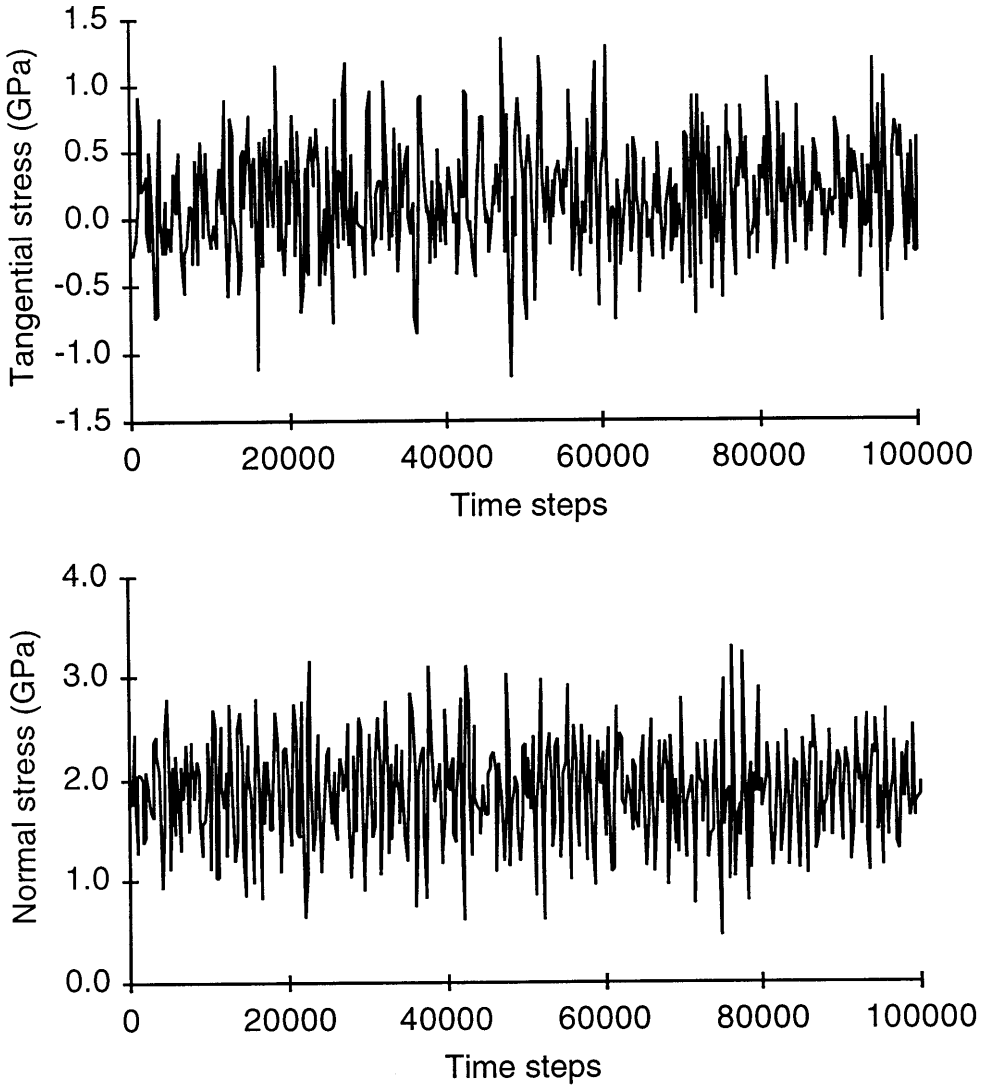

Figure 5-10: Instantaneous tangential and normal stresses in silicon-dodecane sliding. Calculations are for top silicon surface only.

Table 5.4: Tangential and normal stresses in silicon-dodecane sliding.

	Top silicon	Bottom silicon	Dodecane
Normal stress (MPa)	1,874	1,873	1,983
Tangential stress (MPa)	146	128	123
Friction coefficient	0.078	0.069	0.062

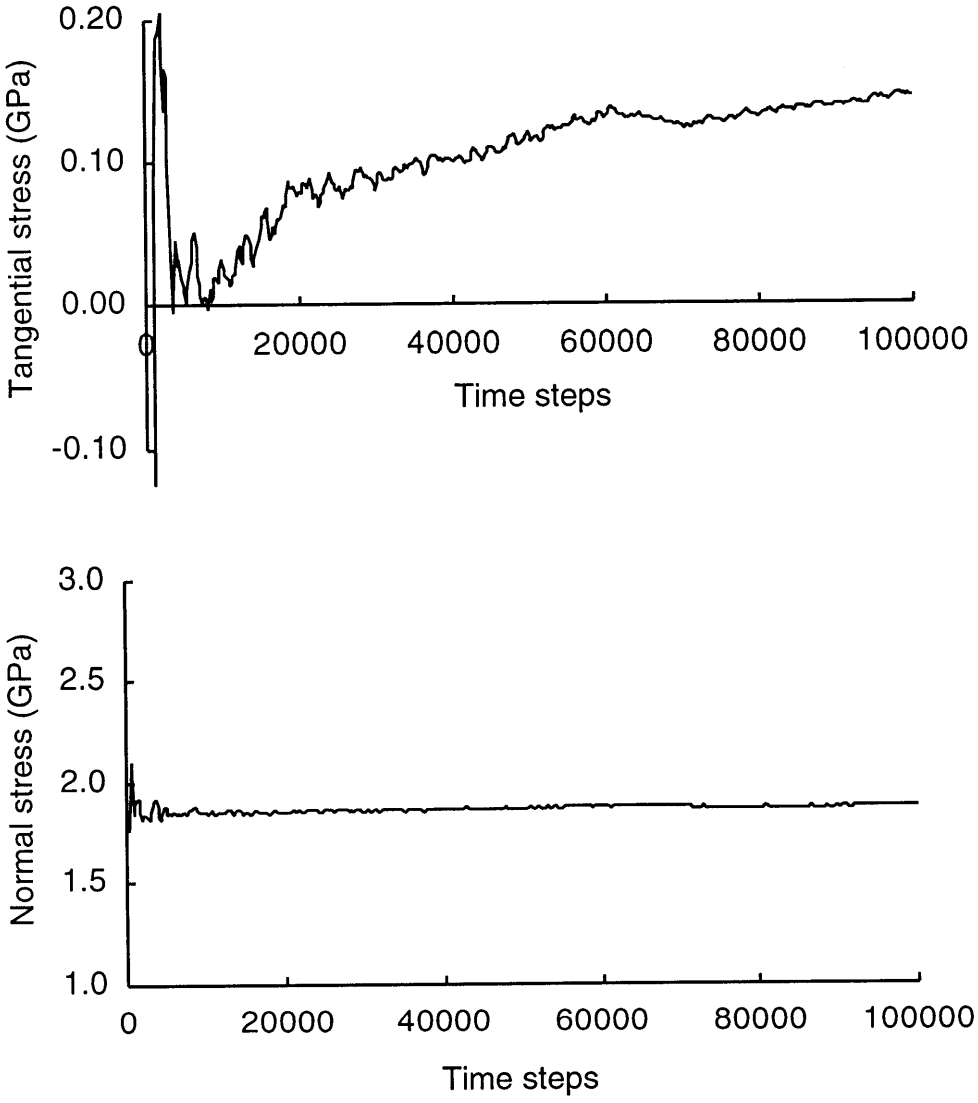

Figure 5-11: Tangential and normal stresses in silicon-dodecane sliding. Time averaged forces for top silicon surface only.

has several sources. First, the simulation environment is perfectly lubricated, and consequently, there are no solid-to-solid interactions. In comparison, an experimental system likely has some direct solid-to-solid contacts which requires a significant shear force, resulting in higher friction. Due to these solid interactions, the real system may also have some degree of wear and permanent deformation such as plowing, which are additional mechanisms of friction in boundary-lubricated sliding [56, 57]. Given these possible sources of the error, the simulation was still able to yield the friction coefficient in reasonable agreement with experiment. With more carefully designed experiments where the lubricant coverage is maximized, the present model can be calibrated to better predict the friction coefficient for perfectly lubricated surfaces under boundary lubricated sliding. Combined with similar simulations without any lubricant in between, simulations can provide a means of predicting the frictional behavior of surfaces at various degrees of lubricant coverage. Such simulations can also be a powerful tool for studying the effect of various parameters, as well as lubricant-surface combinations, in establishing the fundamental mechanisms of friction in boundary lubrication.

Figures 5-12 - 5-17 show the system during the sliding. In these figures, a four-color scheme is used to elucidate the action of the dodecane layers during the sliding. The two layers that are next to the silicon surfaces are shown with blue carbon atoms. The middle layer is shown with green carbon atoms. All hydrogen atoms appear in red. The silicon atoms are white, and the fixed silicon atoms are not shown. It may be noticed in Figure 5-12 that in the adsorbed dodecane layers, the molecules are half standing up, just as in Figure 5-7. The standing segments penetrate into the middle layer region. During the sliding (Figures 5-13 - 5-17), the adsorbed molecules on the whole do not get sheared off. They remain fixed to their respective surfaces, resisting deformation and retaining their initial molecular orientations throughout the process. On the other hand, the middle layer undergoes deformation and shearing as many of its molecules are forced to move around.

The atomic pictures of the sliding process suggest that the dodecane molecules assume very different roles depending on how far they are located from the surfaces.

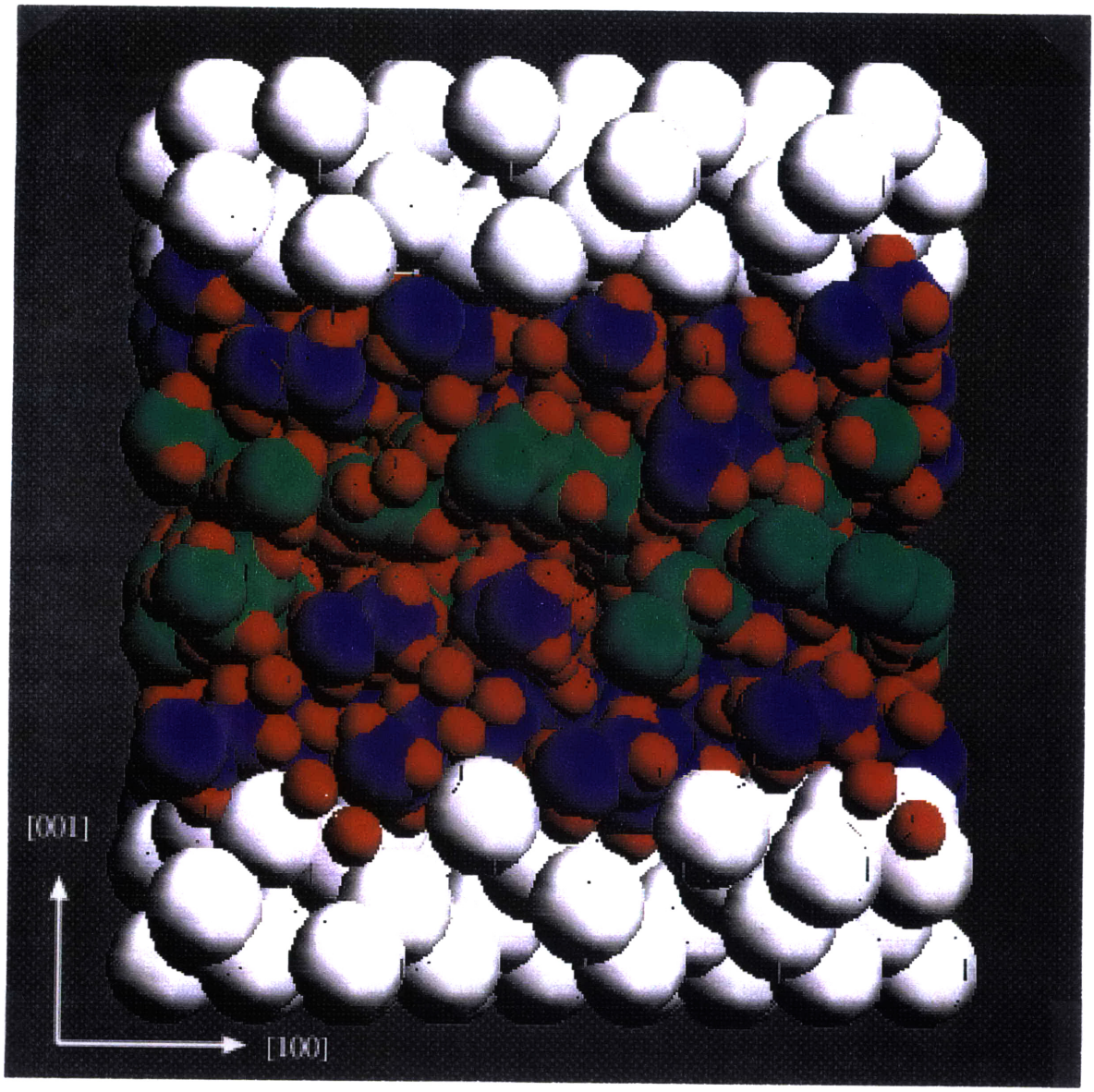

Figure 5-12: Silicon-dodecane system before sliding. Carbon atoms of dodecane molecules adsorbed on silicon surfaces are in blue. Carbon atoms in the middle dodecane layer are in green. All hydrogen atoms are in red, and silicon atoms are in white.

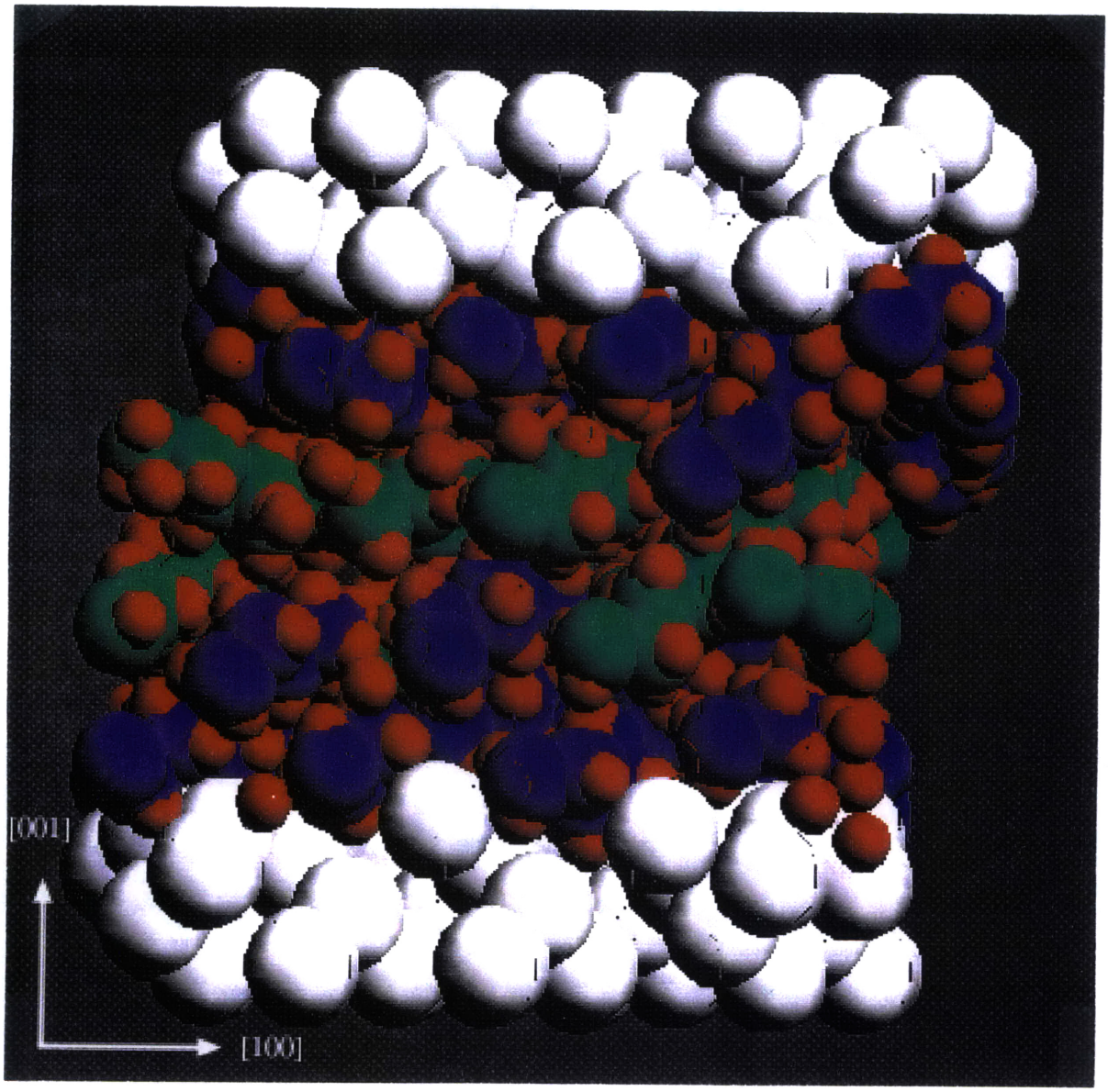

Figure 5-13: Silicon-dodecane system after 1.54 Å of sliding. Sliding is in [100] direction.

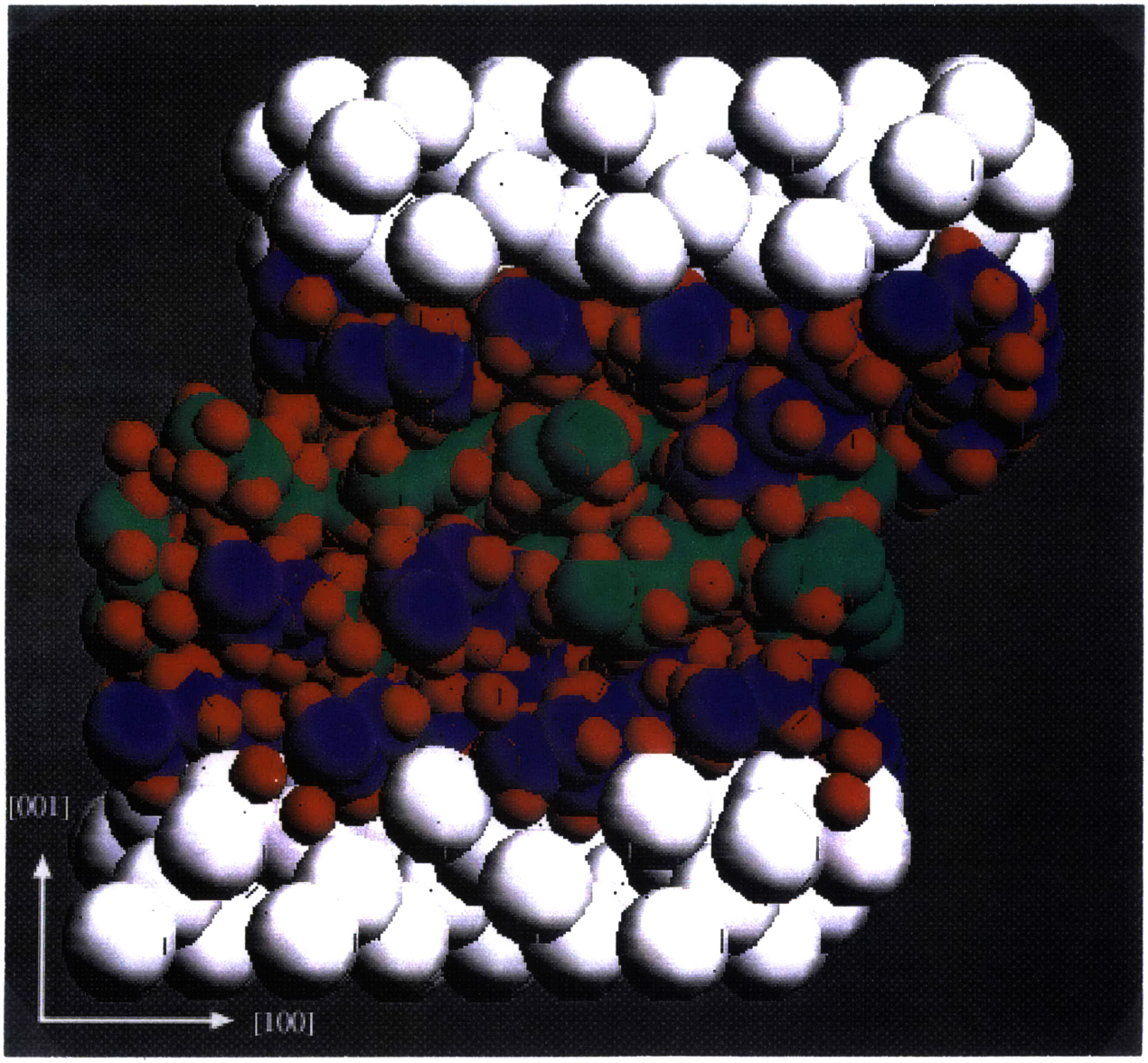

Figure 5-14: Silicon-dodecane system after 3.07 Å of sliding.

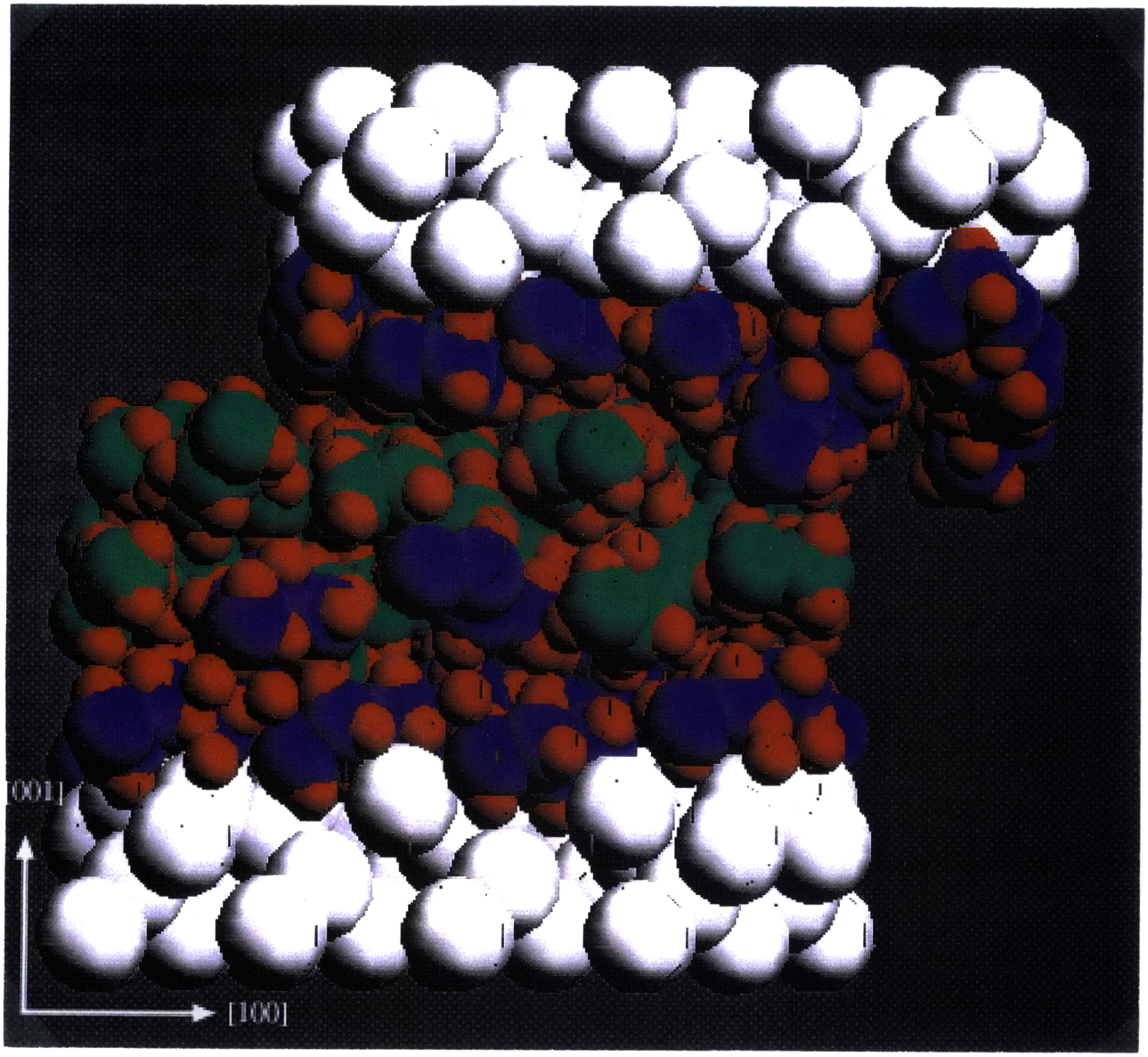

Figure 5-15: Silicon-dodecane system after 4.61 Å of sliding.

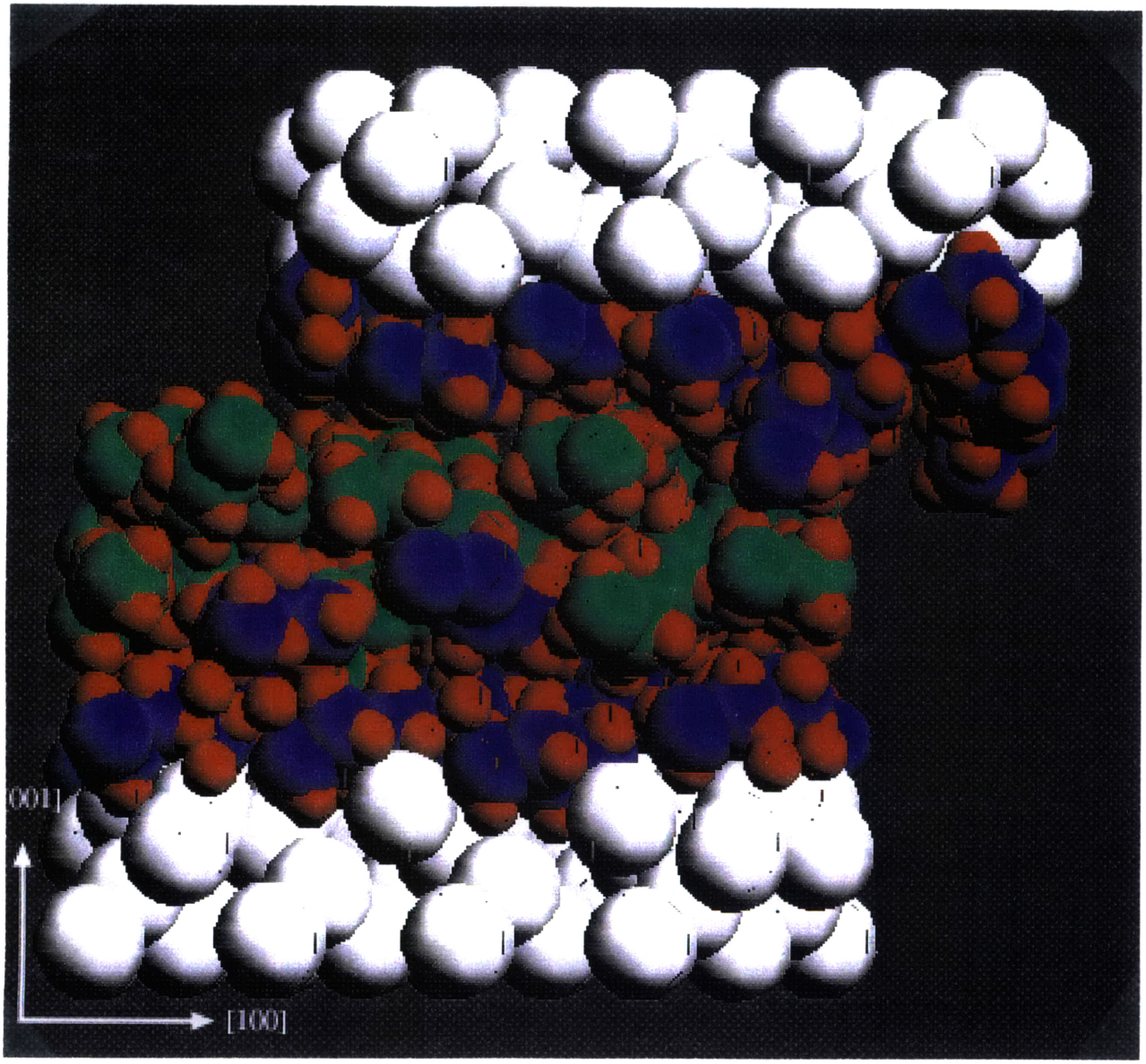

Figure 5-16: Silicon-dodecane system after 6.14 Å of sliding.

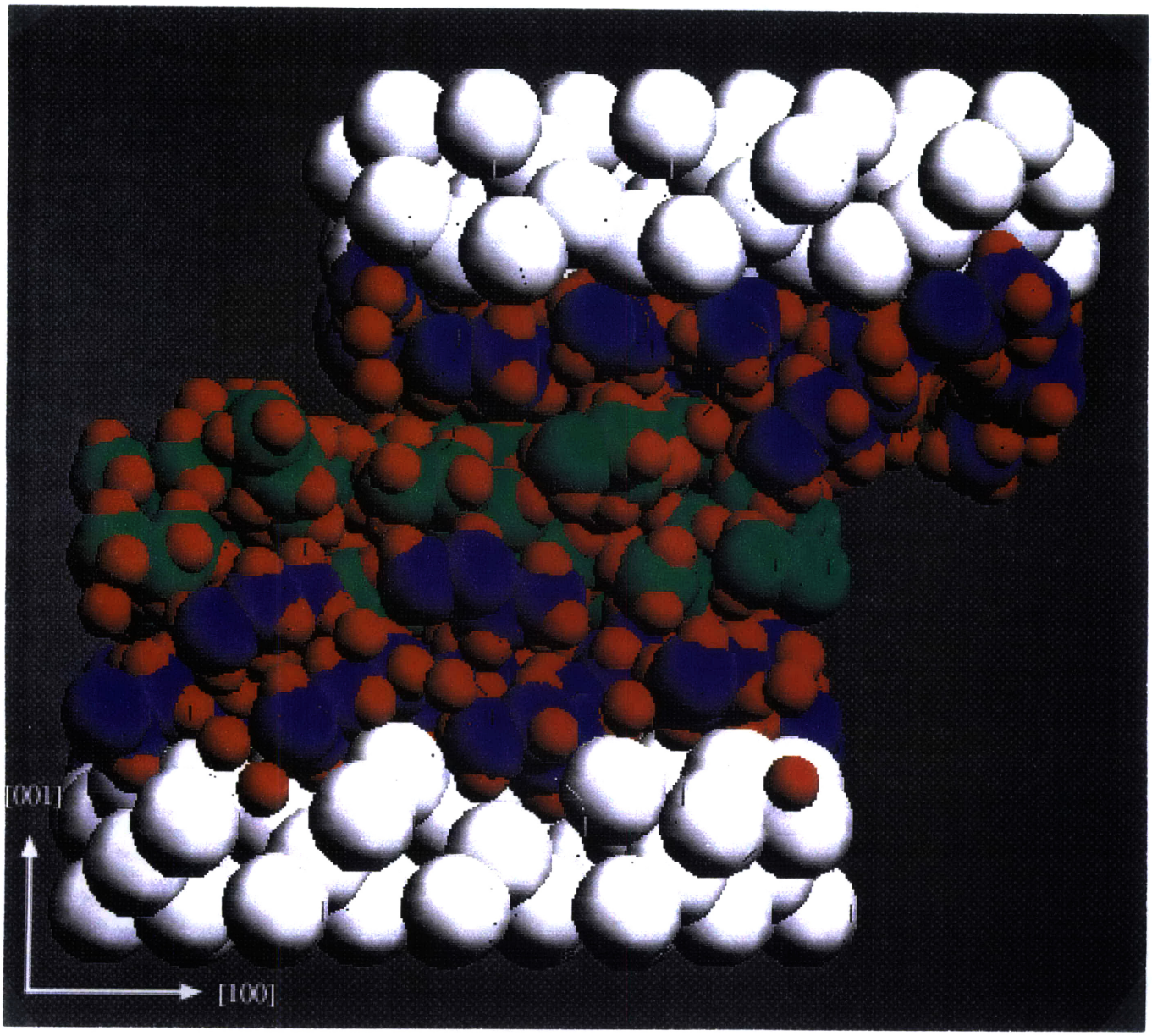

Figure 5-17: Silicon-dodecane system after 7.68 Å of sliding.

Table 5.5: Vibrational spectral peaks of dodecane in compression and sliding. Wavenumbers are in cm^{-1}.

Bulk dodecane	Adsorbed dodecane	Compressed dodecane	Dodecane in sliding
955	946	955	955
1138	1146	1155	1155
1467	1485	1493	1493
2952	2978	2961	2970

Next to the surfaces, the adsorbed layers behave like an extension of the silicon surfaces, as if the solid nature of the substrate has been imparted on the lubricant. Between the adsorbed layers, the middle layer molecules display more liquid-like character as they experience shearing and movement. The shearing of the middle molecules is enhanced by the segments of the adsorbed molecules that are partially standing up and penetrating into the middle of the film. Due to their bond with the solid surface, the segments are probably stiffer than the non-adsorbed chains in the middle. It follows that the segments cause a viscous disturbance to the non-adsorbed molecules. In such an event, more friction force would be needed for the partially adsorbed segments to push around the middle molecules. If the adsorbed molecules were all able to lie flat on the surface, it seems likely that the friction force would be considerably reduced.

The vibrational spectra of the system were computed at the compressed and the sliding stages. The spectra for the sliding stage was obtained over the last 20,000 time steps of sliding. The peaks in the spectrum corresponding to C-C stretching, C-C-H bending, H-C-H bending, and C-H stretching are summarized in Table 5.5. The peaks for the same modes from the bulk and the nine adsorbed molecules are also shown for comparison. There are no drastic changes due to the compression and sliding in the vibrational spectrum of dodecane. As to whether a real system also displays insignificant shifts in the vibrational peaks remains to be seen from the

pending results of the Raman spectroscopy studies.

Chapter 6

Conclusions and Future Research

Molecular dynamics simulations of friction in dry sliding of model solids and of boundary lubricated surfaces have been carried out. The first study addressed the friction between two solid surfaces represented by Lennard-Jones potential functions. The second was of friction in boundary- lubricated sliding of silicon (001) surfaces separated by a film of dodecane ($C_{12}H_{26}$).

The Lennard-Jones solids were modeled using L-J parameters appropriate for argon (Ar) and xenon (Xe). The system was established using two opposing semi-infinite cells. A stable interface was formed by choosing appropriate cell dimensions that matched in periodicity while allowing for different lattice parameters. The system was then compressed by giving the cells a normal strain of -0.002. Next, sliding was effected by displacing the fixed atoms of argon at a speed of 4.9 m/s. The following are the key conclusions of the simulations of Lennard-Jones solids.

- For the bimaterial system whose atomic interactions are of the Lennard-Jones form, the preferred configuration for a single atom on a foreign surface is the hollow-site geometry. The single atom sits in one of the valleys between the surface atoms.

- When the argon and xenon come into contact, disorder is created at the interface region due to the mismatch of their lattices. Argon, whose Lennard-Jones potential is weaker than that of xenon, experiences more disorder. In addition,

the mismatching lattices at the interface do not permit most of the interfacial atoms to attain the favorable hollow-site geometry. Consequently, the Ar-Xe bonds at the interface are weak, so that they are the most vulnerable to breaking during the sliding.

- At the interface, some of the argon atoms are in the "on-top" position with respect to the xenon surface while others are in the "hollow-site" position. The atoms in the hollow-site position are able to penetrate closer to the xenon surface, thereby causing the argon interface layer to have a warped shape. The warped interface continuously becomes distorted as the argon interfacial atoms slide over the various potential hills and valleys of the xenon surface. The interfacial forces required to distort the interface contributes to the friction force, and the work which is used to distort the interface is dissipated as heat.

- The friction coefficient for a L-J system was 0.023, much lower than experimental values for metallic surfaces in sliding. One reason for the discrepancy is that L-J potentials are more suitable for noble gases rather than metals. Another reason is that the simulation does not account for grain boundaries and other sources of slip and permanent deformation, which are additional mechanisms of friction. Also, plowing and wear are not included in the simulations.

The simulation of two silicon (001) surfaces lubricated with a film of dodecane comprised the second part of the study. A combination of semi-infinite and thin-film boundary conditions were used to set up the geometry of the system. The Stillinger-Weber potential function was used to model silicon, while the consistent force field (CFF) model was used for dodecane. A novel potential function for the silicon- dodecane interaction was developed by combining the carbon and hydrogen Lennard-Jones potentials from CFF with a modified Lennard-Jones representation of the Stillinger-Weber potential. This study began with mono- and multi-molecular adsorption simulations. This was followed by the establishment of a silicon-dodecane-silicon system, which was subject to compression resulting in a normal stress of 1.87

GPa. The fixed atoms of the top silicon substrate were then made to slide at a speed of 20 m/s. The following are the key conclusions from these simulation studies.

- On the silicon (001) surface, trench-like ledges develop along the [110] direction. When one dodecane molecule is allowed to interact with the surface, it approaches and adsorbs into one of the ledges. Strong preference for ledge-adsorption is seen when the molecule crosses over to an adjacent ledge when the present ledge is closed off. The preference for ledge adsorption seems to agree with polarized Raman spectroscopy studies which reveal that dodecane molecules adsorb on a silicon (001) surface in the [110] direction.

- When more molecules are placed on the surface, there is not enough ledge space to accommodate all the molecules. Most of the molecules only partially occupy the ledges, while the remaining portion of the chain stand up normal to the surface. It may be concluded, based on these observations, that the adsorption orientation of the molecules depends on the concentration of the lubricant at the surface. If the concentration is low, all the molecules lay flat in the ledges. Beyond a critical concentration, the ledges saturate, causing some of the molecules to partially stand up. This suggests that the right combination of the lubricant/substrate geometry could lead to favorable lubricant adsorption orientations.

- When the system temperature is raised to 488 K, the adsorbed molecules display more mobility, although they do not completely escape the surface. The molecules have more kinetic energy at the higher temperature which allows them to often break free from the silicon atoms. This finding is consistent with experimental stiction and friction tests at elevated temperatures, where it was found that dodecane molecules desorb from the silicon (001) surface at 428 K.

- In the simulation of sliding, the friction coefficient of a well-lubricated system was calculated to be 0.07, which is in reasonable agreement with the experimental values of boundary lubricated surfaces which are in the range 0.06–0.28.

The experimental value for silicon-dodecane-silicon system in sliding was 0.28. The agreement between the simulated result and experimental values seem fair.

- In the sliding simulation, the dodecane molecules adjacent to the silicon surfaces showed solid behavior, acting as an extension of the Si surface. The partially standing adsorbed molecules cause shear deformation to the middle molecular layer of the dodecane film. The middle layer behaves more like a liquid, being deformed and smoothed by the sliding motion of the silicon and the adsorbed molecules.

- It is clear that sliding occurs between the adsorbed layers and the non-adsorbed middle layer. If the adsorbed molecules lie flat without any partially standing segments, there would be less shearing of the middle molecules, resulting in lower friction. Thus, lubricant-substrate combinations which promote the molecules to lie uniformly flat could be expected to yield lower friction in boundary-lubricated systems.

The main contribution of this thesis was the implementation of the system of molecular dynamics for studying the friction in dry as well as boundary lubricated sliding. The potential functions, boundary conditions, and the simulation methodology were satisfactorily established and were found to yield atomic-scale information of the various systems. Several possibilities for future research topics are:

- The silicon-dodecane potential functions used in this study gave qualitatively acceptable results concerning the molecular adsorption orientation. Nevertheless, the potential functions still need to be improved using the results of spectroscopy data. In addition, the experimental desorption data can also be used as an additional calibration point to provide a more accurate well-depth for the potentials.

- A larger system with more surface area needs to be considered to improve the results of adsorption, desorption, and friction simulations. This would reduce the effect of the artificial periodicity imposed by periodic boundary conditions.

- It was found that the concentration of the lubricant at the interface has a strong influence on the orientation of the adsorbed molecules. However, it is not clear yet how to determine the equilibrium concentration of substrate-lubricant interfaces. One method could be to simulate for several different concentrations of the lubricant on the surface and compute the potential energies. The concentration which yields the lowest potential energy could be concluded to be the equilibrium concentration.

- This simulation used a (001) surface, which provided ledges for molecules to lie in. Other surface orientations such as the (111) surface, which has a different surface geometry, could be simulated in order to study how the lubricant behavior differs. The friction coefficient for the different surfaces could be compared, from which important conclusions concerning the role of the surface atomic density, packing, etc. on the molecular adsorption and the friction coefficient could be obtained.

- Lubricant molecules other than dodecane could be simulated. It is well known experimentally that oleic acid, which has a different end group from the n-alkanes, gives lower friction. This phenomena could be investigated in detail for various surface geometries to gain insight into the mechanisms by which oleic acid is the more suitable boundary lubricant.

- The present system could be simulated at higher temperature in order to see the effect of the desorption on the friction coefficient. Most likely, a means of relating the film thickness to the number of desorbed molecules during sliding needs to be established. This is because an increase of the friction coefficient will not likely occur unless the film begins to get thinner, allowing more substrate-substrate interaction.

- Dry sliding of silicon on silicon could be simulated. The friction coefficient in this case should be higher than in the lubricated case. The friction coefficient for the dry case can be combined with the fully lubricated case to predict the

friction coefficient at various degrees of lubricant coverage. Comparisons with experimental values of friction could also be more readily made.

Bibliography

[1] Bhushan, B., and Venkatesan, S., "Friction and Wear Studies of Silicon in Sliding Contact with Thin-Film Magnetic Rigid Disks," *Journal of Materials Research*, Vol. 8, No. 7, 1993, pp. 1611-1628.

[2] White, R.L., Schreck, E., and Wang, R., "Nanoindentation and the Tribology of Head-Disk Interface Components," *IEEE Transactions on Magnetics*, Vol. 32, No. 1, 1996, pp. 110-114.

[3] Federspiel, C.C., Saka, N., and Rabinowicz, E., "Friction and Wear of Magnetic Recording Ceramics in Contact with Abrasive Papers, and Lapping and Magnetic Tapes," *Tribology and Mechanics of Magnetic Storage Systems*, Vol. 4, STLE SP-22, 1987, pp. 159-166.

[4] Hardy, W.B., and Doubleday, I., "Boundary Lubrication - The Paraffin Series," *Proceedings of the Royal Society A*, Vol. 102, 1922, p. 550.

[5] Bowden, F.P., Gregory, J.N., and Tabor, D., "Lubrication of Metal Surfaces by Fatty Acids," *Nature*, Vol. 156, 1945, p.97.

[6] Bowden, F.P., and Tabor, D., **The Friction and Lubrication of Solids**, Clarendon Press, Oxford, 1986, p.176-199.

[7] Boyd, J. and Robertson, B.P., "The Friction Properties of Various Lubricants at High Pressures," *ASME Transactions*, Vol. 167, 1945, p.51.

[8] Appledoorn, J.K., "Physical Properties of Lubricants," Chap. 8, **Boundary Lubrication: An Appraisal of World Literature**, Eds. Ling, F.F., Klaus, E.E., and Fein, R.S., ASME, New York, p. 133.

[9] Campbell, W.E., and Thurber, E.A., "Studies in Boundary Lubrication-II. Influence of Adsorbed Moisture Films on the Coefficient of Static Friction Between Lubricated Surfaces," *ASME Transactions*, Vol. 70, 1945, p. 401.

[10] Sonwalkar, N., Yip, S., and Sunder, S.S., "A Combined Molecular Dynamics and Raman Spectroscopy Approach for Designing Ice-Metal Interfaces," *Journal of Computer-Aided Materials Design*, Vol. 2, 1995, pp. 77-100.

[11] Bhushan, B., Israelachvili, N., and Landman, U., "Nanotribology: Friction, Wear, and Lubrication at the Atomic Scale," *Nature*, Vol. 374, No. 13, 1995, pp. 607-616.

[12] Tomlinson, G.A., "A Molecular Theory of Friction," *Philosophical Magazine and Journal of Science*, Vol. 7, No. 46, 1929, pp. 905-939.

[13] Frenkel, F.C., and Kontorova, T., *Zhurnal Eksperimental Noii Teoreticheskoi Fiziki*, Vol. 8, 1938, p. 1340.

[14] McClelland, G.M., "Friction at Weakly Interacting Interfaces," in **Springer Series in Surface Sciences: Adhesion and Friction**, Vol. 17, Eds. Grunze, M. and Kreuzer, H.J., Springer-Verlag, New York, 1988, pp. 1-16.

[15] Landman, U., Luedtke, W.D., Burnham, N.A., and Colton, R.J., "Atomistic Mechanisms and Dynamics of Adhesion, Nanoindentation, and Fracture," *Science*, Vol. 248, 1990, pp. 454-461.

[16] Gao, J., Luedtke, W.D., and Landman, U., "Nano-elastohydrodynamics: Structure, Dynamics, and Flow in Nonuniform Lubricated Junctions," *Science*, Vol. 270, 1995, pp. 605-608.

[17] Harrison, J.A., White, C.T., Colton, R.J., and Brenner, D.W., "Molecular-Dynamics Simulations of Atomic-Scale Friction of Diamond Surfaces," *Physical Review B*, Vol. 46. No. 15, 1992, pp. 9700-9708.

[18] Harrison, J.A., White, C.T., Colton, R.J., and Brenner, D.W., "Effects of Chemically-Bound, Flexible Hydrocarbon Species on the Frictional Properties of Diamond Surfaces," *Journal of Physical Chemistry*, Vol. 97, No. 25, 1993, pp. 6573-6576.

[19] Perry, M.D., and Harrison, J.A., "Molecular Dynamics Studies of the Frictional Properties of Hydrocarbon Materials," *Langmuir*, Vol. 12, 1996, pp. 4552-4556.

[20] Kim, D.E., and Suh, N.P., "Molecular Dynamics Investigation of Two-Dimensional Atomic-Scale Friction," *Journal of Tribology*, Vol. 116, 1994, p. 225.

[21] Glosli, J.N., and McClelland, G.M., "Molecular Dynamics Study of Sliding Friction of Ordered Organic Monolayers," *Physical Review Letters*, Vol. 70, No. 13, 1993, pp. 1960-1963.

[22] Tupper, K.J., and Brenner, D.W., "Molecular Dynamics Simulations of Friction in Self-Assembled Monolayers," *Thin Solid Films*, Vol. 253, 1994, pp. 185-189.

[23] Grest, G.S., "Interfacial Sliding of Polymer Brushes: A Molecular Dynamics Simulation," *Physical Review Letters*, Vol. 76, No. 26, 1996, pp. 4979-4982.

[24] Koike, A., and Yoneya, M., "Molecular Dynamics Simulations of Langmuir-Blodgett Monolayers," *Journal of Chemical Physics*, Vol. 105, No. 14, 1996, pp. 6060-6067.

[25] Rabinowicz, E., **Friction and Wear of Materials**, John Wiley and Sons, Inc., New York, pp. 198-219.

[26] Abraham, F., "Computational Statistical Mechanics. Methodology, Applications, and Supercomputing," *Advances in Physics*, Vol. 35, No. 1, 1986, pp. 1-111.

[27] Allen, M.P., and Tildesley, D.J., **Computer Simulation of Liquids**, Clarendon Press, Oxford, 1987.

[28] Rahman, A., "Correlations in the Motion of Atoms in Liquid Argon," *Physical Review*, Vol. 136, No. 2A, 1964, pp. A405-A411.

[29] Stillinger, F.H., and Weber, T.A., "Computer Simulation of Local Order in Condensed Phases of Silicon," *Physical Review B*, Vol. 31, No. 8, 1985, pp. 5262-5271.

[30] Siepmann, J.I., Karaborni, S., and Smit, B., "Simulating the Critical Behavior of Complex Fluids," *Nature*, Vol. 365, 1993, pp. 330-332.

[31] Jorgensen, W.L., Madura, J.D., and Swenson, C.J., "Optimized Intermolecular Potential Functions for Liquid Hydrocarbons," *Journal of the American Chemical Society*, Vol. 106, 1984, pp. 6638-6646.

[32] Mundy, C.J., Siepmann, J.I., and Klein, M.L., "Calculation of the Shear Viscosity of Decane Using a Reversible Multiple Time-Step Algorithm," *Journal of Chemical Physics*, Vol. 102, No. 8, 1995, pp. 3376-3380.

[33] Lifson, S., and Warshel, A., "Consistent Force Field for Calculations of Conformations, Vibrational Spectra, and Enthalpies of Cycloalkane and n-alkane Molecules," *Journal of Chemical Physics*, Vol. 49, No. 11, 1968, pp. 5116-5129.

[34] Warshel, A., and Lifson, S., "Consistent Force Field Calculations. II. Crystal Structures, Sublimation Energies, Molecular and Lattice Vibrations, Molecular Conformations, and Enthalpies of Alkanes," *Journal of Chemical Physics*, Vol. 53, No. 2. 1970, pp. 582-594.

[35] Ullo, J.J., and Yip, S., "Molecular Dynamics Simulation of Hydrocarbon Molecules in Condensed Phases. I. Liquid n-butane," *Journal of Chemical Physics*, Vol. 85, No. 7, 1986, pp. 4056-4064.

[36] Andersen, H.C., "Molecular Dynamics Simulation at Constant Pressure and/or Temperature," *Journal of Chemical Physics*, Vol. 72, No. 4, 1980, pp. 2384-2393.

[37] Parrinello, M., and Rahman, A., "Crystal Structure and Pair Potentials: A Molecular Dynamics Study," *Physical Review Letters*, Vol. 45, No. 14, 1980, pp. 1196-1199.

[38] Parrinello, M., and Rahman, A., "Polymorphic Transitions in Single Crystals: A New Molecular Dynamics Method," *Journal of Applied Physics*, Vol. 52, No. 12, 1981, pp. 7182-7190.

[39] Landau, L.D., and Lifshitz, E.M., **Statistical Physics**, Pergamon Press, Oxford, 1980.

[40] Press, W.H., Flannery, B.P., Teukolsky, S.A., and Vetterling, W.T., **Numerical Recipes (FORTRAN)**, Cambridge University Press, Cambridge, 1989, pp. 430-435.

[41] Metropolis, N., Rosenbluth, A.W., Teller, A.H., and Teller, E., "Equation of State Calculations by Fast Computing Machines," *Journal of Chemical Physics*, Vol. 21, No. 6, 1953, p. A405.

[42] Hogervorst, W., "Transport and Equilibrium Properties of Simple Gases and Forces Between Like and Unlike Atoms," *Physica*, Vol. 51, 1971, pp. 77-89.

[43] Kong, C.L., "Combining Rules for Intermolecular Potential Parameters. II. Rules for the Lennard-Jones (12-6) Potential and the Morse Potential," *Journal of Chemical Physics*, Vol. 59, No. 5, 1973, pp. 2464-2467.

[44] Holloway, S., and Bennemann, K.H., "Study of Water Adsorption on Metal Surfaces," *Surface Science*, Vol. 101, 1980, p. 327.

[45] Belamane, H., Halicioglu, T., and Tiller, W.A., "Comparative Study of Silicon Empirical Interatomic Potentials," *Physical Review B*, Vol. 46, No. 4, 1992, pp. 2250-2279.

[46] Phillpot, S.R., Yip, S., and Wolf, D., "How Do Crystals Melt?" *Computers in Physics*, NOV/DEC, 1989, p. 20.

[47] Kluge, M.D., Ray, J.R., and Rahman, A., "Molecular Dynamic Calculation of Elastic Constants of Silicon," *Journal of Chemical Physics*, Vol. 85, No. 7, 1986, pp. 4028-4031.

[48] **Landolt-Börnstein: Crystal and Solid State Physics**, Group 3, Vol. 11, Ed. Hellwege, K.H., Springer, Berlin, 1979, p. 116.

[49] Cui, S.T., Cummings, P.T., and Cochran, H.D., "Multiple Time Step Nonequilibrium Molecular Dynamics Simulation of the Rheological Properties of Liquid n-decane," *Journal of Chemical Physics*, Vol. 104, No. 1, 1996, pp. 255-262.

[50] Cui, S.T., Gupta, S.A., Cummings, P.T., and Cochran, H.D., "Molecular Dynamics Simulations of the Rheology of Normal Decane, Hexadecane, and Tetracosane," *Journal of Chemical Physics*, Vol. 105, No. 3, 1996, pp. 1214-1220.

[51] Svehla, R.A., "Estimated Viscosities and Thermal Conductivities of Gases at High Temperatures," Technical Report R-132, NASA, 1961, pp. 1-26.

[52] Silvestro, M., "Analysis of Boundary Lubricant Films Using Raman Spectroscopy," S.M. Thesis, Department of Mechanical Engineering, Massachusetts Institute of Technology, Cambridge, MA, 1996.

[53] Iyer, N., S.M. Thesis, in progress, Department of Mechanical Engineering, Massachusetts Institute of Technology, Cambridge, MA.

[54] Saka, N., Tian, H., and Suh, N.P., "Boundary Lubrication of Undulated Metal Surfaces at Elevated Temperatures," *Tribology Transactions*, Vol. 32, No. 3, 1989, pp. 389-395.

[55] Gee, M.L., McGuiggan, P.M., and Israelachvili, J.N., "Liquid to Solidlike Transitions of Molecularly Thin Films Under Shear," *Journal of Chemical Physics*, Vol. 93, No. 3, 1990, pp. 1895-1905.

[56] Komvopoulos, K., Saka, N, and Suh, N.P., "The Mechanism of Friction in Boundary Lubrication," *Journal of Tribology*, Vol. 107, 1985, pp. 452-462.

[57] Suh, N.P., **Tribophysics**, Prentice-Hall, Englewood Cliffs, NJ, 1986.